

HIGH-PERFORMANCE ORGANIC PHOTODIODES AND THEIR APPLICATIONS

A Dissertation
Presented to
The Academic Faculty

by

Wen-Fang Chou

In Partial Fulfillment
of the Requirements for the Degree
Doctor of Philosophy in the
School of Electrical and Computer Engineering

Georgia Institute of Technology
August 2019

COPYRIGHT © 2019 BY WEN-FANG CHOU

HIGH-PERFORMANCE ORGANIC PHOTODIODES AND THEIR APPLICATIONS

Approved by:

Dr. Bernard Kippelen, Advisor
School of Electrical and Computer
Engineering
Georgia Institute of Technology

Dr. Benjamin Klein
School of Electrical and Computer
Engineering
Georgia Institute of Technology

Dr. Gee-Kung Chang
School of Electrical and Computer
Engineering
Georgia Institute of Technology

Dr. Gregory Abowd
School of Interactive Computing
Georgia Institute of Technology

Dr. Omer Inan,
School of Electrical and Computer
Engineering
Georgia Institute of Technology

Date Approved: May 03, 2019

To my family.

ACKNOWLEDGEMENTS

First, I would like to sincerely thank my advisor, Dr. Bernard Kippelen for his support, encouragement, and guidance in the past years, which inspire me greatly not only in academic studies but also in some perspectives of life. I also would like to thank Dr. Gee-Kung Chang, Dr. Omer Inan, Dr. Benjamin Klein, and Dr. Gregory Abowd for serving on my committee. I thank their valuable time and input for my Ph.D. work.

I am indebted to all of the members in Kippelen Research Group. Especially, I would like to extend my gratitude to Dr. Canek Fuentes-Hernandez, who is always generous to share his knowledge and provides valuable and insightful opinions for scientific discussions. In addition, I would like to thank Dr. Silja Abraham, Dr. Xiaojia Jia, Xiaoqing Zhang, Felipe Larrain, Victor Rodriguez-Toro, Youngrak Park, Oliver Moreno, Yi-Chien Chang, Gunhee Kim, and the past group members who helped and supported me. It is truly a pleasure to work with all of them, and I appreciate the friendship with them. Their help and assistance make my Ph.D. work possible.

This work was funded by Office of Naval Research (ONR), Air Force, Center for Advanced Organic Photovoltaics (CAOP), National Nuclear Security Administration (NNSA), and Consortium for Nonproliferation Enabling Capabilities (CNEC).

Lastly, I would express my deepest gratitude to my family. I thank their endless love and encouragement. I also thank Wei-Chun Hung, who always has faith in me. Their support makes my Ph.D. journey completed and meaningful. This dissertation is dedicated to all of them.

TABLE OF CONTENTS

ACKNOWLEDGEMENTS	iv
LIST OF TABLES	viii
LIST OF FIGURES	ix
LIST OF SYMBOLS AND ABBREVIATIONS	xiv
SUMMARY	xx
CHAPTER 1. Introduction	1
1.1 Photodetectors	1
1.2 Current Technologies of Photodetectors	2
1.3 Development of Organic Photodiodes	4
1.4 Flexible and Printed Organic Photodiodes	7
1.5 Current Challenges of Organic Photodiodes	9
1.6 Objectives of the Research	10
1.7 Structure of the Dissertation	11
CHAPTER 2. Background	13
2.1 Organic Semiconductors	13
2.2 Semiconductor Physics	19
2.2.1 Fermi Level Energy Under Equilibrium	19
2.2.2 Fermi Level Energy Under Non-Equilibrium	20
2.2.3 Carrier Generation/Recombination	21
2.3 Working Principles of Organic Photodiodes	22
2.3.1 Device Structure	22
2.3.2 Donor/Acceptor Interfaces	25
2.3.3 Operation of Organic Photodiodes	27
2.4 Equivalent Circuit Model	30
2.5 Performance Metrics of Organic Photodiodes	33
2.5.1 Response Time	33
2.5.2 Responsivity	34
2.5.3 Linear Dynamic Range	34
2.5.4 Noise	35
2.5.5 Noise Equivalent Power and Specific Detectivity	38
CHAPTER 3. Experimental Methods	40
3.1 Materials	40
3.2 Fabrication Procedures	43
3.2.1 Substrate Preparation	43
3.2.2 Electron-Collection Interlayer Deposition	44
3.2.3 Photoactive Layer Deposition	44
3.2.4 Hole-Collection Layer Deposition	45

3.2.5	Device Structure	46
3.3	Electrical p-Doping	47
3.4	Atomic Layer Deposition	47
3.5	Characterization	49
3.5.1	Current-Voltage Measurements	49
3.5.2	Irradiance- and Temperature-Dependent Current-Voltage Measurements	49
3.5.3	Spectral Responsivity Measurements	50
3.5.4	Linear Dynamic Range Measurements	51
3.5.5	Response Time	51
CHAPTER 4.	Origins of the Dark Current	52
4.1	Introduction	52
4.2	Establish an OPD with Low Dark Current	53
4.3	Irradiance- and Temperature-Dependent Studies	54
4.4	A Comparison with Si PDs	58
4.5	Summary	65
CHAPTER 5.	Large-Area and Flexible Organic Photodiodes	66
5.1	Introduction	66
5.2	Area Scaling	67
5.2.1	Area Scaling	69
5.2.2	Responsivity	76
5.2.3	Noise Equivalent Power and Specific Detectivity	77
5.2.4	Field of View	77
5.3	Photoplethysmogram	78
5.4	Summary	82
CHAPTER 6.	A Method for Decreasing the Dark Current in Thin Devices	83
6.1	Introduction	83
6.2	Dark Current Reduction in PMA-Doped Devices	83
6.3	Simulation of J-V Characteristics	86
6.4	Photodetector Performance	87
6.4.1	Responsivity	87
6.4.2	Linear Dynamic Range	90
6.4.3	Noise Equivalent Power and Specific Detectivity	91
6.4.4	Response Time	94
6.5	Application to Other Systems	98
6.6	Summary	101
CHAPTER 7.	Conclusions and Future Work	102
7.1	Conclusions	102
7.2	Future Work	103
7.2.1	Device Stability	103
7.2.2	Photoresponse Spectrum	104
7.2.3	Stretchable Organic Photodiodes	104
7.2.4	Self-Sustainable Sensors	105

LIST OF TABLES

Table 1 The dark current density values at -10 mV of OPDs with different areas, ranging from 0.1 to 0.9 cm ²	68
Table 2 Parameters extracted from the equivalent circuit model.	87
Table 3 Fitting parameters of photocurrent decay generated with different optical power.	97

LIST OF FIGURES

Figure 1.1 Photodetector market size and applications.	1
Figure 2.1 Ethylene chemical structure and energy levels of atomic orbitals and molecular orbitals in an ethylene molecule.	14
Figure 2.2 The energy levels and formation of LUMO and HOMO in conjugated molecules.	16
Figure 2.3 Energy levels in organic solid bulk.	18
Figure 2.4 Basic structure of OPDs.	23
Figure 2.5 (a) The conventional structure, and (b) the inverted structure.	24
Figure 2.6 Representation of the formation of charge-transfer (CT) states at the molecular level.	26
Figure 2.7 Energy levels of layers of organic photodiodes (a) before contact and (b) after contact in a dark condition.	28
Figure 2.8 Energy levels of layers of organic photodiodes under illumination.	29
Figure 2.9 (a) An equivalent circuit diagram of a photodiode. (b) J - V characteristics.	32
Figure 2.10 Schematics of the response time characterization.	33
Figure 2.11 (a) Noise represented in the time domain and (b) the power spectral density in the frequency domain.	36
Figure 2.12 Optical power-dependent photocurrent plot showing nonlinearity at low-light level illumination.	39
Figure 3.1 Chemical structure of materials used in OPDs.	43
Figure 3.2 Cross section of the reference device.	46

Figure 3.3 Top view of reference devices.....	46
Figure 3.4 Picture of PMA doping for a polymer film.	47
Figure 3.5 The procedure of Al ₂ O ₃ layer deposition using ALD.	48
Figure 3.6 The setup schematic of response time measurement.....	51
Figure 4.1 The dark J - V characteristics of (a) P3HT:PCBM- and (b) P3HT:ICBA-based OPDs measured at room temperature.	53
Figure 4.2 Measured and modeled open-circuit voltage vs. short-circuit current density characteristics over various temperatures of (a) P3HT:PCBM-based and (b) P3HT:ICBA- based OPDs.....	55
Figure 4.3 Transport bandgap extraction from the reverse saturation current density vs. inverse of the product between thermal energy and ideality factor.	57
Figure 4.4 A comparison of (a) measured J - V characteristics, (b) measured I - V characteristics in the reverse in the dark for P3HT:ICBA OPDs and Si PDs.....	58
Figure 4.5 A comparison of spectral responsivity measured in P3HT:ICBA OPDs and Si PDs.....	59
Figure 4.6 The response times in OPDs measured with varying load resistance compared to those in Si PDs.....	60
Figure 4.7 Frequency response in OPDs.....	60
Figure 4.8 (a) Normalized transient photocurrent of OPDs at various applied bias. (b) Photocurrent vs. electrical field.	61
Figure 4.9 Temporal evolution of the dark current measured at 0 V in (a) a P3HT:ICBA OPD, and (b) a Si PD (Hamamatsu S1133).	62
Figure 4.10 The current vs. the optical power characteristics in P3HT:ICBA OPDs.	63

Figure 4.11 Current transients in P3HT:ICBA OPDs showing (a) NEP_t and (b) linear interpolation of SNR equal to 1, and (a) NEP_g and (b) linear interpolation of SNR equal to 1	64
Figure 4.12 The spectral specific detectivity of P3HT:ICBA OPDs and Si PDs.	64
Figure 5.1 J - V characteristics of OPDs with various device areas measured in the dark condition.	68
Figure 5.2 Fabrication steps of flexible OPDs using PEDOT:PSS layers as bottom electrodes.	70
Figure 5.3 J - V characteristics of OPDs with various device areas measured in a dark condition.	70
Figure 5.4 Transient dark current fluctuations around steady-state dark current measured at 0 V.	71
Figure 5.5 Responsivity measurement at 635 nm with a 1.3 cm ² OPD.	71
Figure 5.6 Device structure of OPDs with Ag as bottom electrodes.	72
Figure 5.7 Transmittance of transparent Ag on a PET substrate.	73
Figure 5.8 A comparison of dark J - V characteristics of OPDs fabricated on glass and PES substrates.	73
Figure 5.9 (a) The measured steady-state dark J - V characteristics of OPDs with 0.1 and 1.0 cm ² . (b) Comparison of the dark current densities at low-voltage operation between Si PDs and OPDs with similar sizes.	75
Figure 5.10 Transient dark current fluctuations around steady-state dark current measured at 0 V in (a) an 0.1 cm ² , and (b) an 1.0 cm ² OPD.	75
Figure 5.11 (a) Responsivity measurement at 635 nm with a (a) 0.1 cm ² and a (b) 1.0 cm ² OPD operating at 0 V.	76
Figure 5.12 FOV measurement of flexible OPDs.	78

Figure 5.13 Concept of PPG measurement in a reflection mode.....	79
Figure 5.14 The setup of PPG measurements. (a) Schematic illustration of reflectance-mode PPG measurements with (i) a Si PD and (ii) a ring-OPD. (b) Circuit of PPG signal readout.....	80
Figure 5.15 The measured of PPG signals with varying optical power of LED illuminated at 635 nm, sensing with (a) a low-noise Si PD (Hamamatsu S1133), (b) with a ring-OPD.	81
Figure 6.1 PMA-doped OPD devices treated with ALD. (a) Device structure and chemical structure of P3HT, ICBA, and PMA. (b) A comparison of stabilized J - V characteristics measured under dark of PMA-doped devices and those with 1 cycle of Al_2O_3 treatment using ALD.	85
Figure 6.2 Stabilized J - V characteristics measured under dark of PMA-doped devices with (a) Al_2O_3 and (b) HfO_2 treatment with various cycle numbers using ALD.	85
Figure 6.3 Measured and simulated J - V characteristics at room temperature of ALD-treated OPDs and the parameters derived from equivalent circuit model. (a) $V_{\text{OC}} - J_{\text{SC}}$ characteristics illuminated under 9 orders of magnitude of irradiance, $10^{-10} - 10^{-1} \text{ W/cm}^2$. (b) J - V characteristics under dark. The table summarizes the parameters.....	86
Figure 6.4 A comparison of spectral responsivity measurements of devices without treatment and with 1 and 5 cycles of treatment.	89
Figure 6.5 A comparison of spectral responsivity measurements in devices with a 200 nm- and 500 nm-thick photoactive layer.	89
Figure 6.6 . Measurement of linear dynamic range at 653 nm showing larger than 136 dB and the measured noise current under dark equal to 22 fA.....	90
Figure 6.7 Current fluctuations measured under dark.	92
Figure 6.8 Direct measurement of NEP . (a) Temporal photocurrents corresponding to a gradual increase of optical power. (b) Minimum detectable optical power associated with	

the noise equivalent power at 653 nm derived from the signal-to-noise ratio equal to one.	92
Figure 6.9 Specific detectivity values derived from measured <i>NEP</i> and linear <i>NEP</i> value operated at 80 Hz, and white noise limited specific detectivity values.	94
Figure 6.10 Response time of OPDs with different thickness. (a) PMA-doped P3HT:ICBA OPDs. (b) intrinsic P3HT:ICBA OPDs.	95
Figure 6.11 Photocurrent decay profile of ALD-treated OPDs illuminated with different optical power. The dynamics follows a single exponential decay with a time constant of 3.09 μ s illuminated at 1.7 nW.....	97
Figure 6.12 Stabilized dark <i>J-V</i> characteristics of ITO/PEIE (10 nm)/PDPP3T:PC ₇₁ BM (80 nm) /MoO ₃ (10 nm)/Ag devices with 5, 10, and 15 cycles of Al ₂ O ₃ treatment. Symbols refer to the mean value and filled areas refer to the range of minimum to maximum, calculated over five devices for each condition.....	98
Figure 6.13 Spectral responsivity of the device with 10 cycles of Al ₂ O ₃ treatment.	99
Figure 6.14 Stabilized dark <i>J-V</i> characteristics of ITO/PEIE (10 nm)/P3HT:ICBA (200 nm)/MoO ₃ (10 nm)/Ag devices with 10, 50, and 100 cycles of Al ₂ O ₃ treatment. Symbols refer to the mean value and error bars refer to the standard deviation, calculated over five devices for each condition.	100

LIST OF SYMBOLS AND ABBREVIATIONS

PMTs	Photomultiplier tubes
SiPMs	Silicon photomultipliers
APDs	Avalanche photodiodes
OPDs	Organic photodiodes
OPTs	Organic phototransistors
OPV	Organic photovoltaics
D/A	Donor/acceptor
CuPc	Copper phthalocyanine
PV	Perylene tetracarboxylic derivative
V_{OC}	Open-circuit voltage
J_{SC}	Short-circuit current density
MEH-PPV	Poly(phenylene-vinylene)
C ₆₀	Fullerene
BHJ	Bulk heterojunction
CN-PPV	Cyano-PPV
EQE	External quantum efficiency
P3OT	Poly(3-octyl thiophene)
Si PDs	Si photodiodes

D^*	Specific detectivity
R	Responsivity
I_{dark}	Dark current
J_{dark}	Dark current density
SNR	Signal-to-noise ratio
PEN	Polyethylene naphthalate
PPG	Photoplethysmogram
ALD	Atomic layer deposition
LUMO	Lowest unoccupied molecular orbital
HOMO	Highest occupied molecular orbital
$E_{LUMO-HOMO}$	LUMO-HOMO bandgap
E_{fund}	Fundamental bandgap
IE	Ionization energy
EA	Electron affinity
E_{tran}	Transport gap
E_{opt}	Optical bandgap
S_0	Ground state
S_1	First excited state
E_F	Fermi level energy

$f(E)$	Fermi-Dirac distribution
k	Boltzmann constant
T	Temperature
n_0	Intrinsic electron concentration
p_0	Intrinsic hole concentration
$g_C(E)$	Density of state of the conduction band
$g_V(E)$	Density of state of the valence band
E_C	Energy at the conduction band edge
E_V	Energy at the valance band edge
N_C	Effective density of states per unit volume in the conduction band
N_V	Effective density of states per unit volume in the valance band
Δn	Excess electron concentration
Δp	Excess hole concentration
n_i	Intrinsic electron concentration
p_i	Intrinsic hole concentration
F_n	Quasi-Fermi level energy for electrons
F_p	Quasi-Fermi level energy for holes
E_i	Intrinsic Fermi level energy
E_b	Binding energy

q	Fundamental charge of the electron
RT	Room temperature
CT	Charge transfer
ϕ_{bi}	Build-in potential
V_{ph}	Photovoltage
J_{ph}	Photogenerated current
R_s	Series resistance
R_p	Shunt resistance
J_o	Reverse saturation current density
n	Ideality factor
J	Current density
V	Voltage
B	Bandwidth
t_r	Rise time
t_f	Fall time
h	Plank constant
ν	Frequency
LDR	Linear dynamic range
rms	Root mean square

I_{dark}	Dark current
$I_{\text{dark,rms}}$	Dark current fluctuations around average value (noise current)
S_n	Power spectral density
A	Device area
ϕ_{opt}	Optical power
NEP	Noise equivalent power
ITO	Indium-doped tin oxide
PEDOT:PSS	Poly(3,4-ethylenedioxythiophene):polystyrene sulfonate
PEIE	Polyethylenimine ethoxylated
P3HT	Poly(3-hexylthiophene-2,5-diyl)
PDPP3T	Poly(diketopyrrolopyrrole-terthiophene)
ICBA	Indene C60-bisadduct
PC ₆₁ BM or	
PCBM	[6,6]-Phenyl C61 butyric acid methyl ester
PC ₇₁ BM	[6,6]-Phenyl C71 butyric acid methyl ester
NIR	Near infrared
CF	Chloroform
DCB	1,2-dichlorobenzene
PMA	Phosphomolybdic acid
ALD	Atomic layer deposition

TMA Trimethylaluminum

SUMMARY

Photodetectors are prevalent in daily life. With the advance of emerging technologies in wearable electronics, human-computer interaction, and health care, the demand for photodetectors is rapidly increasing. Photodetectors consisting of crystalline inorganic materials show high performance and satisfy the requirements for conventional electronics. The mechanical properties and design process of inorganic photodetectors, however, are complex, posing challenges to the realization of future innovations. In contrast to commercially available inorganic counterparts, organic photodetectors enable a highly conformal form factor and a simple fabrication process of a large area at low temperature and low cost. In addition, the electrical and optical properties of organic materials can be easily tailored through chemical synthesis. Therefore, organic photodetectors hold considerable potential to deliver multiple functionalities in the design of electronics.

In this work, we develop high-performance organic photodiodes (OPDs) with an unprecedented level of performance that can rival that of low-noise silicon photodiodes (Si PDs). The magnitude and fluctuations in the dark current plays a key role in low-light level sensing devices. We begin by investigating the physical origins of the dark current values in OPDs by conducting studies of irradiance- and temperature-dependence current-voltage characteristics. We find that both the parasitic shunt resistance and the thermally-activated reverse saturation current density are significant in determining the noise level of OPDs. With this insight, we demonstrate the selection of proper materials with weak electronic

interactions between donors and acceptors and produce a low-noise photodiode with a measured specific detectivity value of 8×10^{13} Jones.

Next, we present a study of the scalability of solution-processed P3HT:ICBA OPDs and show that their dark current values are comparable to those of low-noise Si PDs of similar size at low-voltage operation. Then, we demonstrate large-area OPDs fabricated on flexible substrates yielding low dark current density values (J_{dark}) in the pA/cm² range at low-voltage operation, leading to a high specific detectivity value approaching 10^{13} Jones. With this capability, we design flexible and large-area OPDs into a ring geometry for photoplethysmogram sensing. As they deliver high conformity and efficient optical power collection, the OPDs show 9.6 times less power consumption than low-noise Si PDs when the signal-to-noise ratio equals one.

Finally, we introduce a universal method using atomic layer deposition for reducing dark current density values for OPDs with low shunt resistance. OPDs with thin photoactive layers enable a wider linear dynamic range and a faster response, but the high dark current values result in poor detectivity. This superficial treatment decreases J_{dark} in reverse bias by five orders of magnitude in 200 nm-thick p-doped OPDs, leading to a measured noise equivalent power of 2.9 pW, a specific detectivity value of 7.5×10^{12} Jones at low frequency, and an estimated peak specific detectivity value of 7.2×10^{13} Jones at high frequency. In particular, the doped thin OPDs yield a single exponential photoresponse with a time constant of 3.1 μ s illuminated in the range of nW, without a lag tail. This strategy provides a solution to the problem of sensing a continuous pulse of light with weak optical power.

CHAPTER 1. INTRODUCTION

1.1 Photodetectors

Photodetectors transduce optical signals into electrical signals that are prevalently used in our daily life. Photodetectors with high detectivity values at low light levels have drawn wide attention because they underpin a variety of sensing applications in imaging, security, automotive industry, healthcare, LiDAR (Light Detection and Ranging), and the internet of things (I-4). The photodetector market is rapidly increasing, and the global revenue of photodetectors was 13 billion dollars in 2016 and is projected to reach 21 billion dollars in 2022, shown in Figure 1.1.

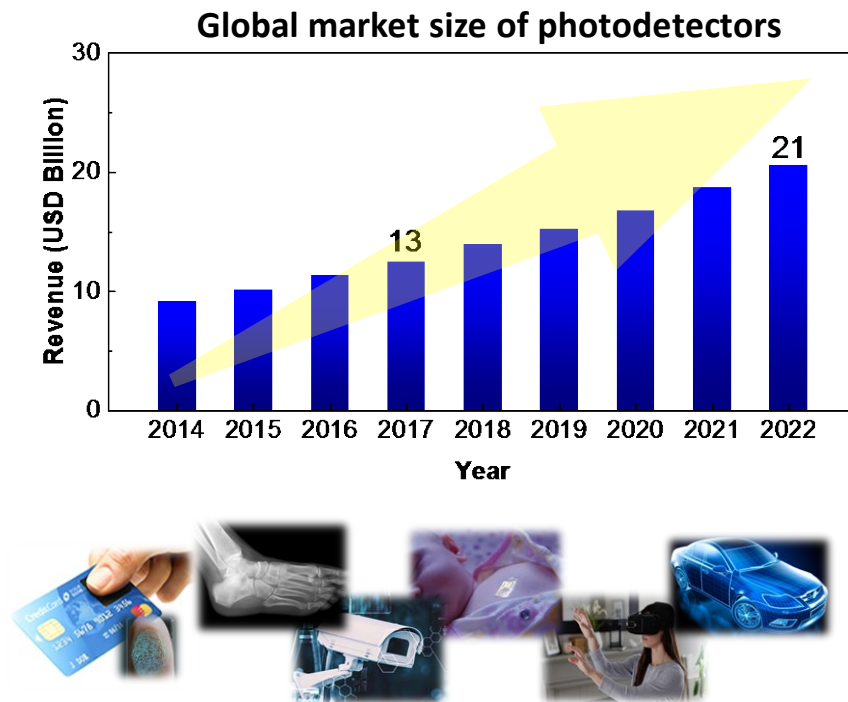


Figure 1.1 Photodetector market size and applications (5).

1.2 Current Technologies of Photodetectors

There are many different photodetectors technologies currently available in the market. Photomultiplier tubes (PMTs) can reach a photon-counting regime with the use of an external photoelectric effect in a vacuum tube. The photoelectrons are accelerated and focused by a dynode and generate secondary electron emission. After multiple stages of secondary emission, these photoelectrons are collected at an anode with a specific gain. PMTs are superior in short response time, low noise, and high gain; therefore, they are widely used in medical equipment and analytical instruments. However, they are bulky, need to be operated at high voltages, and are expensive.

Silicon photomultipliers (SiPMs) are another type of device that can reach the photo-counting regime, composed of an avalanche photodiode and a quenching resistor in a pixel (refer to microcell) connected in parallel into a dense array. The density of a typical SiPM is hundreds to thousands of microcells per mm^2 , and the active areas range from 1 to 50 mm^2 . SiPM features low-power operation, uniform response, and insensitivity to magnetic fields, providing an alternative to medical imaging and bio-photonics areas.

Solid-state single devices such as PIN photodiodes or avalanche photodiodes (APDs) with a diode structure is widespread distributed in microelectronic devices and communication networks. Photons are absorbed in the silicon-based active layer and then generate electron-hole pairs. By applying a reverse bias, the free carriers are accelerated by the electrical field across the depletion region toward the electrodes on the opposite sides. The PIN photodiodes only allow the responsivity less than one without an internal

gain, so APDs are developed for signal amplification. Applying a high voltage in the range of 100-200 V introduces impact ionization, leading to an internal current gain of ca. 100.

State-of-the-art photodetectors based on crystalline inorganic semiconductors, processed with high temperatures typically onto rigid-form substrates, introduce challenges for developing flexible and large-area devices at low cost (6-9). In contrast, organic photodetectors show great potential to deliver simple processes, low-cost fabrication, lightweight, low process temperature, and the mechanical stretchability that fill the niche for next-generation technology (10-13). Moreover, the electrical and optical properties of organic materials can be easily tailored through chemical synthesis (14, 15).

Organic photodetectors have been realized into two structures: organic photodiodes (OPDs) and organic phototransistors (OPTs) (16). OPTs are operated in the photoconductive mode combined with inherent current amplification properties due to the transistor structure, enabling to a high responsivity more than 1,000 A/W at low irradiance (17). However, the photocurrent relying on the trap sites in the active layer results in long response times, ranging from hundreds of milliseconds to several seconds, which limits the use of applications (16, 18-21). On the contrary, OPDs enable fast response, low noise and low-voltage operation, providing more versatility in the design of electronics. In this thesis, we will discuss the photodetectors based on a diode structure.

1.3 Development of Organic Photodiodes

OPDs are optoelectrical devices composed of organic materials in a photoactive layer that generate photocurrent or photovoltage in response to incident light. They have been widely studied in various applications, such as organic photodetectors and organic photovoltaic (OPV) cells, or so-called organic solar cells. Photodetectors and photovoltaic cells share similar structures but generate photoresponse under different operation modes. Additionally, the metrics of OPDs and OPVs are different. For example, high power conversion efficiency in photovoltaic cells is desired, while the detectability of photodetectors in sensing low-level optical power is essential.

The rapid achievements in organic photodetectors in the diode structure primarily benefit from the grateful developments in OPVs in the recent early decades. The photovoltaic effect was first disclosed in Becquerel's work in 1839. He demonstrated the generation of currents in a loop comprised of two silver halides-coated metal and liquid electrolytes under broadband solar illumination (22). The pioneering work led the foundation for tremendous photosensitive applications. The next milestone was reached in 1954 when Chapin, Fuller, and Pearson at Bell Laboratories designed a silicon-based photocell with a p-n junction that generated approximately 6% power conversion efficiency under solar radiation (23).

In 1986, Tang reported a bilayer heterojunction cell and showed that excitons diffuse through the bulk and separate into free carriers at the donor/acceptor (D/A) interface. He used copper phthalocyanine (CuPc) as a donor and a perylene tetracarboxylic derivative (PV) as an acceptor in the photoactive layer. The structure of this organic photodiode was

ITO/CuPC/PV/Ag with an open-circuit voltage (V_{OC}) of 450 mV, a short-circuit current density (J_{SC}) of 2.3 mA/cm², and power conversion efficiency of around 0.9% under 75 mW/cm² AM2 illumination. This demonstration was a significant breakthrough to generate photovoltage and photocurrent in organic-based cells. In 1993, Sariciftci et al. reported a diode composed of a solution-processed conjugated polymer as a donor, poly(phenylene-vinylene) (MEH-PPV), and an evaporated fullerene (C₆₀) (24). Since then, plenty of solution-processed OPDs have been widely investigated for simplification of the fabrication methods.

The major challenge of OPDs with a bilayer structure is to generate photocurrent efficiently due to a short diffusion length of excitons. Excitons created in photoactive layers need to diffuse to the D/A interface and then dissociate before recombination; otherwise, it will decrease the photocurrent. To overcome the issue, in 1994, Heeger, *et al.* introduced the concept of bulk heterojunctions (BHJ), a blend of donor and acceptor layer where produces interpenetration of two domains in bulk, mixed with MEH-PPV (as donors) and C₆₀ (as acceptors) (25). The interpenetration of donor and acceptor shortens the distance that excitons travel to the D/A interface and in the meantime creates more D/A interfaces that facilitate exciton dissociation, and therefore improve the photocurrent. In 1995, Yu and Heeger showed that a BHJ device comprised of MEH-PPV and cyano-PPV (CN-PPV) yields external quantum efficiency (EQE) values in excess of 80 % at -10V (26). An OPD made of BHJ not only enhances the photo-generated current but also provides ease of fabrication. Thus, BHJ is currently the most prevalent architecture in solution-processed OPDs.

In 1994, the Heeger group presented polymeric OPDs made from poly(3-octyl thiophene) (P3OT) and MEH:PPV sensitized with C₆₀, which is the first solution-processed BHJ-based OPD (27). The device structures are ITO/P3OT/Au and ITO/MEH-PPV:C₆₀/Ca, respectively. In this work, these OPDs biased at -10 V show uniform spectral responsivity in visible and near UV region. In addition, the P3OT-based OPDs biased at -15 V show responsivity values larger than 0.3 A/W from 350 to 550 nm, which outperform commercial UV-enhanced Si photodiodes (Si PDs). Since then, OPDs gain numerous attention in the literature on improving the figure of merits to be comparable with inorganic counterparts. A low-noise fullerene-based OPD with a cross-linkable buffer layer enables an linear dynamic range value of 90 dB, greater than that of GaN photodiodes (50 dB) for UV sensing as well (28). A thermal-evaporated donor/acceptor alternating multilayer stack as a photoactive layer in OPDs enables sub-nanosecond response time, which is comparable to that of Si PDs (29).

OPDs currently show specific detectivity (D^*) values in the range of 10^{12} - 10^{13} Jones at room temperature in the visible spectrum (30, 31), comparable to those of commercial Si PDs. In fact, to realize high-detectivity OPDs, a drastic reduction in the spectral noise current in the dark is required. Although an increase of responsivity (R) improves D^* , R has limited improvement in OPDs. On the other hand, orders of magnitude decrease in the dark current (I_{dark}) or increase in shunt resistance values contribute to a significant increase in D^* . In the past few decades, some strategies have been showed to obtain a decreased dark current, such as incorporation of a thick active layer that reduces pinholes (32), introduction of electron/hole blocking layers that hinders undesired recombination on the

electrode interface (31, 33), or the use of large optical bandgap organic semiconductors in the photoactive layer that suppresses thermal-generated carriers (34).

A seminal work in 2009 was reported by Gong, *et al.* demonstrating a high-performance OPD that exhibits D^* in the range of 10^{13} - 10^{14} Jones from 300 to 1450 nm. The device structure was ITO/PEDOT/PS-TPD-PFCB/PDDTT:PC₆₁BM (150 nm)/C₆₀/Al, where PS-TPD-PFCB and C₆₀ acted as injection blocking leading to a low dark current density (J_{dark}) value of 600 pA/cm² at -0.1 V (31). In 2014, Armin *et al.* reported that an increased thickness of PCDTBT:PC₇₁M photoactive layer results in a J_{dark} value of 200 pA/cm² measured at -0.2 V (32).

1.4 Flexible and Printed Organic Photodiodes

The recent increased prevalence of image sensors and rapid growth of the internet of things drives development of lightweight, low-power, and cost-effective electronics. In addition, with advances in the field of biomedical science and robotics, innovations in wearable and disposal sensors have attracted tremendous attention. The market for wearable sensors is continuously growing and is predicted to reach \$5.5 billion by 2025 (2). Now wearable sensors employing inorganic optoelectronics dominate the market, because the sophisticated silicon technology has been well studied and developed for years. However, state-of-the-art inorganic electronic devices are bulky and rigid, impeding sensing reliable physiological signals in movement. To reduce motion artifacts and improve signal-to-noise ratio (SNR) for wearable sensing applications, many methods have been studied, including optimizing the sensing distance, rearranging sensor geometry, or

enhancing algorithm on a microcontroller (2, 35-38). However, those solutions usually in the meantime come with a complicated design that necessitates additional power consumption and/or fabrication cost. Despite the challenges, the conformability of flexible optoelectronics provides mechanically compatible contact with detection parts (39-42), enabling improved signal qualities and therefore lowering power consumption. As a result, interest in developing flexible and stretchable optoelectronics is blooming, and they are believed to become a game changer for next-generation technology (14, 41-47).

Organic semiconductors show great potential to realize flexible electronics at low cost. In addition, they deliver ease of process, tailorable optoelectronics properties, compatibility for large-area roll-to-roll manufacturing, and accessibility to integrate with organic-inorganic hybrid components (32, 48-51). Benefiting from these desirable attributes, OPDs are promising candidates as flexible photodetectors. Pierre *et al.* reported full-printed OPD arrays on polyethylene naphthalate (PEN) substrates, yielding a shot-noise dominated D^* value of 3.45×10^{13} Jones biased at -5 V. They blade-coated electron-collecting layers and photoactive layers, and screen-printed electrodes uniformly on centimetric scales (52). Azzellino *et al.* reported fully inkjet-printed BHJ OPDs on PEN substrates with a high EQE value in excess of 80% (53). Lochner *et al.* realized all-organic pulse oximetry by integrating organic light-emitting diodes and a flexible OPD. The OPD was fabricated by blade-coating on a PEN substrate, yielding a dark current value in the range of nA/cm^2 in reverse bias (49).

1.5 Current Challenges of Organic Photodiodes

Although OPDs have made significant inroads into next-generation sensing and imaging devices, several challenges still need to be addressed. First, OPDs show relatively high J_{dark} values. Strategies to increase D^* values in OPDs have focused on reducing i_{dark} by using injection blocking layers (54, 55) and on optimizing the photoactive layer geometry and morphology to reduce defects (56, 57). State-of-the-art J_{dark} values in the hundreds of pA/cm² at -0.2 V have been demonstrated using these combined strategies (16, 32, 52, 57-59). In addition, the flexible OPDs reported in the literature to date show J_{dark} values in the range of nA/cm² (60). However, these values are still orders of magnitude larger than those found in low-noise Si PDs (*i.e.* Hamamatsu S1133, in the pA/cm² range) and have limited improvement since 2014. In fact, J_{dark} values are determined by the shunt resistance and also by the reverse saturation current density, which we will discuss in this thesis.

Second, the intrinsic disorder structure and carrier transport mechanism in organic materials consequently leads to modest charge mobility values in the range of 10⁻⁵ to 10⁻¹ cm²/Vs in the vertical direction, resulting in a lag response time in the OPDs compared to that in their inorganic counterparts (61). The slow response limits their prevalence in applications, particularly for thick devices. The solution-processed BHJ OPDs show bandwidth from sub-MHz to tens MHz (16), while Si photodiodes provide a bandwidth in the range of GHz. Thin OPD devices enable faster response, but they also present high dark current values leading to high noise that limits the detectivity. To solve this issue, we provide a solution, which will be discussed in the following chapter.

In addition, environmental and operational stabilities of OPDs are also important for the commercialization of organic electronics. Molecular additives have been demonstrated to improve the stability of OPVs (62), and a bilayer gate dielectric using atomic layer deposition has been shown to obtain high operational stability in organic thin-film transistors (63); Yet, few systematic stability study on OPDs have been reported in the literature.

Next, stretchable OPDs have been investigated only recently. However, the reduction of carrier transport by introducing elastomers in organic materials and the existence of leakage paths in the bulk after stretching leave challenges in the development of high-performance stretchable OPDs. In addition, the development of stretchable transparent electrodes is also a key role to achieve a stretchable OPD.

1.6 Objectives of the Research

The objective of the research is to develop high-performance OPDs for sensing low illumination. OPDs can be fabricated into devices with a flexible form factor using coating and printing techniques. These techniques are scalable and therefore enable large-area devices and arrays.

First, we investigate the origin of the dark current and select a proper material combination that yields low-noise photodiodes. The optimized OPDs exhibit low J_{dark} values comparable to those of state-of-the-art Si photodiodes at low voltages. Without adding more complexities in the fabrication, we demonstrate large-area OPDs on plastic

substrates with limited dark current values leading to a high D^* value (10^{14} Jones) operating at high frequency. This competes with that of rigid Si counterparts of similar size. Flexible and large-area OPDs are designed with a novel geometry to record photoplethysmogram (PPG) for applications in physiological sensing. Their highly conformal form factors, combined with the new geometry, provide improved optical power collection compared to conventional small-area Si-based detectors. Our work establishes that OPDs can yield unprecedented D^* values that are comparable to those of low-noise inorganic counterparts but at lower voltage and under room temperature operation. In addition, the large-area and flexible OPDs are shown to improve the signal-to-noise ratio for PPG and therefore can potentially be used in low-power wearable electronics.

Next, to develop a universal method for lowering the dark current of OPDs with low shunt resistance, we treat organic active layers with oxide species using atomic layer deposition (ALD) to passivate defects. We exhibit reduced dark current values in reverse bias after using this interfacial treatment for P3HT:ICBA and PDPP3T:PC₇₁BM devices. Then we fabricate a thin active layer treated with ALD for the purpose of improving the response time of OPDs and of studying their irradiance-dependent response dynamics.

1.7 Structure of the Dissertation

In chapter 2, the fundamentals of organic semiconductors, semiconductor physics, and device operation principle will be reviewed. An equivalent circuit model that describes a photodiode behavior and the importance of the electrical parameters will be presented. An overview of the figures of merit for organic photodetectors will be given in the end.

In chapter 3, the organic materials used in this research and details of device fabrication will be included. An overview of general device fabrication techniques and characterization methods will also be provided.

Chapter 4 describes the origin of the dark current, which determines the electronic noise characteristics in OPDs. This insight provides us with a proper selection of materials to reach high detectivity value in OPDs.

Chapter 5 demonstrates the flexible and large-area OPDs with high detectivity based on what we learned in chapter 4. An innovative geometry of the OPD is designed to sense PPG signals, achieving a high signal-to-noise ratio.

Chapter 6 provides a superficial treatment using ALD on organic photoactive layers to reduce the dark currents of OPDs with low shunt resistance. This technique is applicable to various systems with thin photoactive layers, providing a method to develop high-performance NIR OPDs or to improve the response time in OPDs.

CHAPTER 2. BACKGROUND

2.1 Organic Semiconductors

Organic semiconductors are carbon-based materials with semiconducting properties that can be used as active layers in optoelectronic devices such as photodiodes, light-emitting diodes, and transistors. The electron configuration of carbon is $1s^2 2s^2 2p^2$, and the four valence electrons occupy $2s$, $2p_x$, and $2p_y$ orbitals.

When a carbon atom is in the presence of an external perturbation with nearby atoms, such as carbon, hydrogen, oxygen, one of the electrons in the $2s$ orbital will promote to a $2p_z$ orbital, and these orbitals may hybridize into $2sp$, $2sp^2$, or $2sp^3$ orbitals as the outer-shell orbitals of a carbon atom. In organic molecules, electron interactions between carbon atoms form either σ or π molecular orbitals. While the σ molecular orbitals result from the head-on overlap of two atomic hybridized orbitals, π molecular orbitals arise from the side-by-side overlap of two off-plane p_z atomic orbitals. For example, the outer-shell orbitals of ethylene molecules hybridize into three identical $2sp^2$ orbitals and leave one unhybridized $2p_z$ orbital. The overlap of $2sp^2$ orbitals in the plane creating σ orbitals, and the unhybridized $2p_z$ orbitals perpendicular to the plane create π orbitals.

The existence of delocalized electrons in π orbitals leads to the semiconducting properties in organic materials. In the first approximation, optical and electrical properties are governed mainly by electrons in π molecular orbitals, so the electrons in σ molecular orbitals can be ignored. According to the framework of molecular orbital theory (Hückel theory), molecular orbitals consist of linear combinations of atomic orbitals. In the ethylene

molecule for instance, the supposition of two atomic $2p_z$ orbitals, $|\varphi_1^{2p_z}\rangle$ and $|\varphi_2^{2p_z}\rangle$, results in the formation of two molecular orbitals. A low-energy state composed of the symmetric linear combination of two the $2p_z$ orbitals, $|\pi\rangle \propto |\varphi_1^{2p_z}\rangle + |\varphi_2^{2p_z}\rangle$, shows a high probability of finding electrons between the two carbon atoms, referred to as a π bonding orbital. On the other hand, a high-energy state composed of an antisymmetric linear combination of two the $2p_z$ atomic orbitals $|\pi^*\rangle \propto |\varphi_1^{2p_z}\rangle - |\varphi_2^{2p_z}\rangle$, which shows a lower probability of finding electrons and is called an antibonding orbital or π^* orbital. The energy levels are shown in Figure 2.1.

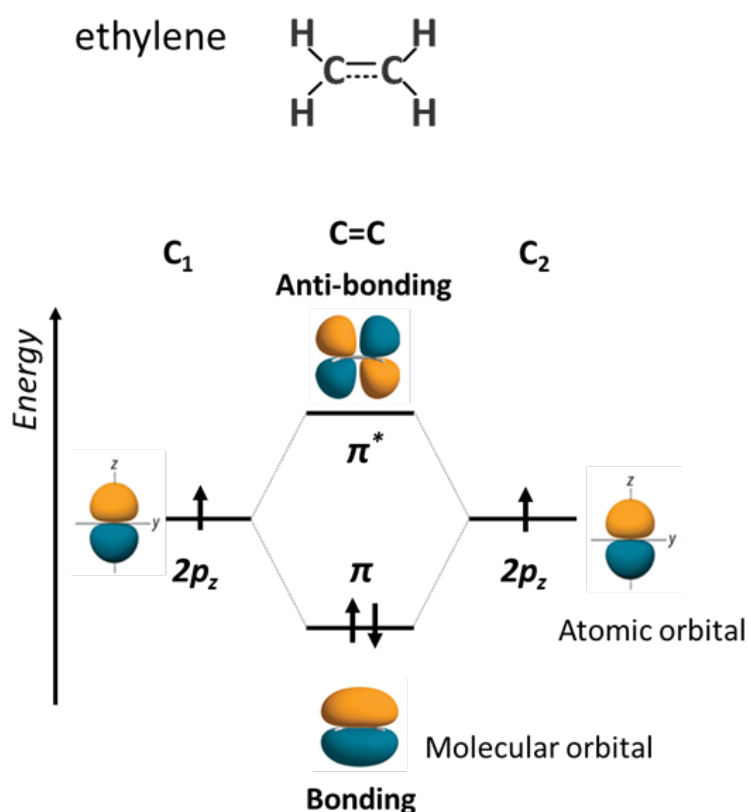


Figure 2.1 Ethylene chemical structure and energy levels of atomic orbitals and molecular orbitals in an ethylene molecule.

In larger polyene molecules, in which more carbon atoms are connected, the alternation of single and double bonds between adjacent carbon atoms leads to highly delocalized π -electrons. Such molecules with alternating single and double bonds are referred to as conjugated molecules. In 1,3-butadiene (linear polyene molecule with 4 carbon atoms), the molecular orbitals are constructed from linear combinations of four $2p_z$ atomic orbitals, yielding a total of four molecular orbitals. Two of these orbitals are bonding and two are anti-bonding molecular orbitals. In the ground state and at low temperature, each bonding orbital contains two electrons with opposite spin due to the Pauli exclusion principle, and the antibonding orbitals are empty (in the first approximation ignoring thermodynamics for now), which corresponds to a total of four π electrons for 1,3-butadiene since the molecule is comprised of four carbon atoms and each atom contributes one π electron.

An increase in conjugation results in more and more π and π^* molecular orbitals. In particular, the highest molecular occupied orbital among these π orbitals is called HOMO, and the lowest unoccupied molecular orbital among these π^* orbitals is called LUMO, shown in Figure 2.2. In the first approximation, only the HOMO and the LUMO are mainly responsible for the optical and electrical properties of the molecule. These two orbitals are called “frontier” orbitals, and the other orbitals are ignored.

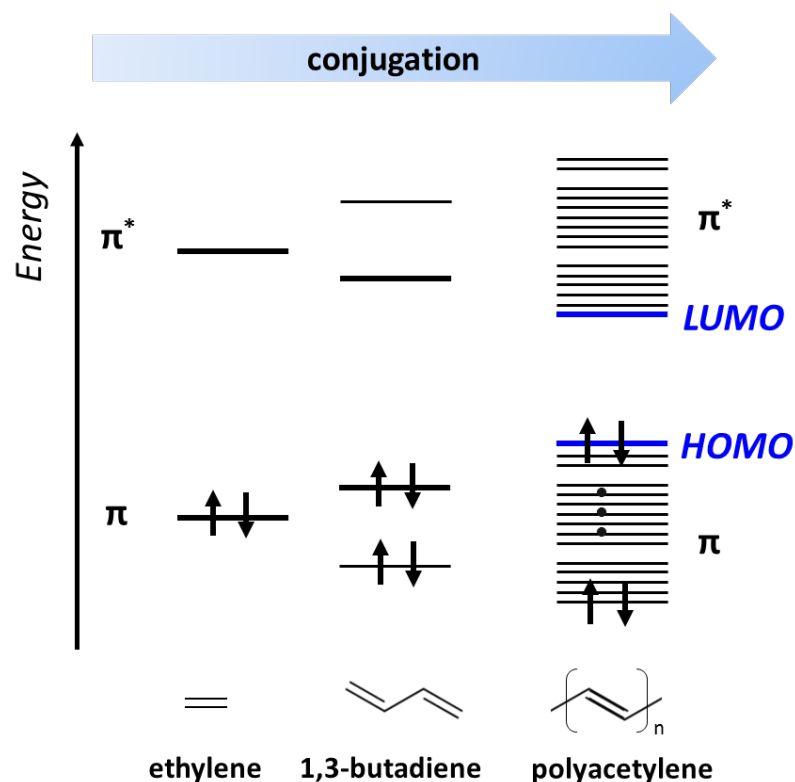


Figure 2.2 The energy levels and formation of LUMO and HOMO in conjugated molecules.

The energy gap between LUMO-HOMO ($E_{LUMO-HOMO}$) is an important parameter for the description of the optical properties of organic semiconductors. In the molecular case, the fundamental gap (E_{fund}) is defined as the difference between ionization energy (IE) and electron affinity (EA), which indicates that minimum energy is required to remove an electron (oxidize) and add an electron (reduce) to a molecule, respectively. IE can be measured by gas-phase ultraviolet photoelectron spectroscopy, and EA by gas-phase inverse photoemission spectroscopy. E_{fund} is measured with charged molecular species, so it is generally not equal to $E_{LUMO-HOMO}$ calculated for neutral molecules.

In a solid film, when a large ensemble of organic molecules forms a solid bulk, due to intermolecular and intramolecular interaction, HOMO and LUMO levels will broaden into a HOMO manifold and a LUMO manifold, respectively, which are analogous to the valence band and conduction band in inorganic materials. The transport gap (E_{trans}) for free carriers is often defined as the energy difference between the IE and the EA. Figure 2.3 illustrates the energy level. E_{trans} is often evaluated in the first approximation from cyclic voltammetry experiments in which oxidation and reduction potentials provide information on the energy required to remove (oxidize) or add an electron (reduction) to molecules in a solution. The optical gap (E_{opt}) is the energy difference between the ground state and the lowest optically accessible excited state when the Coulomb interaction between a positively charged hole and a negatively charged electron takes place. In this case, the first excited state consists of a bound electron-hole pair referred to an exciton. The difference between the E_{fund} and the E_{opt} is the exciton binding energy E_B .

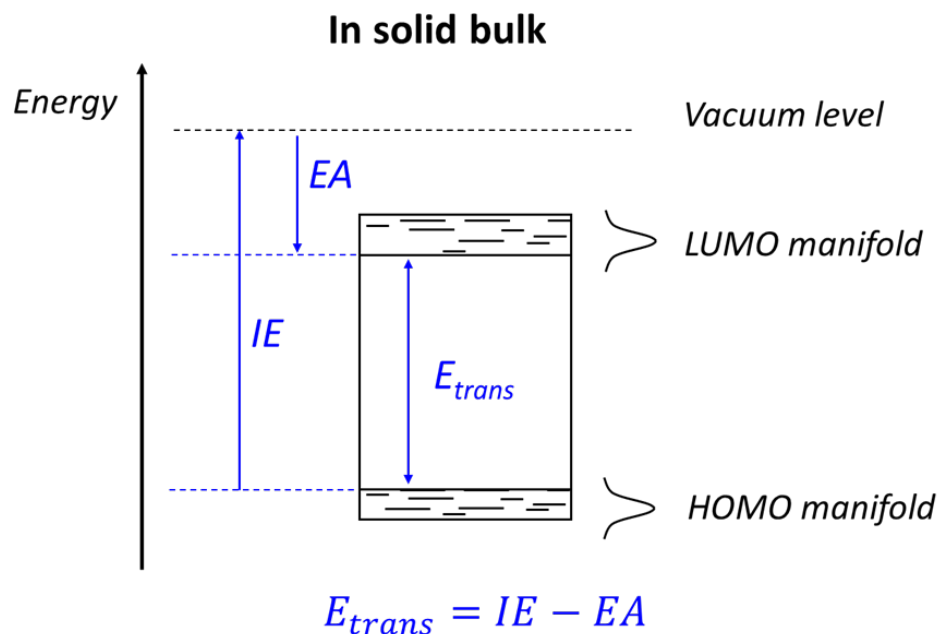


Figure 2.3 Energy levels in organic solid bulk.

The photophysical properties of organic molecules are also described in terms of electronic state diagrams (also called Jablonski diagrams). In the ground state, the spin of the two electrons in the HOMO must be antiparallel because of Pauli exclusion principle, yielding a total spin value of zero. Therefore, the ground state is a singlet state called S_0 . In the excited state, one electron is in the HOMO and one is in the LUMO. The electrons are in different orbitals that can be paired in a different fashion and form either singlet excited states (S_n) or triplet excited states (T_n) (64). Because of selection rules, in the first approximation, only optical transitions between S_n states are allowed, and the optical property is usually considered only the ground state S_0 and the first singlet excited state S_1 .

2.2 Semiconductor Physics

2.2.1 Fermi Level Energy Under Equilibrium

The Fermi level energy (E_F) is the average electrochemical potential of a particle in a large ensemble under thermal equilibrium, which means that the net energy exchange in a system is zero; that is, every microscopic process is balanced by its reverse process. The occupation probability of an allowed energy state with energy E is given by the Fermi-Dirac distribution function, $f(E)$:

$$f(E) = \frac{1}{1 + e^{(E-E_F)/kT}} \quad (1)$$

where E_F is the Fermi level energy in eV, T is the temperature of the system in Kelvin, and k is the Boltzmann constant. When a system achieves thermal equilibrium, E_F is consistent across the entire semiconductor. For non-degenerate semiconductors (*i.e.*, $|E - E_F| > 3kT$), the E_F lies within the bandgap, and $f(E)$ can be approximated to

$$f(E) = \frac{1}{1 + e^{(E-E_F)/kT}} \cong e^{-(E-E_F)/kT} \quad (2)$$

Under thermal equilibrium, the intrinsic carrier concentration of electrons (n_0) and holes (p_0) can be derived from the Fermi-Dirac distribution and the density of states of all possible states, expressed by

$$n_0 = \int_{E_C}^{\infty} g_C(E) f(E) dE \quad (3)$$

$$p_0 = \int_{-\infty}^{E_V} g_V(E)(1 - f(E))dE \quad (4)$$

where $g_C(E)$ is the density of states of the conduction band (or the LUMO manifold), and $g_V(E)$ is the density of states of the valence band (or the HOMO manifold).

Thus, Equation (3) and (4) yield

$$n_0 = N_C e^{-(E_C - E_F)/kT} \quad (5)$$

$$p_0 = N_V e^{-(E_F - E_V)/kT} \quad (6)$$

where E_C is the energy at the conduction band edge, E_V is the energy at the valance band edge, N_C is the effective density of states per unit volume in the conduction band, and N_V is the effective density of states per unit volume in the valance band.

2.2.2 Fermi Level Energy Under Non-Equilibrium

Once a system is in the presence of an external perturbation, such as illumination, temperature variation, or applied bias, the net exchange energy of the system leads to an extra generation of electrons and holes under the quasis-equilibrium condition. The electron and hole concentration can be expressed as follows:

$$n = n_0 + \Delta n = n_i e^{-(E_i - F_n)/kT} \quad (7)$$

$$p = p_0 + \Delta p = p_i e^{-(F_p - E_i)/kT} \quad (8)$$

where Δn (Δp) is the excess electron (hole) concentration, n_i (p_i) is the intrinsic electron (hole) concentration, F_n (F_p) is the quasi-Fermi level energy for electrons (holes), and E_i is the intrinsic Fermi level energy. It is noted that Fermi level energy across the system is no longer consistent but splits into quasi-Fermi level energies with respect to the carrier concentrations, expressed by

$$F_n = E_c + kT \ln\left(\frac{n}{N_c}\right) \quad (9)$$

$$F_p = E_v - kT \ln\left(\frac{p}{N_v}\right) \quad (10)$$

2.2.3 Carrier Generation/Recombination

Carrier generation/recombination is a key process taking place in semiconductors that determines the performance of a photodiode. In organic photodiodes, the generation of excess carriers is induced by incident photons while recombination is the reverse process of generation, that is, the relaxation process toward a steady state. Recombination can be carried out by two processes. One is band-to-band recombination, in which an electron from the conduction band recombines with a hole from the valence band and can be involved in a radiative, non-radiative, or Auger mechanism. Particularly, radiative recombination means that the relaxation process accompanied by the emission of photons

associated with release of energy. Non-radiative recombination occurs when the relaxation process transfers energy to phonons, and Auger recombination occurs when energy transfers to a secondary electron and promotes it to a higher excited state. When a system reaches the principle of detailed balance, that is, the same amount of thermal generation and recombination of carriers, the generation and recombination rate can be expressed as follows:

$$G = R_{eq} = Bnp = Bn_i^2 \quad (11)$$

where G is the generation rate, R_{eq} is the recombination rate, and B is the recombination coefficient.

The other type of recombination process is so-called trap-assisted Shockley-Read-Hall (SHR) recombination, involving trap centers within the bandgap of a material. This recombination includes a two-step process. The recombination rate reaches a maximum value when the energy of the trap level is in the mid bandgap.

2.3 Working Principles of Organic Photodiodes

2.3.1 Device Structure

Organic photodiodes (OPDs) consist of an organic photoactive layer and two electrodes with a work function difference. The photoactive layer acts as a light absorber and is sandwiched between two electrodes with different work function values. A

photoactive layer can be formed by two structures: (i) a bilayer heterojunction, which is a stack of two separate donor/acceptor layers or (ii) bulk heterojunction, a mixed layer of donors and acceptors. Figure 2.4 Basic structure of OPDs. shows the basic structure of OPDs.

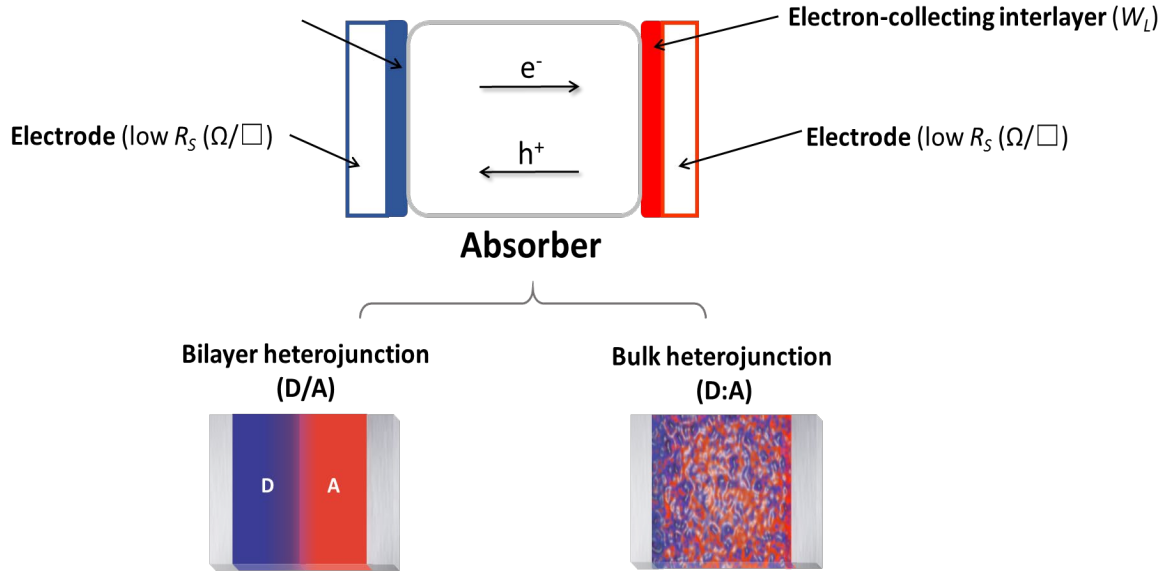


Figure 2.4 Basic structure of OPDs.

The high work function electrode collects holes, and the low work function electrode collects electrons. One of the electrodes is semi-transparent allowing incident light to penetrate the absorber, and the other one serves as a light reflector. In general, each electrode serves two purposes: It is conductive (low sheet resistance), so it collects current without introducing significant Joule loss; and it has a specific work function. These two properties can be provided by one material or by two adjacent materials. In the latter case, the electrode serves as a conductor and the work function is defined by a so-called charge-

collecting layer. Electron (hole) collection is most efficiently conducted using low (high) work function materials.

The direction of current flow defines two the architectures of organic photodiodes: conventional and inverted structures. The conventional structure collects electrons from the top electrode, while the inverted one collects electrons from the bottom electrode, shown in Figure 2.5. For some organic photodiodes, photoresponse performance is structure dependent, affecting the incident light distribution and current transport, leading to different spectral responsivity values or the linear dynamic range (for OPDs), or different open-circuit voltage (V_{OC}) and short-circuit current density (J_{SC}) values (for OPVs). In this research, we mostly focus on the inverted structure.

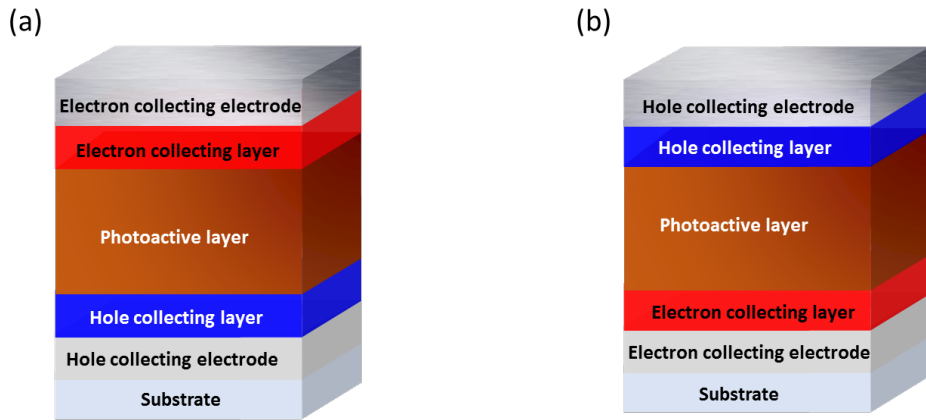


Figure 2.5 (a) The conventional structure, and (b) the inverted structure.

Organic semiconductors, unlike their inorganic counterparts, possess high extinction coefficients, resulting in efficient light harvesting in photoactive layers with a relatively small thickness in the range of 200-500 nm. In contrast to the inorganic layer of semiconductor devices, the organic photoactive layer, which primarily consists of two

intrinsic materials as the donor and the acceptor, preferentially transports holes and electrons, respectively. To be energetically favorable for charge injections from electrodes, hole transport materials are selected from donor-like materials with low IE while electron transport materials are selected from acceptor-like materials with high EA. In general, state-of-the-art donors used in organic photodiodes and organic solar cells are small molecules or conjugated polymers, while acceptors are often fullerene derivatives.

2.3.2 Donor/Acceptor Interfaces

Absorption of a photon in a semiconductor excites an electron from HOMO to LUMO, leading to the formation of an exciton, an electron-hole pair bound by Coulomb attraction. Organic semiconductors present low dielectric constant values, and the binding energies of an exciton vary from 0.2 eV to 1.5 eV (65), at least one order of magnitude larger than thermal energy at room temperature (RT) (66), 25.9 meV, as a result of the moderate dielectric screening of the Coulomb interaction. Hence, excitons formed in organic semiconductors are mostly stable and need to be dissociated before they can contribute to currents. The condition is in contrast with that of inorganic semiconductors (e.g., Si), in which the exciton binding energy is less than the thermal energy at room temperature, leading to the efficient dissociation of excitons into free electron-hole carriers.

Excitons, however, are able to dissociate efficiently at donor/acceptor (D/A) interfaces. At the D/A interface, the electronic coupling of donor and acceptor molecules leads to the formation of charge-transfer states (CT) with decreased energy, shown in Figure 2.6. The excitons become a weakly Coulombically-bound pair in the CT state and

tend to dissociate into charges in the presence of disorder or dipoles at the interface (64). Therefore, a bulk heterojunction (BHJ) consists of a blend of donors and acceptors that form an interpenetrating network for accumulating D/A interfaces to improve exciton dissociation. In bulk solids, intermolecular interactions cause energetic disorder and broaden molecular electronic levels into manifolds. The EA manifolds of the acceptor (*i.e.*, EA(A)), and IE manifolds of the donor (*i.e.*, IE(D)) are analogous to the valence and conduction bands, respectively, of an inorganic system. The free charge carriers are transported via thermal-activated hopping through intermolecular means and then collected by electrodes on both sides to generate current.

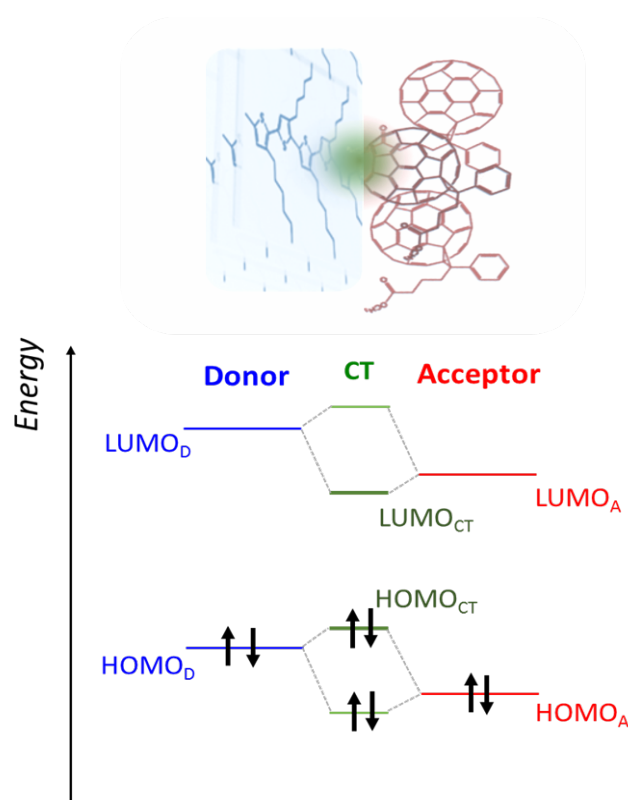


Figure 2.6 Representation of the formation of charge-transfer (CT) states at the molecular level.

2.3.3 Operation of Organic Photodiodes

The photocurrent of photodiodes is generated by the free carriers swept in opposite directions by applied bias. The asymmetry of silicon photodiodes stems from the p- and n-doped regions, and the built-in electrical field forms across the depletion region. Minority carriers created in p and n regions of the diode are swept to the other side of the junction and then are collected by electrodes. Analogous to silicon photodiodes, organic photodiodes achieve asymmetry by the use of D/A interfaces that facilitate charge separation and by the use of two electrodes with high contrast work function values. After exciton dissociation, free electrons accumulate in the LUMO manifold of the acceptor material (electron-transport material), and the holes accumulate in the HOMO manifold of donor material (hole-transport material). Therefore, LUMO of the acceptor and HOMO of the donor, in general, represent the relevant absorber energy levels.

The use of electrodes with a high work function contrast can be realized by the difference in the inherent work function of electrodes or by applying additional work function modifier on electrodes. High work function (W_H) electrodes are chosen to match the HOMO of the donor materials, forming an ohmic contact for hole injection. Low work function (W_L) electrodes, by contrast, are chosen to match the LUMO of the acceptor materials. After the layers make contact, the Fermi level energy will align under thermal equilibrium, leading to a ϕ_{bi} value across the absorber, $q\phi_{bi} = W_H - W_L$. Figure 2.7 shows the relevant energy levels before and after contact in a dark condition.

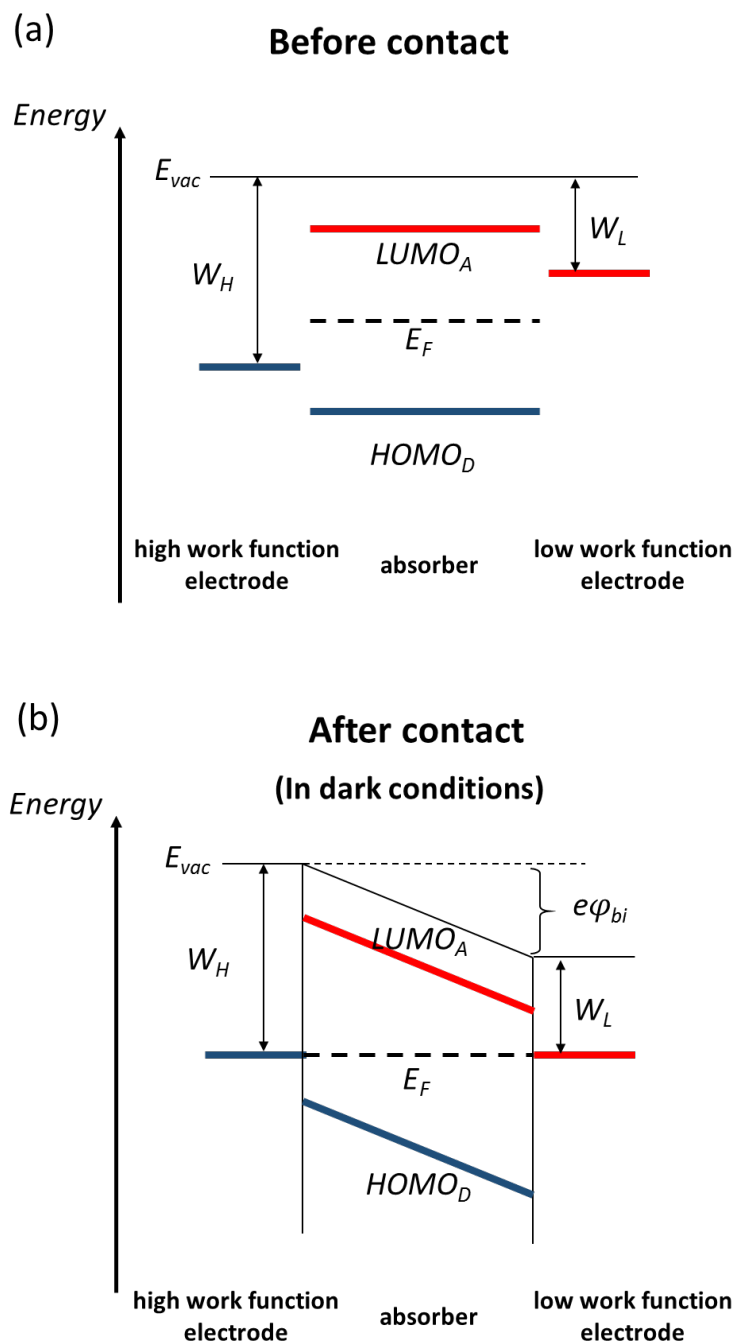


Figure 2.7 Energy levels of layers of organic photodiodes (a) before contact and (b) after contact in a dark condition.

While organic photodiodes are under illumination, photons generate excess electrons and holes in the photoactive layer, resulting in the formation of quasi-Fermi level energies, discussed in Section 2.2.2. Figure 2.8 illustrates F_p in the donor material and F_n in the acceptor material at the electrodes located at $x=0$ and $x=d$, respectively. The gradient of the quasi-Fermi level energies leads to drift photocurrents. In addition, the differences among the quasi-Fermi level energies at electrodes provides photovoltage (V_{ph})

$$eV_{ph} = F_n(x = d) - F_p(x = 0) \quad (12)$$

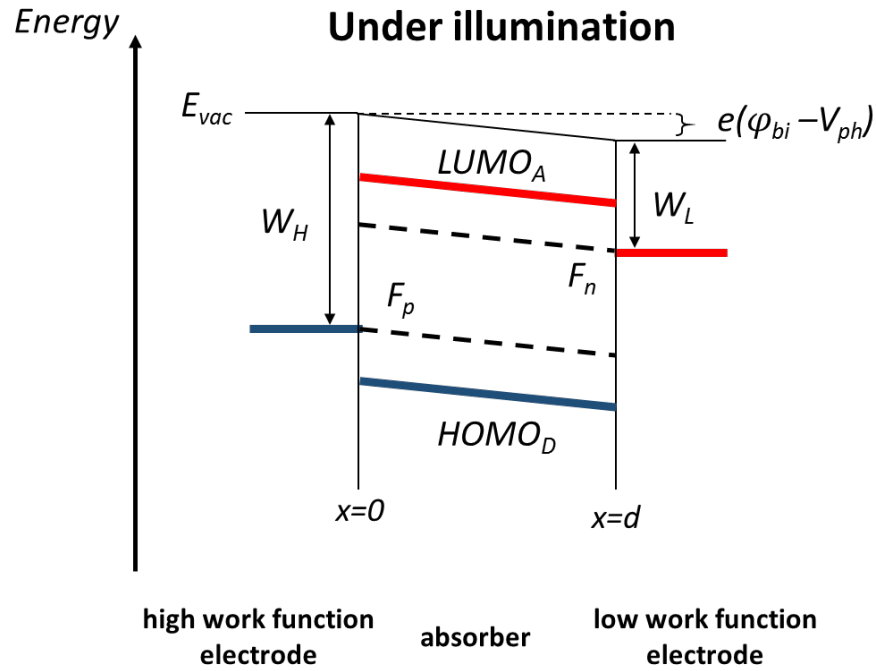


Figure 2.8 Energy levels of layers of organic photodiodes under illumination.

In summary, a device yields the highest photocurrent under short-circuit conditions, indicating photovoltage equal to zero. The differences among quasi-Fermi level energies determine the maximum photovoltage. When the device is under an open-circuit condition, the quasi-Fermi level energies are spatially invariant across the photoactive layer, which indicates that the gradient equals zero; therefore the photocurrent also equals zero.

2.4 Equivalent Circuit Model

An equivalent circuit model of a photodiode is one that rationalizes the electrical characteristics under dark and light conditions. As shown in Figure 2.9 (a), the equivalent circuit is composed of a current source (J_{ph}), a diode, a series resistance (R_s), and a shunt resistance (R_p). The current source represents the photocurrent density with a value of J_{ph} under illumination. The diode describes a current rectification property with a reverse saturation current density of J_o and an ideality factor of n . R_s corresponds to the parasitic resistance of the semiconductor layer, the contact resistance between semiconductors and electrodes, and the resistance from external interconnections. R_p is associated with possible leakage paths that arise from imperfect structures in bulk, such as pinholes.

In this model, the current density and voltage across the photodiode are denoted J and V , respectively. The current-voltage relationship of this circuit is solved based on Kirchhoff's current law, referred to as the Shockley equation:

$$J = \frac{1}{1 + R_s/R_p} \left\{ J_0 \left[\exp \left(\frac{V - JR_s A}{\frac{nkT}{q}} \right) - 1 \right] - \left(J_{ph} - \frac{V}{R_p A} \right) \right\} \quad (13)$$

where kT is thermal energy, q is the elementary charge, and A is the area of the device.

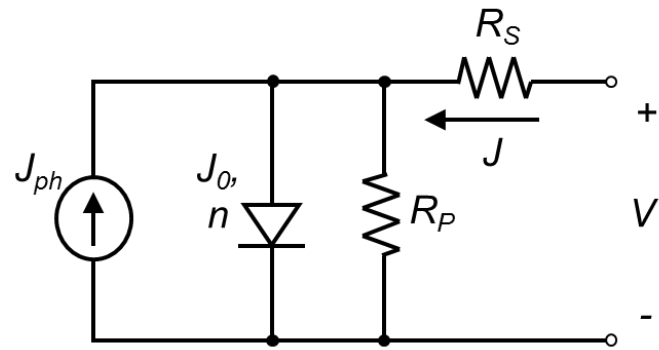
From Equation (1), V_{OC} can be derived when we set J equal to zero, while J_{SC} can be derived when we set V equal to zero, leading to Equations (14) and (15):

$$V_{OC} = \frac{nkT}{q} \ln \left[1 + \frac{J_{ph}}{J_0} \left(1 - \frac{V_{OC}}{J_{ph} R_p A} \right) \right] \approx \frac{nkT}{q} \ln \left(1 + \frac{J_{ph}}{J_0} \right) \quad (14)$$

$$J_{SC} = -\frac{1}{1 + \frac{R_s}{R_p}} \left\{ J_{ph} - J_0 \left[\exp \left(\frac{|J_{SC}| R_s A}{\frac{nkT}{q}} \right) - 1 \right] \right\} \approx -J_{ph} \quad (15)$$

The approximations in Equations (14) and (15) are valid only when the following assumptions are met: (i) $R_p/R_s \gg 1$; and (ii) $J_{SC}/J_0 \gg 1$. A limited R_s value and a high R_p value are desired in a photodiode. R_s limits the current in forward bias, and R_p is related to the dark current in reverse bias. In particular, a low dark current value is essential for a photodetector. Figure 2.9 (b) shows the current-voltage characteristics of photodiodes associated with their parameters (64).

(a)



(b)

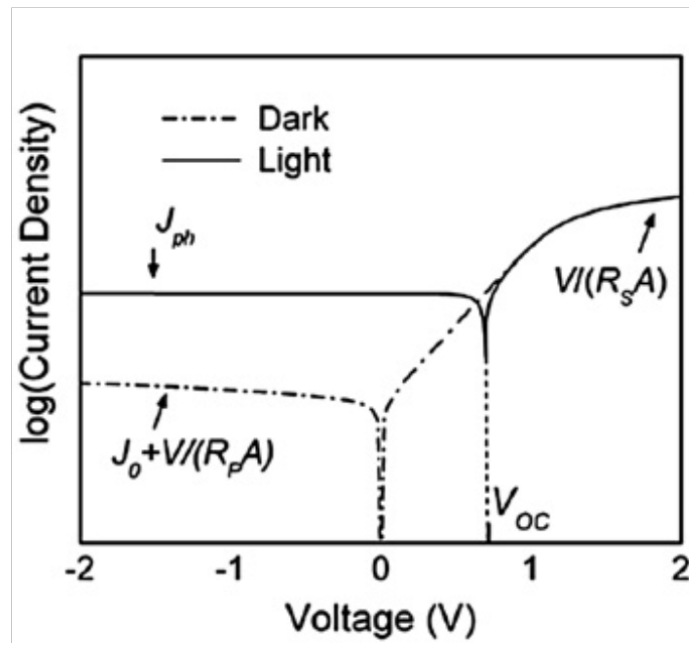


Figure 2.9 (a) An equivalent circuit diagram of a photodiode. (b) J - V characteristics.

2.5 Performance Metrics of Organic Photodiodes

2.5.1 Response Time

The response time of a photodetector is captured by its transient photocurrent responses, following a frequency-modulated optical input, and determines the bandwidth (B) of the photodetector. The response time primarily arises from three components: the drift time of photo-generated carriers, the diffusion time of photo-generated carriers, and the RC time constant associated with external circuits. The rise time (t_r) and the fall time (t_f) are defined by photocurrent increases from 10% to 90% and decreases from 90% to 10%, respectively, shown in Figure 2.10. In terms of the frequency response, the bandwidth of a photodetector is determined by the frequency at which the photocurrent decreases by 3dB. The bandwidth is approximated by $B = 0.35/t_r$ (16).

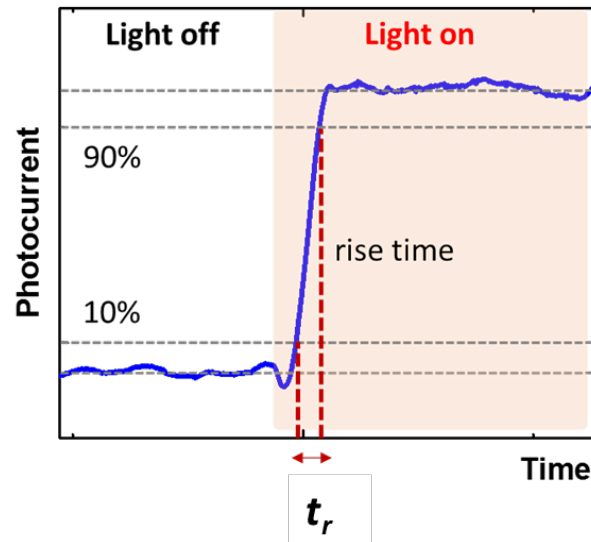


Figure 2.10 Schematics of the response time characterization.

2.5.2 Responsivity

The responsivity (\mathfrak{R}) of a photodetector is defined by the photo-generated current (I_{ph}) per incident optical power ($\phi_{opt}(\lambda)$), the ratio between the electrical output and the optical input. The unit of \mathfrak{R} is in A/W. I_{ph} is in the unit of A, and $\phi_{opt}(\lambda)$ is in the unit of W. \mathfrak{R} is dependent on EQE , indicating the ratio of number of carriers collected in devices to number of incident photons.

$$\mathfrak{R}(\lambda) = \frac{I_{ph}(\lambda)}{\phi_{opt}(\lambda)} = EQE(\lambda) \frac{q}{h\nu} \quad (16)$$

where h is the Plank constant, and ν is the frequency of the incident light. In fact, \mathfrak{R} , which can be variant, is a function of the incident light wavelength, of the optical power, and of the device temperature.

2.5.3 Linear Dynamic Range

The linear dynamic range (LDR), expressed in dB quantifies the operational region, in which the photocurrent shows linearity with optical power. In other words, within this region, \mathfrak{R} values are constant. The LDR is defined as

$$LDR = 20 \log \left(\frac{I_{max}}{I_{min}} \right) \quad (17)$$

In the above equation, I_{min} is the current value at the lower limit of the LDR , and I_{max} is the current value at the upper limit of the LDR . The deviation from the linearity of

photocurrents at high irradiance is rationalized as an indication of increased bimolecular recombination losses for irradiance values at the onset (67) or the impact of high series resistance in OPDs. \mathfrak{R} values, however, are usually variant at low irradiance; that is, the photocurrent decays superlinearly or sublinearly. Charge-trapping effects leading to a photoconductive gain or loss can explain the non-linear behavior (68).

2.5.4 Noise

In photodetectors, low noise that allows for low-light level sensing is desirable. Spurious voltages or currents that interfere with electrical signals are considered noise. In the time domain, noise is quantified as a root mean square (rms) value of the fluctuation of AC signals over a certain measurement of time, depicted in Figure 2.11 (a). In a device, the noise can be represented by the rms value of the current fluctuations ($I_{\text{dark,rms}}$) around a steady-state average dark current value (I_{dark}). I_{dark} is the average value over a set of discrete temporal dark current values ($I_{\text{dark}}(t_j)$), expressed by $I_{\text{dark}} = \langle I_{\text{dark}}(t_j) \rangle$.

As a result, the expression of the electronic noise in a device is shown in Equation (18), in the unit of A.

$$I_{\text{dark,rms}} = \langle (I_{\text{dark}}(t_j) - I_{\text{dark}})^2 \rangle^{1/2} \quad (18)$$

In addition, power spectral density (S_n) describes the noise profile shown in the frequency domain, and the squared value of $I_{\text{dark,rms}}$ is the integral over the selected measurement bandwidth (B), expressed in Equation (19). The noise in the low-frequency

domain is called pink noise, and the noise in the high-frequency domain is called white noise. S_n is in the unit of A^2/Hz .

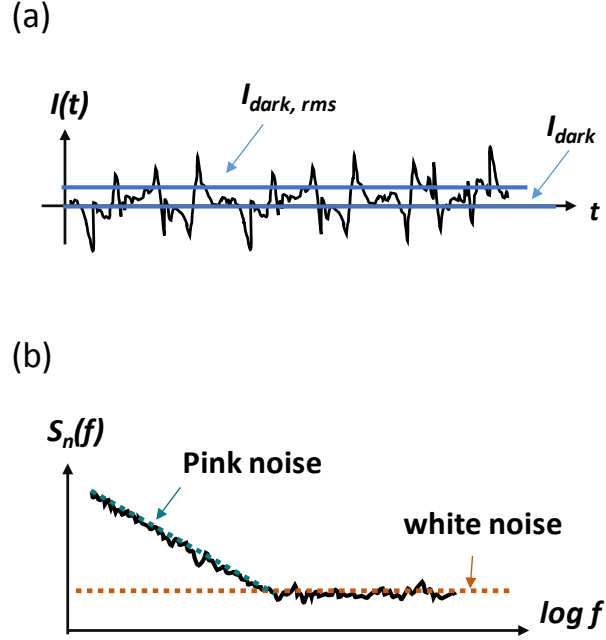


Figure 2.11 (a) Noise represented in the time domain and (b) the power spectral density in the frequency domain.

$$I_{dark, rms}^2 = \int_B S_n(f) df \quad (19)$$

In general, noise is mainly divided into three components: shot noise, thermal noise, and flicker noise or $1/f$ noise. The total power spectral density can be expressed as

$$S_n = S_{shot} + S_{thermal} + S_{1/f} \quad (20)$$

in which,

$$S_{shot} = 2q \left[J_0 \exp\left(\frac{qV}{nkT}\right) + J_0 \right] A \quad (21)$$

$$S_{thermal} = \frac{4kT}{R_p} \quad (22)$$

In the above equation, q is the fundamental charge, J_0 is the reverse saturation current density of a photodiode, V is the applied voltage, n is the ideality factor, k is the Boltzmann constant, T is the temperature in Kelvin, and A is the photodiode area.

Shot noise originates from the discrete single events of photoelectric effects, and the arrival of electric charges follow a Poisson distribution. S_{shot} depends on the reverse saturation current density (69-71), which we will discuss in detailed in the following sections; thermal noise, as a function of shunt resistance in the device, arises from the random thermal agitation of carriers in resistive devices. The first two terms are white noise, a constant value in the spectrum, and flicker noise ($S_{1/f}$) is frequency dependent. In most cases of organic photodetectors with high dark current values operating under reverse bias, shot and thermal noise are dominant contributions to overall spectral noise. Therefore, frequency-dependent noise is typically under-reported in the literature (72). This approach, however, will lead to an overestimated specific detectivity value, which we will discuss in the following sections.

2.5.5 Noise Equivalent Power and Specific Detectivity

Two paramount figures of merit that assess photodiode performance and that account for the spectral noise current are noise equivalent power (NEP) and specific detectivity (D^*). Low NEP or high D^* value leads to high detectivity of a photodiode that approaches a photo-counting regime. NEP , the minimum optical power detectable by a photodetector, is typically defined as the ratio of the input optical power required to produce a signal-to-noise ratio (SNR) of one in a measurement bandwidth. NEP can be expressed by

$$NEP = \frac{I_{dark,rms}}{\Re} \quad (23)$$

The unit of NEP is W.

The bandwidth-normalized (NEP_B) value is generally used when a photodetector is operating in a high-frequency region, where the noise is independent of frequency and white noise dominates the noise level. NEP_B can be expressed as Equation (24) and the unit is in $W/Hz^{1/2}$.

$$NEP_B = \frac{I_{dark,rms}}{\Re\sqrt{B}} \quad (24)$$

NEP is usually inferred by the corresponding optical power as extrapolating the photocurrent into the noise current in the photocurrent vs. the optical power plot, shown in Figure 2.12 Optical power-dependent photocurrent plot showing nonlinearity at low-light level illumination. This approach is based on the assumption that \Re is invariantly

illuminated at a wide range of optical power to NEP . This assumption, however, is often not correct because of the presence of traps resulting from the disorderly structure of OPDs, leading to nonlinear behavior and extrapolation errors. Therefore, acquiring an actual NEP calls for a direct measurement of the photocurrent in which the SNR equals one.

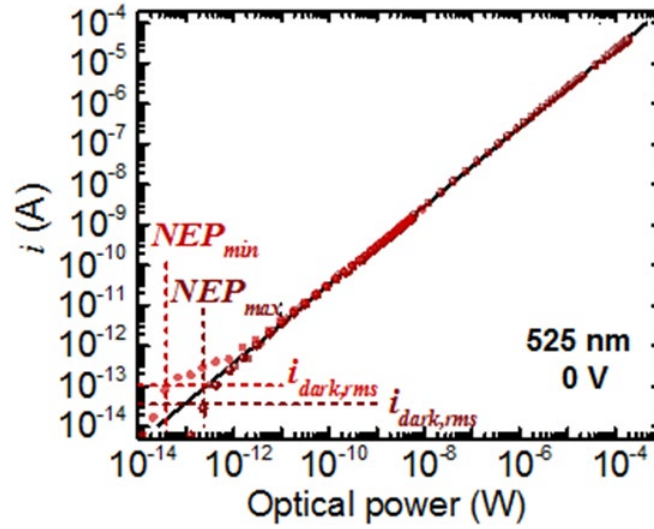


Figure 2.12 Optical power-dependent photocurrent plot showing nonlinearity at low-light level illumination.

D^* is inversely proportional to NEP . The noise scales up with an increased device area or measurement bandwidth. As a result, the specific detectivity, D^* is a common expression used for evaluating a photodetector, described by

$$D^* = \frac{\sqrt{AB}}{NEP} \quad (25)$$

where A is the photoactive area in cm^2 , B is the measurement bandwidth in Hz, and the unit of D^* is in $\text{cm-Hz}^{1/2} \text{W}^{-1}$, or in Jones.

CHAPTER 3. EXPERIMENTAL METHODS

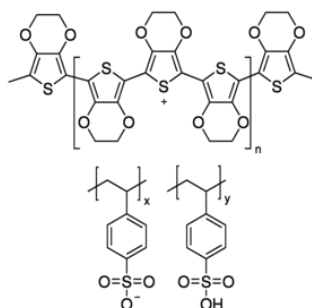
In this chapter, experimental methodology of OPDs will be discussed, including organic materials used this research, details of fabrication processes, and an overview of fabrication techniques. In addition, the methods of optical and electrical characterization will be provided in the end.

3.1 Materials

Indium-doped tin oxide (ITO) (Colorado Concept Coatings), poly(3,4-ethylenedioxythiophene):polystyrene sulfonate (PEDOT:PSS) (HERAEUS) layers, or transparent silver layers were used as bottom electrodes. For electron collection, an amine-containing polymer, polyethylenimine ethoxylated (PEIE) (Sigma Aldrich) diluted in 2-methoxyethanol (Sigma Aldrich) were used for work function reducing interlayer for bottom electrodes. The photoactive layers were composed of donor/acceptor blends. The donors were either poly(3-hexylthiophene-2,5-diyl) (P3HT) (Rieke Metals) or Poly(diketopyrrolopyrrole-terthiophene) (PDPP3T) (Solarmer Materials). Small molecule fullerene derivatives were used as acceptors, *i.e.*, indene C60-bisadduct (ICBA) (Nano-C), [6,6]-Phenyl C61 butyric acid methyl ester (PC₆₁BM or PCBM) (Nano-C), or [6,6]-Phenyl C71 butyric acid methyl ester (PC₇₁BM) (Solenne). Three combinations of donor and acceptor blends in photoactive layers were used. P3HT:ICBA and P3HT:PCBM are for the visible range sensing, whereas PDPP3T:PC₇₁BM enables the photoresponse into the near

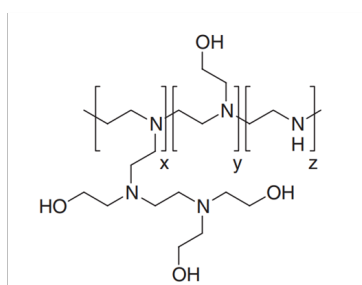
infrared (NIR) region. The solvent used to dissolve the mixture of donors and acceptors was chloroform (CF) (Sigma Aldrich) and 1,2-dichlorobenzene (DCB) (Sigma Aldrich). For hole-collection use, either a thermally evaporated layer of MoO₃ or an electrically p-doping technique using phosphomolybdic acid (PMA) (Alfa Aesar) mixed in acetonitrile was adopted. Some of the devices were superficially treated on photoactive layers with atomic layer deposition (ALD) processed at 110 °C, which will be discussed in the following section. The top electrodes for electrical contact were thermally evaporated Ag layers. The chemical structure of these materials is shown in Figure 3.1.

Transparent conducting material:

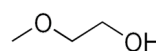


**poly(3,4-ethylenedioxythiophene):polystyrene sulfonate
(PEDOT:PSS)**

Work function reducing modifier:

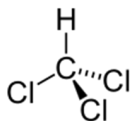


**Polyethylenimine ethoxylated
(PEIE)**

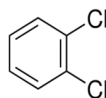


2-Methoxyethanol

Solvents for photoactive layers:

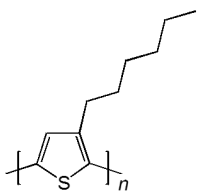


Chloroform

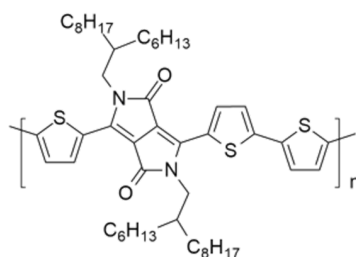


1,2-Dichlorobenzene

Donors:

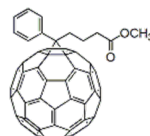


**poly(3-hexylthiophene-2,5-diyl)
(P3HT)**



**Poly(diketopyrrolopyrrole-terthiophene)
(PDPP3T)**

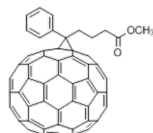
Acceptors:



**[6,6]-Phenyl C₆₁ butyric acid methyl ester
(PC₆₁BM)**



**Indene C₆₀-bisadduct
(ICBA)**



**[6,6]-Phenyl C₇₁ butyric acid methyl ester
(PC₇₁BM)**

P-doping:

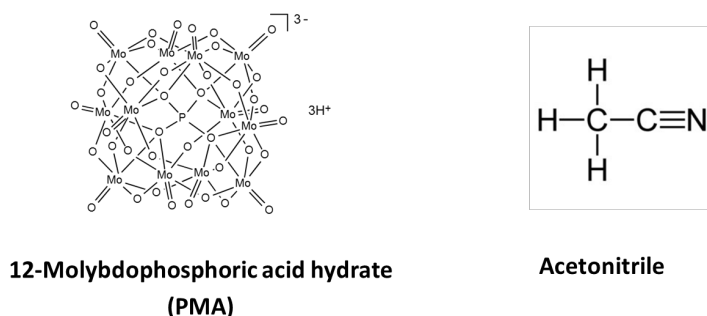


Figure 3.1 Chemical structure of materials used in OPDs.

3.2 Fabrication Procedures

3.2.1 Substrate Preparation

First, polished soda lime float glasses coated with ITO with sheet resistance 9-15 Ω/\square into 1'' by 5'' strips were cut. Then these strips were adhered with half of inch Kapton tape as a shadow mask for patterning. The ITO substrates were patterned with wet etching in a solution of HCl:HNO₃ v/v for 8 minutes at a bath temperature of 60 °C. After etching, the patterned ITO strips were rinsed with copious amounts of distilled water and then cut into 1'' by 1'' pieces. Afterwards, the substrates were cleaned in sequential ultrasonic baths of detergent, deionized water, acetone, and 2-propanol for 30 min each at 60 °C.

For the flexible devices, polyestersulfone (PES) was used as substrates. An 11 nm-thick MoO₃ layer and 10 nm-thick transparent Ag were thermally deposited sequentially. The MoO₃ layer is to generate a thin film of nanoporosity and facilitate transparent silver

growth onto without generating isolated islands. The device area and design pattern were defined by a shadow mask.

3.2.2 *Electron-Collection Interlayer Deposition*

PEIE, 80% ethoxylated solution (Sigma-Aldrich, 37 wt.% in H₂O, Mw. ca. 110,000), was used to lower the work function of bottom electrodes by forming an efficient electron-collecting layer. PEIE was diluted in 2-methoxyethanol to a concentration of 0.4 wt.%, and it was magnetically stirred at 500 rpm overnight. PEIE solution was dispensed onto the substrates through 0.2 μ m pore size polytetrafluoroethylene filters and then spun coated at 5000 rpm for 30 s, followed by thermal annealing on a hot plate at 100 °C for 10 min.

3.2.3 *Photoactive Layer Deposition*

A solution of highly regioregular P3HT and ICBA (or P3HT and PCBM) in 1:1 weight ratio was mixed in 1,2-dichlorobenzene with a concentration of 40 or 100 mg/mL, which was magnetically stirred overnight at 500 rpm at 70 °C in a nitrogen-filled glovebox. A P3HT:ICBA (or P3HT:PCBM) solution was spun on top of PEIE-coated substrates at 800 rpm for 30 s through 0.2 μ m PTFE filters. Photoactive layers were slowly dried in covered glass Petri dishes for solvent annealing, followed by thermally annealing at 150 °C for 10 min on a hot plate in a nitrogen-filled glovebox. This step facilitated the remaining solvent removal and P3HT crystallization. After annealing processes, a portion

of photoactive films was wiped off with chlorobenzene. Thus, the underlying bottom electrode was exposed that allowed electrical contact.

In another case, a solution of PDPP3T and PC₇₁BM in 1:2 weight ratio was mixed in 1,2-dichlorobenzene and chloroform with a volume ratio with a concentration of 15 mg/mL. The solution was magnetically stirred at least for 3 h at 500 rpm at 70 °C in a nitrogen-filled glovebox. The hot solution at 70 °C was spun on top of PEIE-coated substrates at 1,500 rpm 10,000 rpm/s for 60 s through 0.2 µm PTFT filters. Photoactive layers were slowly dried in covered glass Petri dishes for solvent annealing for 5 h. No thermal annealing was required.

3.2.4 Hole-Collection Layer Deposition

For a hole-collection purpose, either a 10 nm thick MoO₃ layer or an electrical p-doping technique was used. The fabrication process of electrically p-doped polymer films will be described in the next section. After the doping process, a silver layer deposited by thermal evaporation for 150 nm was used as top electrodes. In another case, MoO₃ and Ag layers were deposited sequentially by vacuum thermal evaporation (Kurt J. Lesker SPECTROS) with a working pressure less than 10⁻⁶ Torr through a patterned shadow mask.

3.2.5 Device Structure

If without further addressed, the reference devices were fabricated based on inverted structure, the cross section is shown in Figure 3.2. The incident light illuminated from the bottom side.

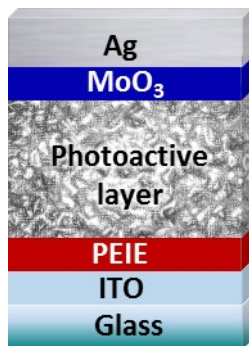


Figure 3.2 Cross section of the reference device.

We fabricated five individual devices on a 1" x 1" substrate, defined by the overlap of bottom and top electrodes with five fingers. The top view of the reference devices indicates the effective device area, where the top and bottom electrodes are overlapped, are shown in Figure 3.3. The shaded areas depict the device areas, ca. 0.12 cm² for each.

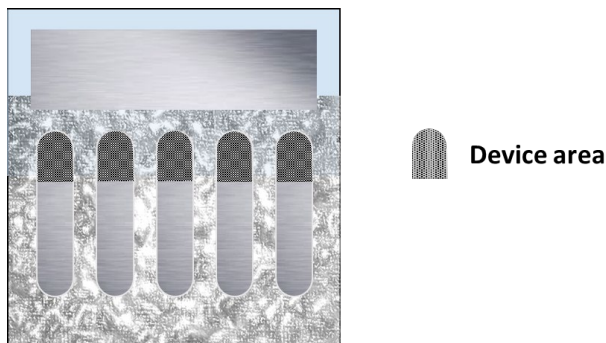


Figure 3.3 Top view of reference devices.

3.3 Electrical p-Doping

A PMA solution with a concentration of 0.5 M in acetonitrile were prepared by mixing it with a magnetic stirring bar in a transparent vial. Samples with P3HT:ICBA films were immersed into a PMA solution in a Petri dish for 1 min. To remove the residues of PMA on the substrates, the doped films were rinsed with 1 mL of pure acetonitrile and spun at 2,000 rpm for 30 s to dry out.



Figure 3.4 Picture of PMA doping for a polymer film.

3.4 Atomic Layer Deposition

The atomic layer deposition (ALD) system used in this research is a Savannah S200 ALD, from Cambridge NanoTech Inc. ALD is a deposition technique generates high-quality and defect-free thin films with excellent step coverage (73). A sequential use of gas phase chemical process leads to the ALD thin-film growth. The chemical species, typically called precursors, are alternatively reacts with the surface of materials cyclically. Generally one growth cycle consists of four steps: 1) Exposure of the first precursor, 2) purging of

the reaction chamber, 3) exposure of the second precursor, and 4) a further purging of the reaction chamber.

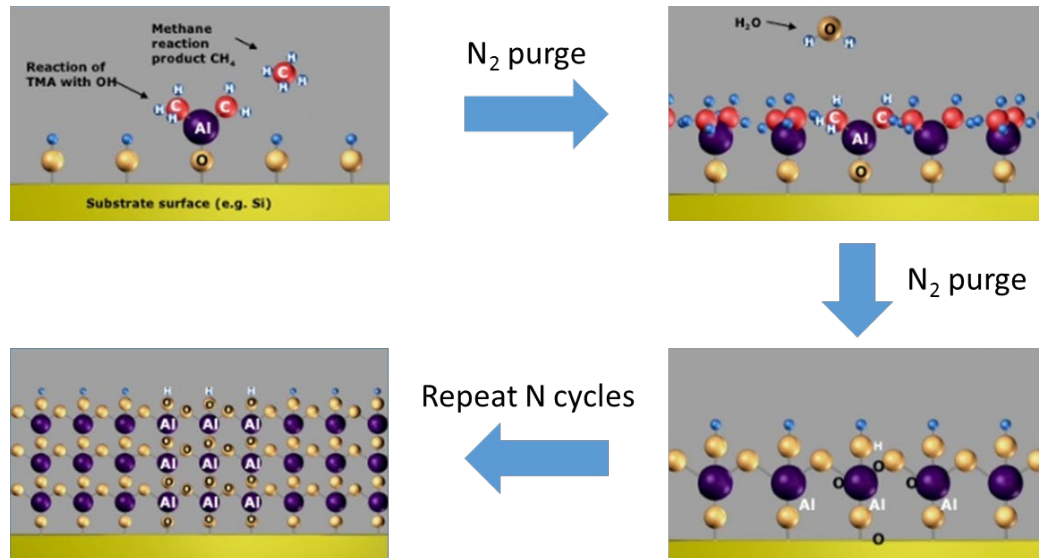


Figure 3.5 The procedure of Al_2O_3 layer deposition using ALD. (Cambridge NanoTech Inc.)

The growth cycles are repeated as many times as required for the desired film thickness. Depending on the process and the reactor being used, one cycle can typically take time from a few seconds to tens of seconds, and may deposit between 0.1 and 3 Å of film material, depending on the material underneath. Figure 3.5 shows an example of the Al_2O_3 thin-film deposition using ALD. Before the ALD processes, the Si surface absorbs water vapor forming hydroxyl groups in the air. The alternative exposure of two precursors, trimethylaluminum (TMA) and water (H_2O). First, TMA vapor species only react with hydroxyl groups and do not react with themselves, leading to a uniform and self-limiting surface. Then the excess TMA species are pumped away with methane-reaction product.

Next, H₂O vapor is pulsed into the chamber and reacts with the dangling methyl groups, forming aluminum-oxygen (Al-O) bridges and hydroxyl groups on the surface. The reaction product methane and excess H₂O vapor are carried away. Similarly, excess H₂O does not react with hydroxyl groups, leading to an atomic passivated layer. This completes one cycle of a monolayer of Al₂O₃.

3.5 Characterization

3.5.1 Current-Voltage Measurements

Current density-voltage (J - V) characteristics of the devices were measured in an N₂-filled glovebox at room temperature with an electrometer (Keithley Model 6430) controlled by a LabVIEW program. The current values were recorded until they were stabilized at a given DC voltage. For dark current measurements, the sample was placed in a dark condition provided by blackout materials that are designed to prevent stray or ambient light. Illumination source was provided by a LED controlled by a DC power supply (Agilent E3647A) and coupled with an optical band-pass filter. The optical power was measured by a power meter (OPHIR, PD300R-UV-SH-ROHS).

3.5.2 Irradiance- and Temperature-Dependent Current-Voltage Measurements

J - V characteristics of the devices were measured in an N₂-filled glovebox with an electrometer (Keithley Model 6430). A green LED (Super Bright LEDs, Inc., LD1-G)

coupled with a 525 nm band-pass filter with a FWHM of 10 nm was used as a light source. The optical power was modulated by a DC power supply, ranging from nW to mW. When the green LED was used, the optical power was varied by changing the LED's bias voltage and by placing neutral density filters to operate the LED within its linear region but still allowing low optical power to be delivered to OPDs. OPDs were mounted on a copper sample holder and placed on a thermal-controlled stage. To have better thermal conductivity, thermal grease was applied between the sample holder and the thermal stage. The temperature ranged from 283 K to 353 K.

3.5.3 Spectral Responsivity Measurements

A laser-driven light source (Energetiq) with a continuous wave coupled with a monochromator (Spectral Products CM110) was used as a light source for spectral responsivity measurement. The light source was collimated using optical lens and illuminated onto the photodetectors active area. Optical band-pass filters were placed in the beam path to avoid multiple frequency harmonic. The optical power on the devices was calibrated by a Si photodiode (Hamamatsu S2386-44K) and a power meter (OPHIR, PD300R-UV-SH-ROHS). An electrometer (Keithley Model 6517A) was used to measure the currents under illumination at an applied voltage. A custom-written LabVIEW program controlled the monochromator to vary the wavelength and recorded the optical power and photocurrent values. The responsivity values were obtained from the photogenerated current values measured at each wavelength divided by the optical power.

3.5.4 Linear Dynamic Range Measurements

Linear dynamic range was obtained by the measurement of photogenerated currents provided by a wide range of the optical power. Either a green LED (Super Bright LEDs, Inc., LD1-G) coupled with a 525 nm band-pass filter with a FWHM of 10 nm or a 653 nm laser was used as a light source. The optical power was modulated by a DC power supply and measured with an optical meter. The photogenerated current values at each optical power were measured in an N₂-filled glovebox with an electrometer (Keithley Model 6430) controlled by a custom-written LabVIEW program.

3.5.5 Response Time

To measure response time, a 635 nm LED (Super Bright LEDs, Inc., LD1-R) was modulated in square waves by a function generator and illuminated an OPD device, which was connected a load resistor in series. The profile of transient voltage drop across the resistor was captured by an oscilloscope (Rohde&Schwarz RTO 1002) and determined the response time. A pre-amplifier (Stanford Research Systems SR560) is required when the signal to ratio is low, *i.e.*, under low illumination. Figure 3.6 shows the measurement setup.

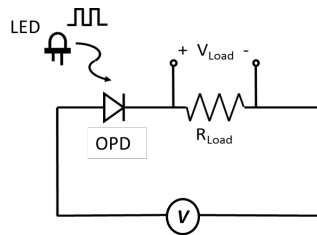


Figure 3.6 The setup schematic of response time measurement.

CHAPTER 4. ORIGINS OF THE DARK CURRENT

4.1 Introduction

The magnitude of electronic noise in the dark condition determines the detectability of a photodetector and is quantified by the root-mean-square (rms) value of the current fluctuations, referred to $I_{dark,rms}$. OPDs show high potential to deliver innovations for next generation, but the state-of-the-art dark current density (J_{dark}) in OPDs is several orders of magnitude higher than that of silicon low-noise photodiodes, which hinders the abilities to establish low-power organic sensing platforms.

The current strategies for increase R_p have been studied for years, but the reverse saturation current (J_0) associated with generation/recombination of carries also plays a central role in determining the J_{dark} . To investigate the limitation of the dark current level, in this chapter, we will discuss the inherent physical properties of two independent systems by conducting irradiance- and temperature-dependent studies and by using the equivalent circuit model to approach J_0 . Here, we incorporated poly(3-hexylthiophene-2,5-diyl) (P3HT) as a donor and either indene-C₆₀ bisadduct (ICBA) or [6,6]-Phenyl-C₆₁-butyric acid methyl ester (PC₆₁BM or PCBM) as an acceptor in BHJ. Both of the devices with thick active layer, ca. 500 and 750 nm, were fabricated with identical methods.

4.2 Establish an OPD with Low Dark Current

Figure 4.1(a) shows that the J_{dark} values in the P3HT:PCBM OPD is significantly smaller than previously reported (16, 61). The low J_{dark} values are obtained by means of introduction of a thick photoactive layer that mitigates parasitic effects (32) and PEIE modified ITO as an electron-collecting layer. PEIE is an insulating polymer-containing simple aliphatic amines that reduces the work function of an electrode and electrically n -dopes the fullerene acceptors at this interface (74). These combined effects led to OPVs with small J_{dark} values (75) and more recently has been demonstrated to reduce J_{dark} in OPDs (52, 58)

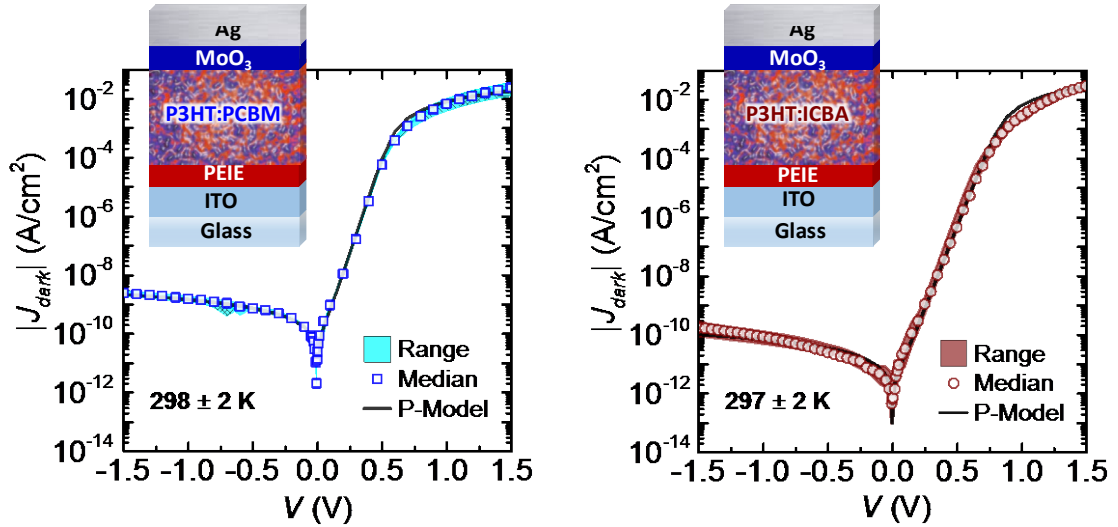


Figure 4.1 The dark J - V characteristics of (a) P3HT:PCBM- and (b) P3HT:ICBA-based OPDs measured at room temperature.

Compared to P3HT:PCBM OPDs with 750 nm-thick photoactive layers, P3HT:ICBA devices with 500 nm-thick photoactive layers yield lower J_{dark} values in reverse bias by more than one order of magnitude, which are comparable to those of low-noise Si PDs (Hamamatsu S1133), shown in Figure 4.1 (b). In addition, the devices in both conditions enable high reproducibility, and the shaded areas in Figure 4.1 present the minimum to maximum variations in J_{dark} measured on 8 devices fabricated in two batches.

4.3 Irradiance- and Temperature-Dependent Studies

Next, we performed temperature- and irradiance-dependent measurements to analyze $J_{dark}(V, T)$ and $V_{oc}(J_{sc}, T)$, and Prince's approach (76) was used based on a single-diode equivalent circuit model (77, 78) that accounts for the parasitic effects of R_p and series resistance R_s . From now on, we refer to this model as the P model. In the P model, the steady-state current density is given by Equation (13).

$$J = \frac{1}{1 + R_s/R_p} \left\{ J_0 \left[\exp \left(\frac{V - J R_s A}{\frac{n k T}{q}} \right) - 1 \right] - \left(J_{ph} - \frac{V}{R_p A} \right) \right\} \quad (13)$$

where k is the Boltzmann constant, n is the ideality factor, and J_{ph} is the photogenerated current. By fitting with Equation (14), J_0 , $R_p A$, and n values in a function of temperature were extracted. High reproducibility of J_{dark} allows a reliable irradiance-dependent measurement with optical power varying over 9 orders of magnitude, which is a huge difference from previous studies carried out on OPVs, illuminated only at high optical power or irradiance (e.g., from 1 to 100 mW/cm²). Figure 4.2 illustrates J_{sc} - V_{oc}

characteristics of P3HT:PCBM-based and P3HT:ICBA-based OPDs measured at temperatures varying from 8 to 80 °C and optical power varying over 9 orders of magnitude, illustrated in Figure 4.2.

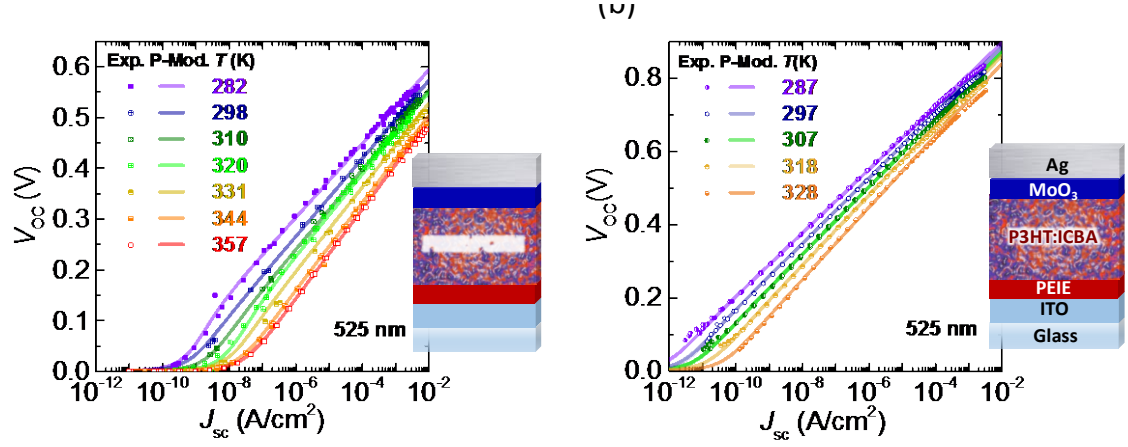


Figure 4.2 Measured and modeled open-circuit voltage vs. short-circuit current density characteristics over various temperatures of (a) P3HT:PCBM-based and (b) P3HT:ICBA-based OPDs.

J_0 refers to an equilibrium current density that is proportional to the recombination rate (R_{eq}) associated with in thermally-activated processes, such as band-to-band, trap-assisted, or Auger recombination. $J_0 \propto R_{eq} \propto e^{-E_g/nkT}$. E_g is the transport bandgap of the system related to the strength of electronic coupling between donor and acceptor moieties, and n represents the dominant recombination process. V_{OC} as a function of J_{ph} can be described in Equation (14). When the optical power is sufficiently small, the R_s can be negligible and J_{SC} is approximated to J_{ph} .

$$V_{OC} = \frac{nkT}{q} \ln \left[1 + \frac{J_{ph}}{J_0} \left(1 - \frac{V_{OC}}{J_{ph} R_p A} \right) \right] \quad (14)$$

We simultaneously fitted $J_{dark}(V, T)$ and $V_{OC}(J_{SC}, T)$ using Equation (13) and (14), and J_0 , $R_p A$, and n values associated with different temperatures were extracted. From Figure 4.1 we find highly agreement in experimental and modeled data based on the fitting parameters. Furthermore, the use of Shockley equivalent circuit model allows the identification of the J_0 as a thermally activated process (79):

$$J_0(T) = J_{00} \exp \left(\frac{-E_g}{nkT} \right) \quad (26)$$

where J_{00} is a constant pre-factor. In Figure 4.3, J_0 follows Arrhenius behavior and the solid lines present a fit to Equation (26).

P3HT:PCBM shows a transport bandgap of 1.13 ± 0.04 eV, and P3HT:ICBA shows a transport bandgap of 1.31 ± 0.05 eV. The results suggest that P3HT:ICBA showing higher E_g allows weak electronic interactions between donor and acceptor moieties in the bulk heterojunction, leading to a reduced dark current density. The pre-factor of P3HT:PCBM and P3HT:ICBA is 2×10^4 and 650 A/cm^2 , respectively. We believe that the pre-factor is dependent on the morphology of materials.

In summary, an important lesson of this experiment is that V_{OC} - J_{SC} relation provides a general framework that selects the proper combination of materials comprising BHJ photoactive layers in OPDs. Larger E_g leads to lower J_0 , which limits the dark current

value. Therefore, in the following context, we will mainly focus on P3HT: ICBA-based OPDs and investigate their device properties.

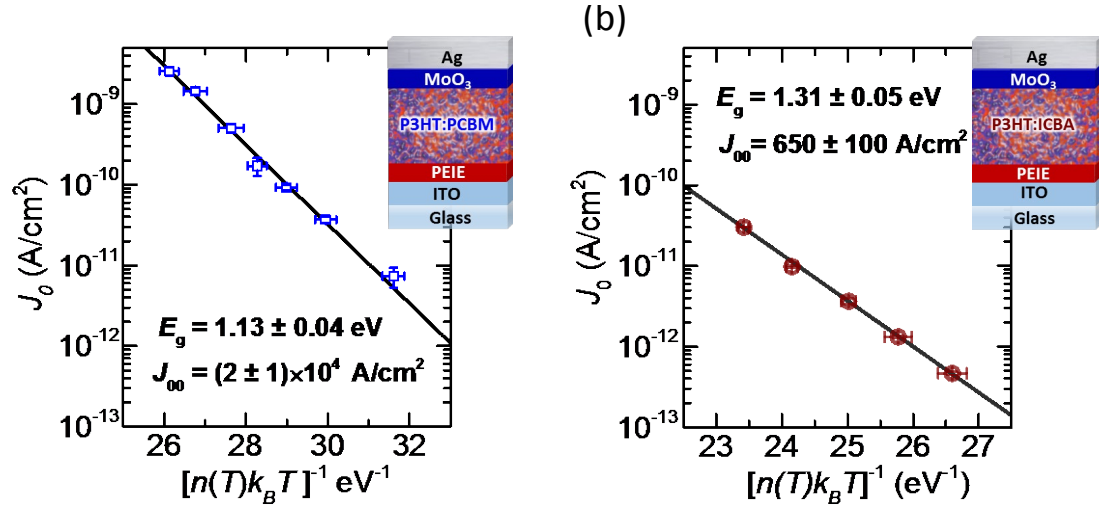


Figure 4.3 Transport bandgap extraction from the reverse saturation current density vs. inverse of the product between thermal energy and ideality factor.

4.4 A Comparison with Si PDs

To evaluate P3HT:ICBA-based OPDs in a reasonable way, we show a side-by-side comparison of the photodetector metrics with a low-noise Si PD (Hamamatsu S1133). A comparison of current densities measured under dark conditions in the Si PD with an area of 0.07 cm^2 and P3HT:ICBA OPDs with an area of 0.10 cm^2 is shown in Figure 4.4. Our OPDs present dark current density values are smaller than 10^{-10} A/cm^2 in reverse bias, comparable to those of state-of-the-art low-noise Si PDs (*e.g.*, Hamamatsu S1133).

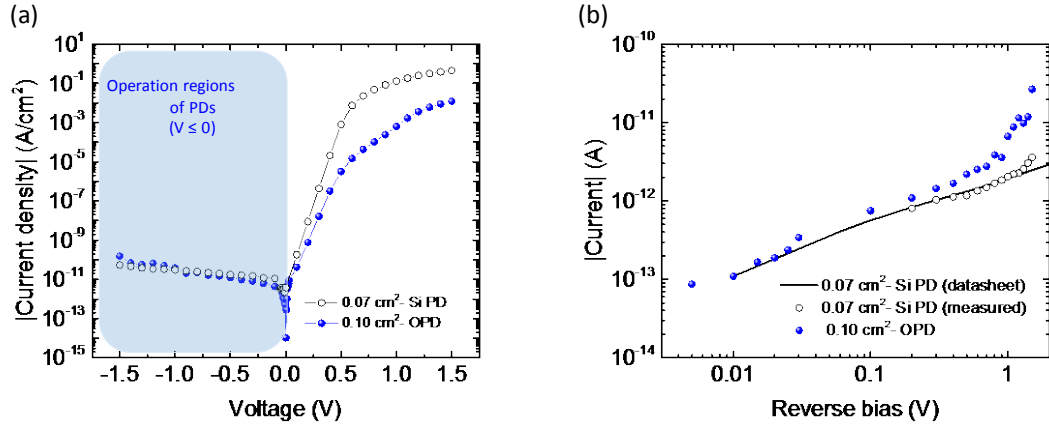


Figure 4.4 A comparison of (a) measured J - V characteristics, (b) measured I - V characteristics in the reverse in the dark for P3HT:ICBA OPDs and Si PDs.

Next, a comparison of spectral responsivity in P3HT:ICBA OPDs and in Si PDs is demonstrated in Figure 4.5. The OPDs show a peak responsivity value of 0.29 A/W at 610 nm , comparable to that of their Si counterparts. Furthermore, the responsivity values in OPDs are consistent as applied at 0 V and -1.5 V , which can be considered electrical field independent.

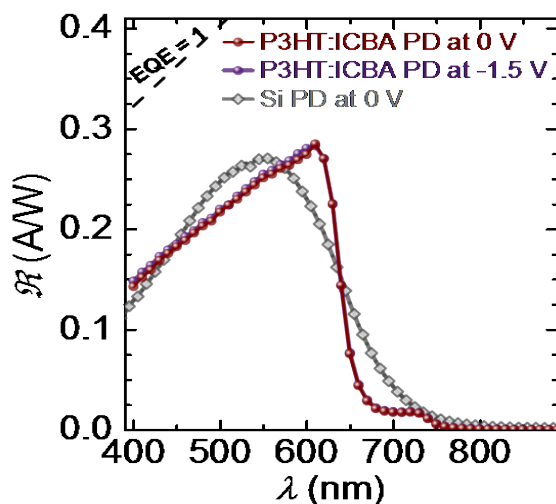


Figure 4.5 A comparison of spectral responsivity measured in P3HT:ICBA OPDs and Si PDs.

Next, to assess the response time of P3HT:ICBA OPDs, we connected an OPD and a load resistor in series without applying external voltage ($V=0$ V) and captured the transient photocurrents by measuring the voltage drop across the resistor. The OPD generated photocurrent by illuminated with a LED at 525 nm, which is frequency modulated in square waves by a function generator. Figure 2.10 illustrates the measurement setup. The response time was determined by the rise time of the photocurrent with the load resistance varying from $50\ \Omega$ to $10\ \text{k}\Omega$. Here, we found that the response time of the OPDs is limited at $35.2 \pm 2.9\ \mu\text{s}$ when using a $50\ \Omega$ resistor, while the response time becomes significantly larger when connecting with a $10\ \text{k}\Omega$ resistor. Figure 4.6 exhibits the measured response times corresponding to varying resistance and compare to those of Si PDs measured at 0 V. Here, OPDs exhibit slower dynamic, primarily due to smaller carrier mobility in disordered organic semiconductor films. Figure 4.7 demonstrates that the

P3HT:ICBA OPDs yields a 3dB-bandwidth of 15 kHz measured at both 0 V and -3 V, suggesting the bandwidth is independent of the electrical field.

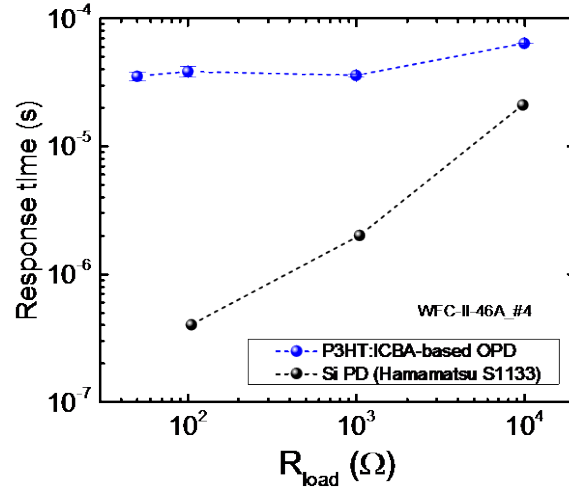


Figure 4.6 The response times in OPDs measured with varying load resistance compared to those in Si PDs.

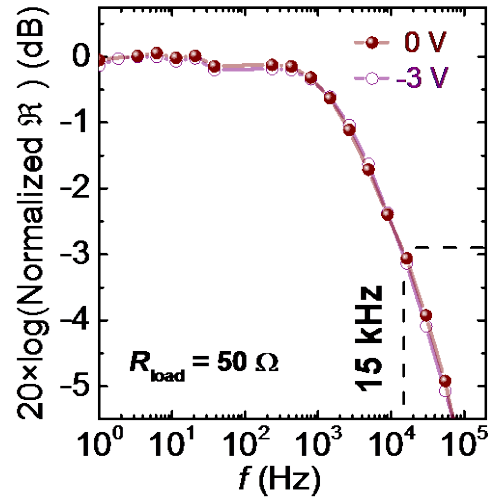


Figure 4.7 Frequency response in OPDs.

Figure 4.8 (a) shows the normalized transient current of OPDs applied at various voltages, from 0 to -16 V. The results consistently show the photocurrent independent of the electrical field, and the transient profile exhibits a fast-rising time, followed by a slower component. Figure 4.8 (b) confirms that the OPDs are sustainable after applied an electrical field of 40 V/ μm .

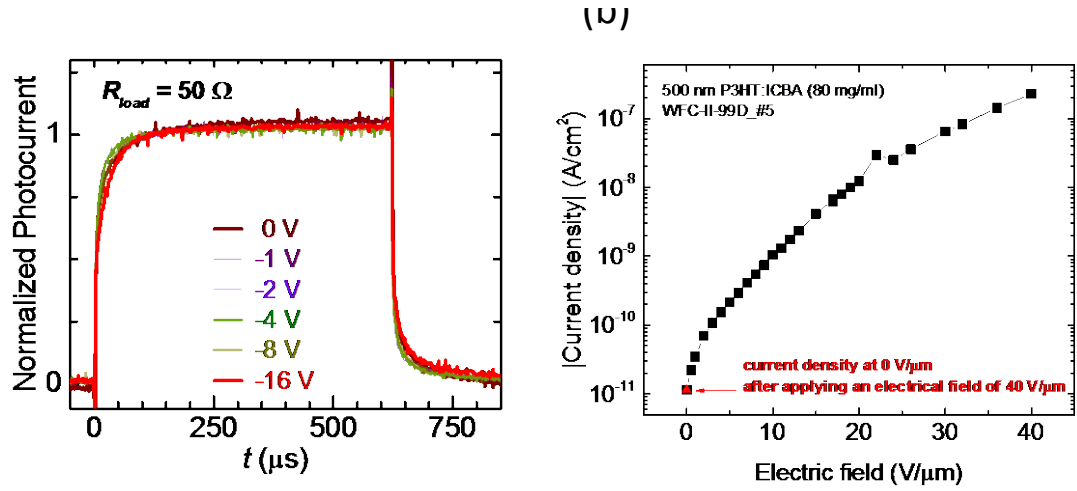


Figure 4.8 (a) Normalized transient photocurrent of OPDs at various applied bias. (b) Photocurrent vs. electrical field.

Next, we further examined the electronic noise in P3HT:ICBA OPDs and Si PDs. From the temporal evolution of the dark current measured at 0 V with a measurement bandwidth of 80 Hz, the noise in OPDs and Si PDs is 26 and 25 fA, respectively, shown in Figure 4.9.

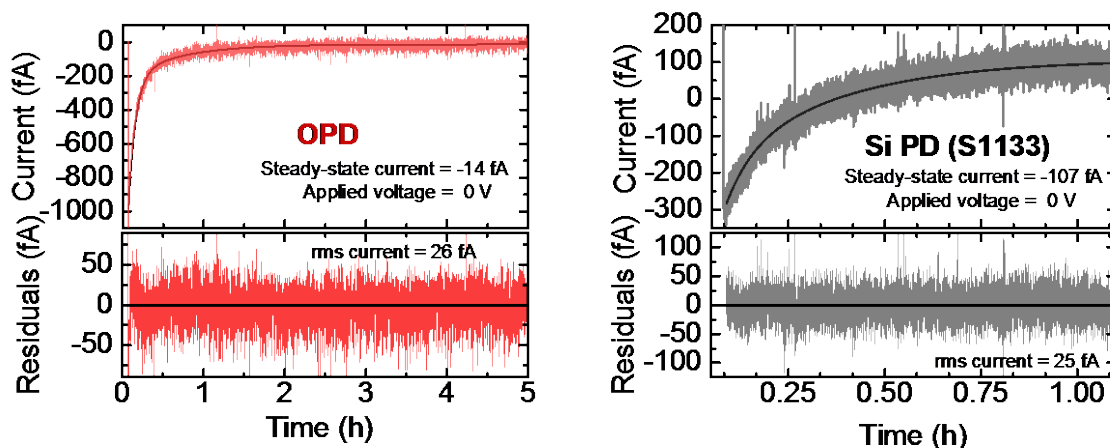


Figure 4.9 Temporal evolution of the dark current measured at 0 V in (a) a P3HT:ICBA OPD, and (b) a Si PD (Hamamatsu S1133).

From above results, a extrapolated NEP measured at 525 nm and 80 Hz can be derived by $I_{dark,rms}/R = 90$ fW. However, in general cases, the disordered structure in organic materials leads to the presence of traps. Therefore, a nonlinear NEP behavior is usually shown in OPDs. Here, we performed a direct measurement of photocurrent as a function of optical power, shown in Figure 4.10. In Figure 4.10, the LDR is 84 dB. In addition, we found that R values are variant at low optical power in the range of pW; Charge-trapping processes lead to a reduced R , whereas trap-assisted photoconductive gain

leads to an improved R . As shown in Figure 4.11, a direct measurement of NEP at 525 nm and 80 Hz reveals that the charge-trapping NEP (NEP_t) and photoconductive NEP (NEP_g) is 240 fW and 45 fW, respectively. Next, assumed the trapping behavior is observed in other wavelengths, we can predict the spectral D^* based on the spectral R values, leading to a peak D_t^* (610 nm, 80Hz) of 1.6×10^{13} Jones and a D_g^* (610 nm, 80Hz) of 8.3×10^{13} Jones, associated with charge-trapping and photoconductive processes, respectively. The spectral D^* of P3HT:ICBA OPDs and a comparison of that with Si PDs are shown in Figure 4.12.

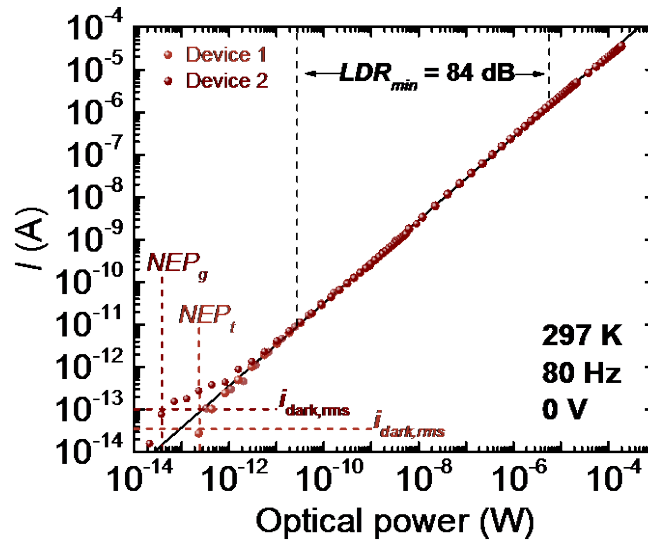


Figure 4.10 The current vs. the optical power characteristics in P3HT:ICBA OPDs.

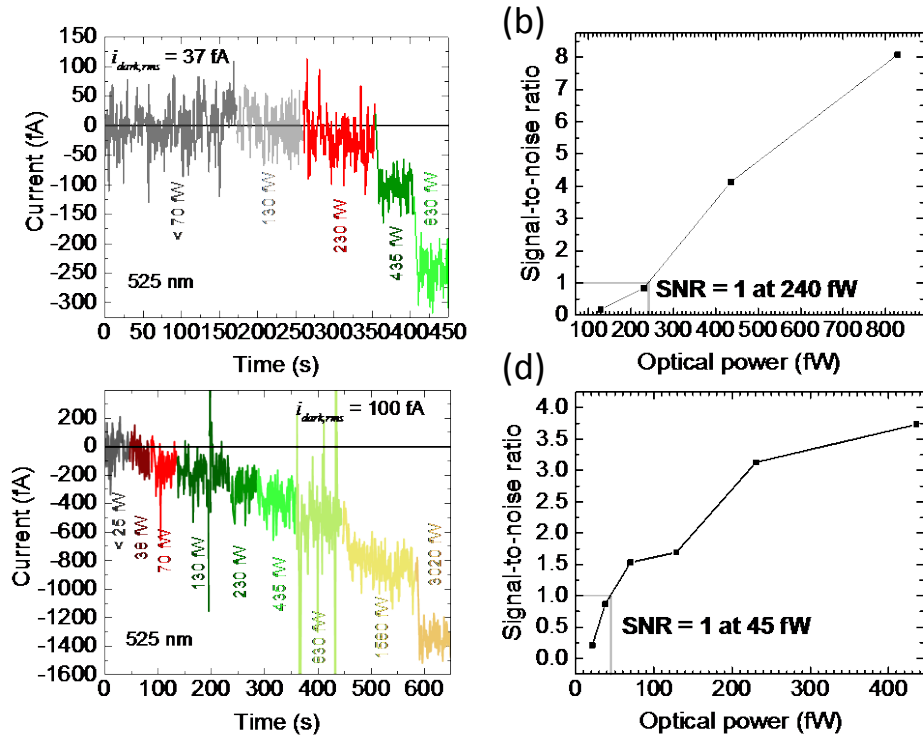


Figure 4.11 Current transients in P3HT:ICBA OPDs showing (a) NEP_t and (b) linear interpolation of SNR equal to 1, and (c) NEP_g and (d) linear interpolation of SNR equal to 1.

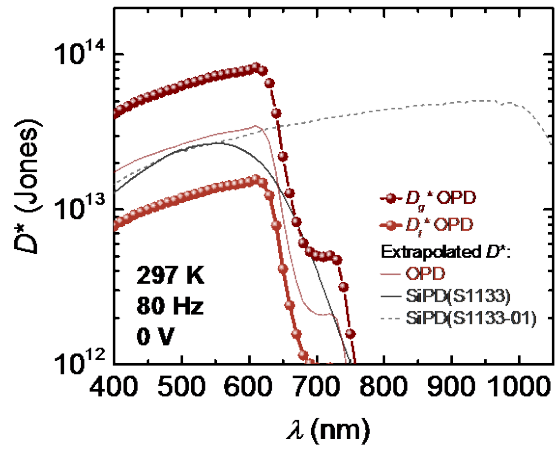


Figure 4.12 The spectral specific detectivity of P3HT:ICBA OPDs and Si PDs.

4.5 Summary

In this chapter, we discussed the origin of the dark current, which determines the electronic noise in OPDs. By conducting irradiance- and temperature-dependent studies with the use of the Prince equivalent circuit model, we extracted the reverse saturation current density and the shunt resistance in OPDs that determined the shot noise and thermal noise, respectively. In addition, we discussed that the reverse saturation current density is associated with thermally-activate processes in the D/A, and this insight provided us with a proper selection of materials to achieve high-detectivity OPDs. We demonstrated P3HT:ICBA OPDs yield a measured NEP of 40 fW and a peak D^* 8×10^{13} Jones, which is comparable to that of low-noise Si PDs.

CHAPTER 5. LARGE-AREA AND FLEXIBLE ORGANIC PHOTODIODES

5.1 Introduction

Area-scaling properties and high form factor are the features for developing OPDs that rival inorganic technology. In inorganic photodiodes, it is common that the dark current density values grow rapidly as the photoactive areas are scaled up. For instance, a state-of-the-art low-noise Si PD (Hamamatsu S1133) with an area of 0.07 cm^2 shows dark current density values of 30 pA/cm^2 at -1 V , while a state-of-the-art Si-PD with an area of 0.90 cm^2 (Hamamatsu S12497) exhibits a dark current density of 220 pA/cm^2 at -10 mV . Thus, high restrictions in manufacturing control of crystal defects for Si is required to obtain a high D^* over increasingly large areas (80), which imposes a tradeoff between performance, area, number of devices, and cost in the design of applications. In addition, the state-of-the-art photodetectors based on crystalline inorganic semiconductors processed at high temperatures introduce challenges for developing flexible and low-power devices at low cost.

Interest in developing flexible and stretchable optoelectronics is blooming (14, 41-47). In particular, flexible photodetectors provide mechanical conformability (39-42) that enables improved signal qualities and therefore lowers power consumption. With recent advances in the field of organic materials, OPDs show higher mechanical compatibility for developing flexible photodetectors and reliable physiological sensors. Several solution-processed techniques have been adopted for the realization of flexible OPDs, such as spin

coating, inkjet printing, blade coating. The dark current values of state-of-the-art flexible OPDs are comparable to those of conventional α -Si p-i-n photodiodes on flexible substrates, in the range of sub-nA/cm^2 (49, 52, 60, 81-83). The existing paradigm held in the flexible OPDs reported in the literature are (i) higher dark current density values than their rigid crystalline inorganic counterparts; (ii) the photoactive area of high-performance OPDs limited near 0.1 cm^2 .

In this chapter, we will evaluate the performance of large-area OPDs on rigid ITO/glass substrates and then show these OPDs on flexible substrates with unprecedented low dark current density (10^{-12} A/cm^2) that leads to high detectivity values in the visible spectrum. Next, we will demonstrate large-area flexible OPDs in 1.0 cm^2 , which shows the dark current density values comparable to those of commercial low-noise Si PDs of similar size. We further take advantages of these combined properties and design the OPDs in ring geometry for efficient physiological signal collection.

5.2 Area Scaling

To investigate the scalability of OPDs, we fabricated devices on glasses with five different areas varying from 0.1 , 0.2 , 0.4 , 0.6 , and up to 0.9 cm^2 . Figure 5.1 illustrates J - V characteristics of OPDs with various device areas measured in the dark condition. The data reveal that there are no substantial differences under forward bias conditions, suggesting that the parasitic effects due to the series resistance are negligibly small when the area increases to 0.9 cm^2 . We found that 0.9 cm^2 -OPDs exhibit higher dark current densities comparing to smaller devices. However, 0.9 cm^2 -OPDs still show low dark current density

values near 0 V. Compared the dark current value biased at -10 mV in OPDs and a standard Si PD (Hamamatsu S12497) with the same device area of 0.9 cm^2 , J_{dark} is 55 times lower than that of the Si PD. Table 1 summarizes the dark current density values at -10 mV of OPDs with different areas. Here, we show the OPD scalability up to 0.9 cm^2 associated with dark current values.

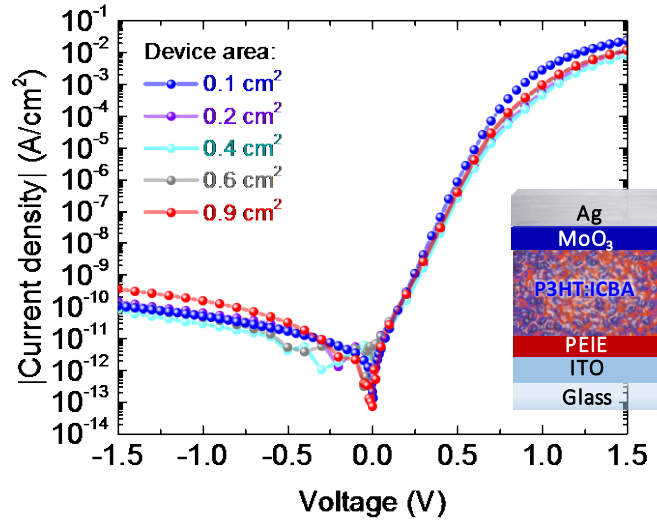


Figure 5.1 J - V characteristics of OPDs with various device areas measured in the dark condition.

Table 1 The dark current density values at -10 mV of OPDs with different areas, ranging from 0.1 to 0.9 cm^2 .

Photoactive Area (cm^2)	Dark current density @ -10 mV (pA/cm^2)
0.1	0.6
0.2	4.1
0.4	2.8
0.6	5.5
0.9	0.1

5.2.1 Area Scaling

(i) PEDOT:PSS as bottom electrodes

In addition to area-scaled OPDs fabricated on glass, we conducted studies to replicate such area scaling on flexible polyethersulfone (PES) substrates. Initially, we investigated the use of PEDOT:PSS layer as a transparent electrode rather than a brittle ITO layer. Also, we selected blends of P3HT:ICBA as a bulk-heterojunction photoactive layer, sandwiched between a high work function contrast of two electrodes, that is, a polyethylenimine ethoxylated (PEIE)-modified (74) transparent silver layer (84) as electron-collecting electrodes and a MoO₃-induced (85) silver layer as hole-collecting electrodes. The flexible OPDs with a ca. 750 nm-thick photoactive layer prohibits pinholes and defects in the bulk that yields an improved shunt resistance value or reduced parasitic leakage. Figure 5.2 illustrates the fabrication steps, and Figure 5.3 shows the dark J - V characteristics of OPDs with various device areas, 0.5, 0.8, 1.3 cm², using PEDOT:PSS/PEIE as electron-collecting electrodes. As it is clear from this experiment, the dark current densities in reverse bias were found significantly larger than those in OPDs fabricated on glass/ITO substrates. In addition, in forward bias, the current density values in these flexible devices are significantly lower than those found on reference glass/ITO substrates due to a high series resistance. Nevertheless, the 1.3 cm²-device still shows a dark current value of 100 pA/cm² at 0 V, which is in the same level with the state-of-the-art OPD but with a larger size. Furthermore, we characterized the noise of the 1.3 cm²-device by measuring the current fluctuations around the steady-state average dark current at 0 V, shown in Figure 5.4. The rms value of the fluctuations is 4.2 pA, which determines the noise at 0 V.

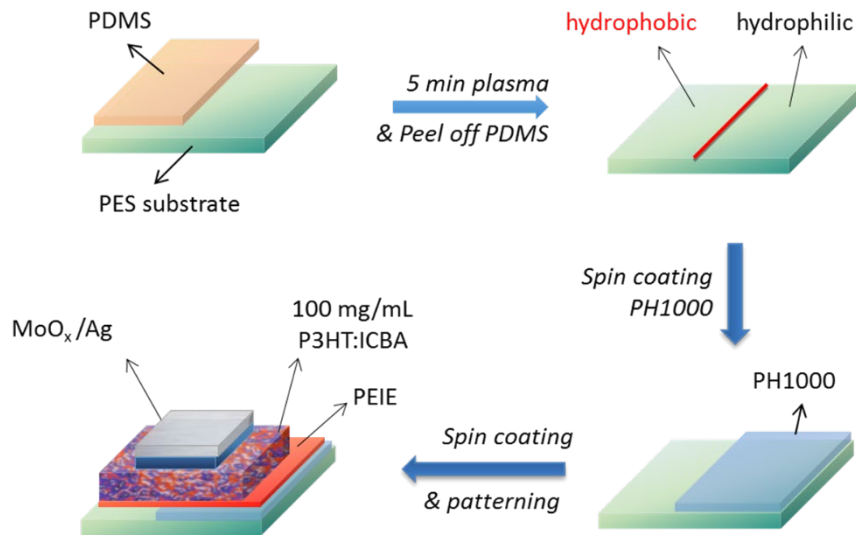


Figure 5.2 Fabrication steps of flexible OPDs using PEDOT:PSS layers as bottom electrodes.

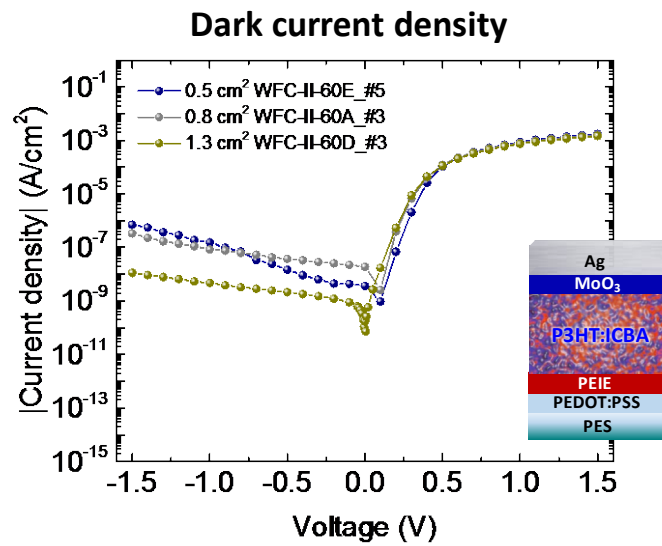


Figure 5.3 J - V characteristics of OPDs with various device areas measured in a dark condition.

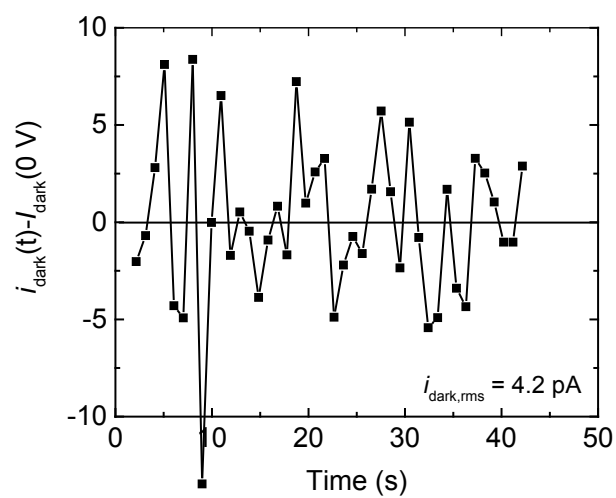


Figure 5.4 Transient dark current fluctuations around steady-state dark current measured at 0 V.

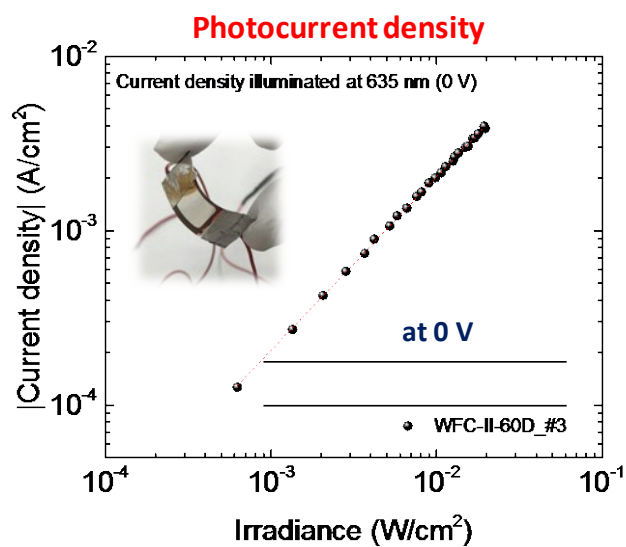


Figure 5.5 Responsivity measurement at 635 nm with a 1.3 cm² OPD.

Next, we further examined the irradiance-dependent photocurrents of the 1.3-cm² OPD operating at 0 V with a laser diode illuminating at 635 nm. The results show that the OPD yields a responsivity value of 0.2 A/W at 635 nm. Next, we can extrapolate a NEP value by $I_{\text{dark,rms}}/\mathcal{R}$, equal to 2.1×10^{-11} W. Therefore, the estimated detectivity value at 635 nm can be derived from Equation (18). That is, $D^*(635 \text{ nm}) = 4.9 \times 10^{11}$ Jones, with a low-frequency bandwidth of 80 Hz.

(ii) Transparent Ag as bottom electrodes

To further improve the performance of flexible OPDs, we used semitransparent Ag as bottom electrodes. Figure 5.6 shows the architecture of the devices. On top of PES substrates, we deposited a 10 nm-thick MoO₃ layer that produces a thin film of nanoporosity and facilitates transparent silver growth onto without generating isolated islands (84, 86-88). The decreased transmittance value in the near infrared region reveals that the transparent silver layer reaches the percolation threshold and become a conductive layer, shown in Figure 5.7.

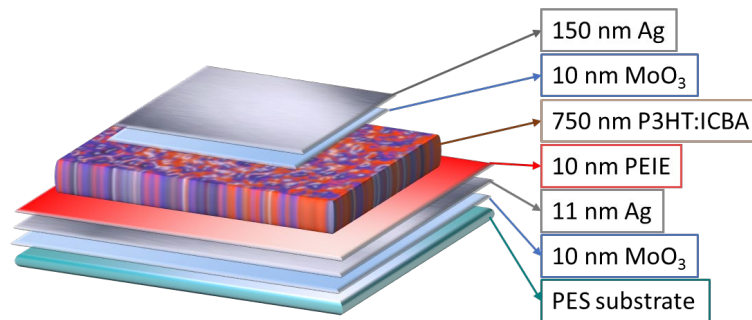


Figure 5.6 Device structure of OPDs with Ag as bottom electrodes.

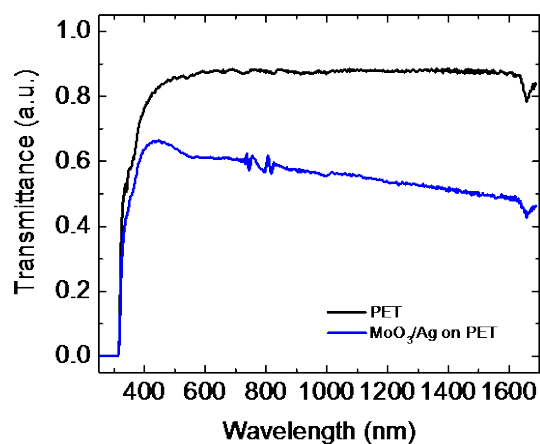


Figure 5.7 Transmittance of transparent Ag on a PET substrate.

As shown in Figure 5.8, the J_{dark} in reverse bias in OPDs fabricated on PES substrates with an area of 0.1 cm^2 present comparable values to those of OPDs fabricated on rigid ITO/glass substrates.

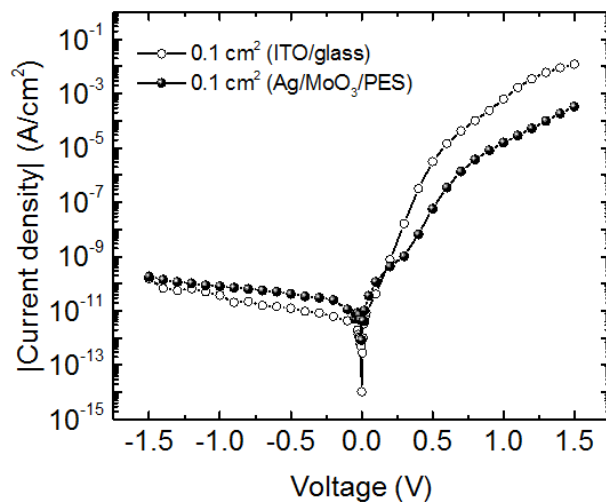


Figure 5.8 A comparison of dark J - V characteristics of OPDs fabricated on glass and PES substrates.

Next, we increased the photoactive area from 0.1 to 1.0 cm² and compared their dark current density values. Figure 5.9 (a) presents the measured of the steady-state current characteristics of OPDs under dark condition. The data reveal that there is no substantial discrepancy under forward bias because of limited parasitic effects caused by the series resistance when the photoactive area is increasing; under reverse bias conditions, the current density values increase to several nA/cm² primarily because more defects or pinholes occur in large-area devices with higher possibility (32, 89). In fact, to achieve OPDs with low-power consumption, we need focus on the performance of OPDs operated at low voltages. We found that the current density values of these devices are in the range of pA/cm² when the reverse bias is less than 0.1 V. To our best knowledge, this is the lowest dark current density value of flexible and large-area OPDs reported in the literature to date. To evaluate the performance, we compared our OPDs with bulky Si counterparts. Figure 5.9 (b), the flexible OPDs exhibit low dark current density values comparable to those of the state-of-the-art low-noise Si-PDs (Hamamatsu S1133 and S1227-1010BQ) of similar area sizes, 0.1 and 1.0 cm², respectively. Furthermore, the 1.0 cm² flexible OPDs show the dark current density values >40 times lower than the 0.9 cm² Si PDs for general industrial measurement (Hamamatsu S12497). From these results, large-area and flexible OPDs constitute a real breakthrough in the photodiode fields.

To further explore the noise level in these OPDs at 0V, we captured the current fluctuations measured in a dark condition, shown in Figure 5.10. The rms values, which present the magnitude of noise, are 52.7 and 87.4 fA in OPDs of 0.1 and 1.0 cm², respectively; a comparable value to that of rigid P3HT:ICBA OPDs, shown in chapter 4.

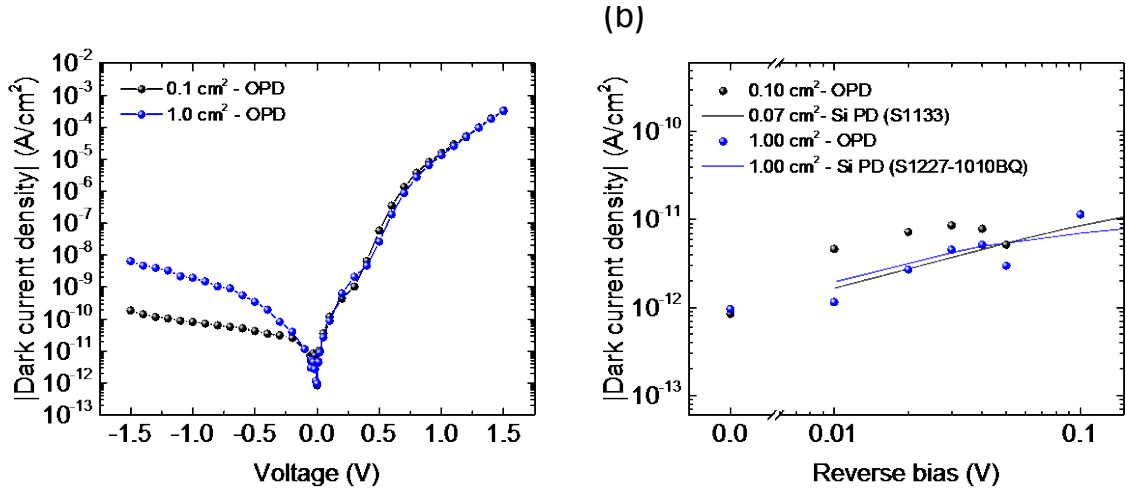


Figure 5.9 (a) The measured steady-state dark J - V characteristics of OPDs with 0.1 and 1.0 cm². (b) Comparison of the dark current densities at low-voltage operation between Si PDs and OPDs with similar sizes.

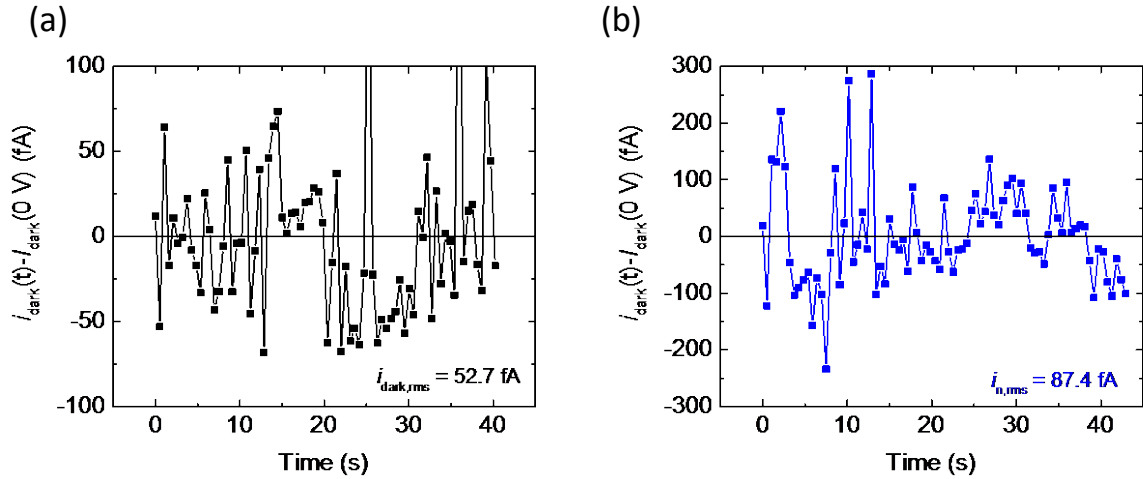


Figure 5.10 Transient dark current fluctuations around steady-state dark current measured at 0 V in (a) an 0.1 cm², and (b) an 1.0 cm² OPD.

5.2.2 Responsivity

To check that large-area (1.0 cm^2) OPDs generate uniform photocurrents, we characterized the responsivity at 0 V illuminated with a laser diode at 635 nm at four locations of the photoactive area and compared that of 0.1 cm^2 OPDs. An averaged responsivity value of 0.09 A/W with a standard deviation value of 0.01 A/W was obtained in large-area OPDs, which is consistent with a responsivity value of 0.10 A/W in OPDs of 0.1 cm^2 , shown in Figure 5.11 (a) and (b).

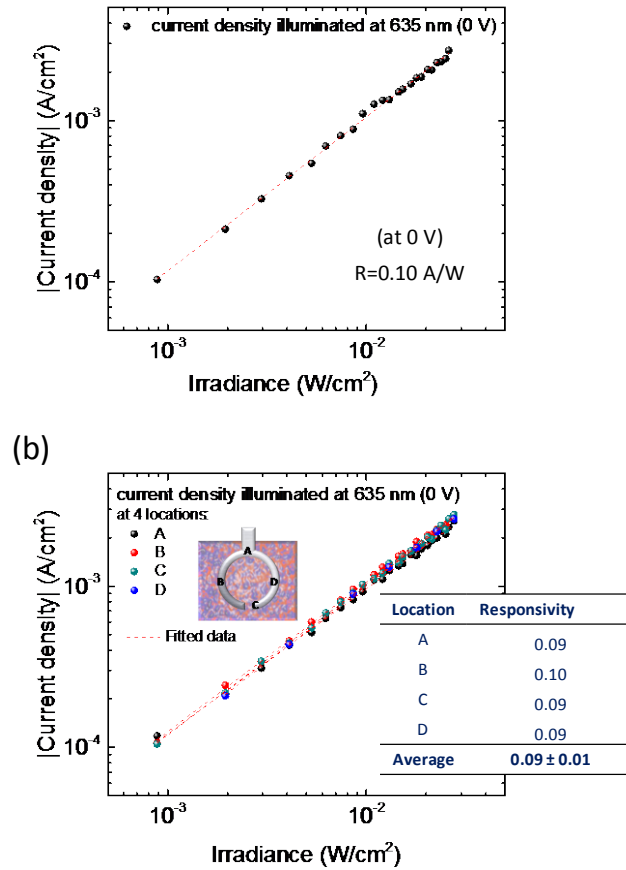


Figure 5.11 (a) Responsivity measurement at 635 nm with a (a) 0.1 cm^2 and a (b) 1.0 cm^2 OPD operating at 0 V.

5.2.3 Noise Equivalent Power and Specific Detectivity

To realize a next-generation high-detectivity OPDs, a drastic reduction of the noise current value ($I_{dark,rms}$) is required. An important metric, noise equivalent power (NEP), which stands for the minimum optical power that a detector can sense at signal-to-noise ratio (SNR) and bandwidth equal to unity (61). In previous sections, we showed a direct measurement of dark current fluctuation that represents the noise level with a bandwidth of 80 Hz in the flexible OPDs. Combined with the responsivity values, we can be able to estimate the NEP values at 80 Hz and 635 nm by $NEP=I_{dark,rms}/R$, which are 527 and 969 fW in 0.1 and 1.0 cm² flexible OPDs, respectively. As a result, the D^* value at 635 nm in the large-area and flexible OPD can be estimated by Equation (18), showing a D^* (80 Hz, 635 nm) value of 9.2×10^{12} Jones.

5.2.4 Field of View

The sensing directionality of the flexible OPDs can be characterized by the field of view (FOV). The measurement was conducted with a 525 nm laser illuminating at the flexible OPD mounted on a rotation stage. We normalized the photocurrents by that at 0 degree, when the OPD is perpendicular to the light path. The results reveal that the half angle, where the photocurrent is half of the maximum value, is ca. ± 75 degrees, suggesting that the flexible OPDs allow a wide angle for sensing.

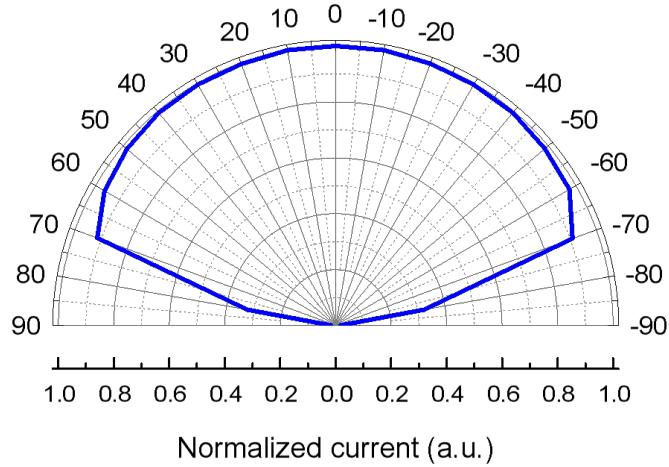


Figure 5.12 FOV measurement of flexible OPDs.

5.3 Photoplethysmogram

With the capability to fabricate large-area flexible OPDs with the low dark current values, we gain higher freedom to design the pattern of devices in various geometry, depending on the desired applications. In addition, without integration between small devices, the sensing system become simple design and potentially cost effective. Here, we demonstrated a physiological detector by monitoring photoplethysmogram (PPG). PPG is a noninvasive technique, composed of a light source and a photodetector, which optically detects the changes of blood vessel volume in the microvascular bed of tissues for heart rate monitoring. The volume of subdermal blood vessels changes as the arterial pulsation, so it modifies the absorptive, reflective, and scattered light through skin. Thus, the photodetector can be monitor the pulsation signals, including diastolic and systolic signals (38, 90-93), depicted in Figure 5.13.

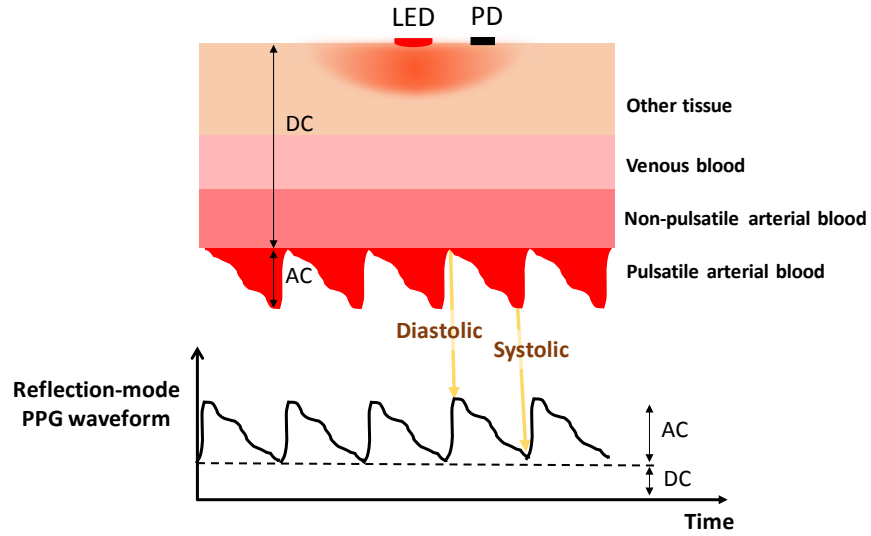


Figure 5.13 Concept of PPG measurement in a reflection mode.

To evaluate the advantages of OPDs, we estimated power consumption of PPG measurements on the finger, and compared that with Si counterparts. To collect scattered signals from skin efficiently, we designed our low-dark-current OPDs in a ring geometry (hereinafter referred to as ring-OPDs). We performed PPG measurements in reflectance mode by placing a low-noise Si PD (Hamamatsu S1133) or a ring-OPD and a light-emitting diode (LED) on the same plane. To acquire PPG signals, we placed a surface-mounted LED (i) from a Si PD at a distance of 7 mm (ii) at the center of ring-OPD with a radial distance of 7 mm on the finger, shown in Figure 5.14 (a). The LED illuminated at a wavelength of 635 nm biased with a DC power supply. The variations of PPG signals were measured with the voltage across a $1\text{M}\Omega$ resistor, connecting with a PD in series, and then amplified with a twenty times DC gain through a 0.1-10 Hz bandpass filter. Figure 5.14 (b) illustrates the setup scheme. The photoactive area of commercial low-noise Si PD is 0.07

cm^2 , while that of the ring-OPD is 1.0 cm^2 . We operated both photodetectors at 0 V that minimized the overall power consumption.

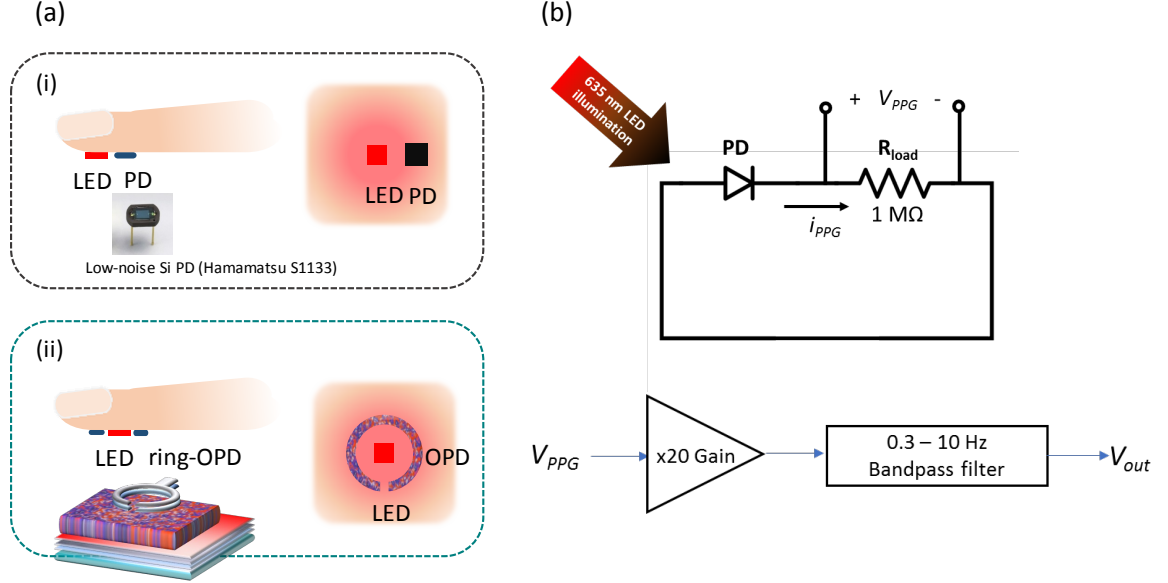


Figure 5.14 The setup of PPG measurements. (a) Schematic illustration of reflectance-mode PPG measurements with (i) a Si PD and (ii) a ring-OPD. (b) Circuit of PPG signal readout.

In Figure 5.15, the PPG signals were measured under varying optical power of LED illuminated at wavelength of 635 nm. Since the Si PD and the ring-OPD generate comparable dark current values at 0 V, they exhibit similar values of PPG amplitude when under high optical intensity, e.g. an electrical power of 9.7 mW driving to the LED. Then we monitored the PPG amplitudes when gradually reducing the electrical power that supplies to the LED. When the optical power of LED decreases, less scattered photons reflecting PPG signals are collected by photodetectors. Consequently, the noises primarily resulting from white noise, such as circuit electrical coupling and thermal fluctuations,

become dominant. However, the ring-OPD collect PPG signals more efficiently due to its symmetric geometry with large area and therefore shows improved SNR values. In addition, ring-OPDs on flexible substrates allow compatible contact with skin that reduces motion artifacts. The ring-OPD only required $25.7 \mu\text{W}$ whereas the low-noise Si PD needed $246.7 \mu\text{W}$ to drive the LED that maintains a similar SNR value closed to 1. The results suggest that using ring-OPDs significantly reduces the power consumption for PPG measurements compared to using the state-of-the-art low-noise Si PDs, which is a major breakthrough for wearable electronics.

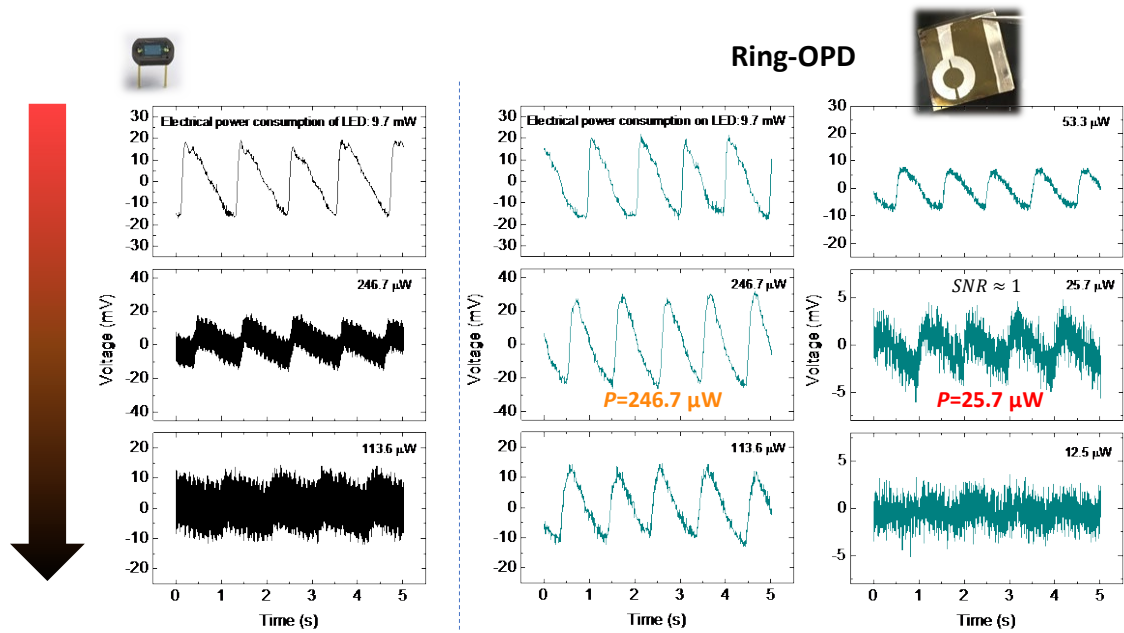


Figure 5.15 The measured of PPG signals with varying optical power of LED illuminated at 635 nm, sensing with (a) a low-noise Si PD (Hamamatsu S1133), (b) with a ring-OPD.

5.4 Summary

In this chapter, we evaluated the scalability of solution-processed P3HT:ICBA OPDs on rigid ITO substrates with unprecedented low dark current density (10^{-12} A/cm²), which leads to high detectivity values approaching 10^{14} Jones in the visible spectrum. In addition, we successfully demonstrate large-area flexible OPDs to 1.0 cm², and they show dark current density values comparable to those of commercial low-noise Si photodiodes (Si PDs). We further took advantages of these combined properties and designed the OPDs in a ring geometry for efficient signal collection. We measured photoplethysmogram with the OPDs, which consumed 9.6 times less power than low-noise Si PDs as the signal-to-noise ratio equal to one.

CHAPTER 6. A METHOD FOR DECREASING THE DARK CURRENT IN THIN DEVICES

6.1 Introduction

In the previous chapter, we demonstrated a proper selection of organic materials, which allows us to develop OPDs with an unprecedented level of performance; rivaling that of low-noise Si PDs in all figures of merit except their response time. The response time can be improved by decreasing the thickness of photoactive layers. However, a thin photoactive layer generally introduces low shunt resistance in devices, leading to increased dark current density and high electronic noise in OPDs. Strategies that suppress the dark current values in OPDs, such as insertion of injection blocking layers or increase in the thickness of photoactive layers, have been widely studied (16, 31-33, 94). Yet, these methods generally impose additional series resistance leading to a decreased responsivity value and a limited linear dynamic range. As a result, developing a low-noise OPD using an amorphous or thin photoactive layer remains challenging to date. In this chapter, we develop a superficial treatment using ALD techniques to reduce electronic noise for 200 nm-thick OPDs, which show comparable responsivity values and an improved linear dynamic range comparable to those with 500 nm-thick active layer.

6.2 Dark Current Reduction in PMA-Doped Devices

Figure 6.1(a) depicts the device structure of PMA-doped photodiodes. The device structure is ITO/PEIE (10 nm)/PMA-doped P3HT:ICBA (200 nm)/Ag (150nm). The

photoactive layer was superficially treated using atomic layer deposition (ALD) with Al_2O_3 deposition recipe, composed of one pulse of water followed by one pulse of TMA with desirable cycles. As a reference, we also fabricated a PMA-doped device without ALD treatment on photoactive layers. Figure 1(b) shows the stabilized current density-voltage (J - V) characteristics measured under dark condition at room temperature. After 1 cycle of Al_2O_3 treatment, the dark current density (J_{dark}) values in reverse bias (from -1.5 V to -0.5 V) decrease more than four orders of magnitude, from 10^{-6} A/cm² to 10^{-11} A/cm² range. In particular, the ALD-treated device shows a low J_{dark} value of 2.2×10^{-11} A/cm² at 0 V. On the other hand, the current density value at 1.5 V of the ALD-treated device shows comparable to that of a reference device without ALD treated. These results imply that 1 cycle of Al_2O_3 treatment increases the shunt resistant (R_p) but does not tremendously increase the series resistance (R_s) in photodiode devices.

To optimize the condition of ALD treatment, we also fabricated devices treated with Al_2O_3 and HfO_2 with various cycle numbers, depicted in Figure 6.2. Among all of the conditions we attempted, 1 cycle of Al_2O_3 treatment enables lowest J_{dark} values in reverse bias but highest J_{dark} values in forward bias.

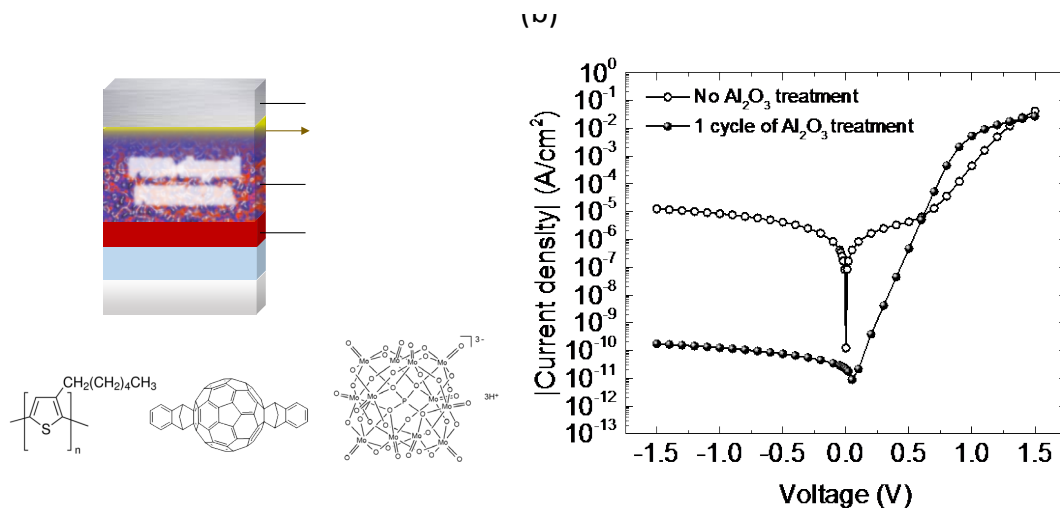


Figure 6.1 PMA-doped OPD devices treated with ALD. (a) Device structure and chemical structure of P3HT, ICBA, and PMA. (b) A comparison of stabilized J - V characteristics measured under dark of PMA-doped devices and those with 1 cycle of Al_2O_3 treatment using ALD.

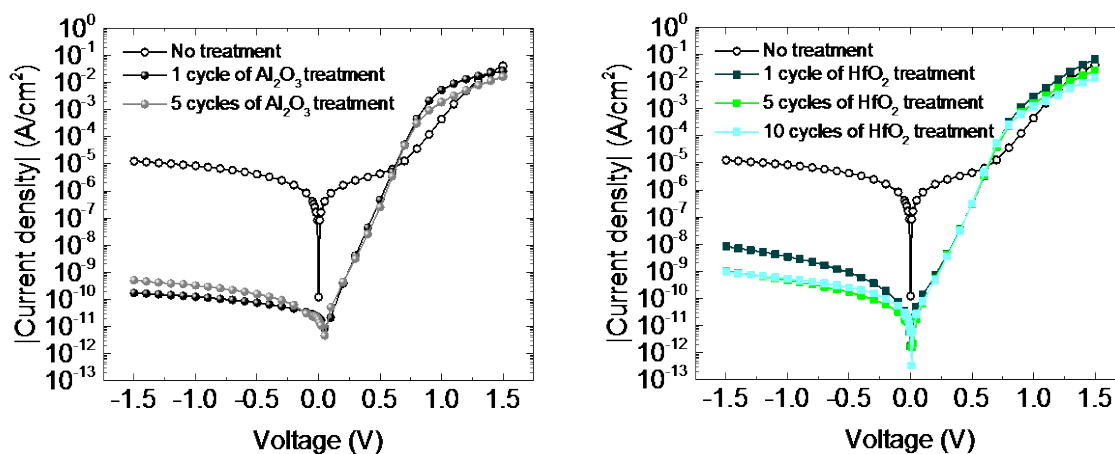


Figure 6.2 Stabilized J - V characteristics measured under dark of PMA-doped devices with (a) Al_2O_3 and (b) HfO_2 treatment with various cycle numbers using ALD.

6.3 Simulation of J - V Characteristics

Next, we conducted current density – voltage irradiance-dependent studies at room temperature, over ca. 9 orders of magnitude of irradiance (*i.e.*, 10^{-10} – 10^{-1} W/cm²), shown in Figure 6.3 (a). Short-circuit current density (J_{sc}) and open-circuit voltage (V_{oc}) characteristics can be derived from the Prince equivalent circuit model, expressed by Equation (14). If R_s is sufficiently small, then J_{ph} can be approximated to J_{sc} . The J - V experimental data under illumination fit the simulated results using Equation (15), with an n , J_0 , and R_pA value of 1.65, 1.8×10^{-11} A/cm², 10 G Ω -cm², respectively. To validate these simulated parameters, we reconstructed the J - V characteristics under dark using the equivalent model, shown as Equation (14), and the results show high consistency with the experimental data, shown in Figure 6.3 (b). Table 2 summarizes the parameters extracted from the equivalent circuit model.

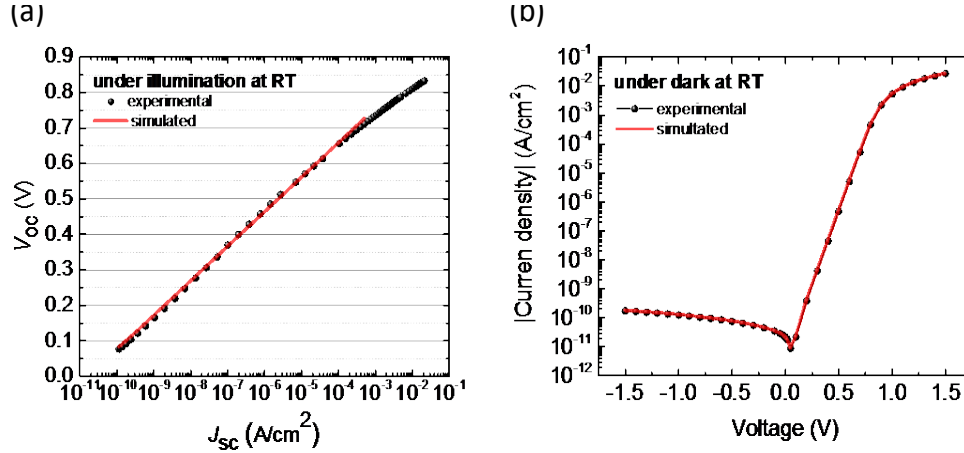


Figure 6.3 Measured and simulated J - V characteristics at room temperature of ALD-treated OPDs and the parameters derived from equivalent circuit model. (a) V_{oc} - J_{sc} characteristics illuminated under 9 orders of magnitude of irradiance, 10^{-10} – 10^{-1} W/cm². (b) J - V characteristics under dark. The table summarizes the parameters.

Table 2 Parameters extracted from the equivalent circuit model.

J_0 (pA/cm ²)	n	$R_p A$ (G Ω -cm ²)	$R_s A$ (Ω -cm ²)	A (cm ²)
18	1.65	10	20	0.12

6.4 Photodetector Performance

To further evaluate the ALD-treated OPDs as photodetectors, we performed spectral responsivity measurements, linear dynamic range measurements, and noise equivalent power measurements. Finally, we will also discuss the specific detectivity and response time of these OPDs.

6.4.1 Responsivity

In Figure 6.4, the spectral responsivity results show that the OPDs enable photoresponse in the visible range and yield a peak value of 0.26 A/W at 555 nm illumination. In addition, compared to untreated reference OPDs, 1 cycle of Al₂O₃ treatment does not degrade the performance in responsivity values. In other words, the treatment does not provide a severe barrier for carrier collection, and OPDs yield comparable R_s values. However, when the device was treated with 5 cycles of Al₂O₃, the responsivity values decrease. The higher cycle number of ALD treatment, the more insulator on the photoactive layer, forming a severe barrier for carrier collection and leading to a reduction in responsivity values. Furthermore, we found that the responsivity values of ALD-treated (1 cycle) device are on par with those of untreated devices with 500

nm-thick photoactive layer, meaning photons can be efficiently absorbed within a 200 nm-thick P3HT:ICBA layer, shown Figure 6.5. In addition, ALD-treated thin devices (200 nm) yield lower dark current density values in reverse bias than those of thick devices (500 nm) without treatment.

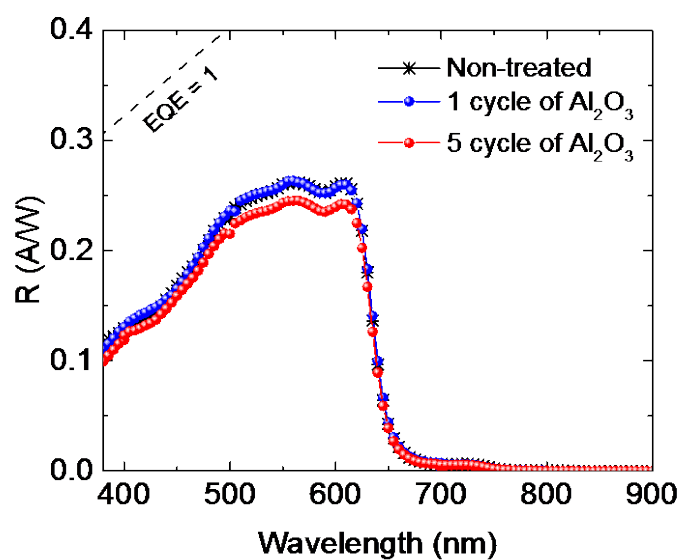


Figure 6.4 A comparison of spectral responsivity measurements of devices without treatment and with 1 and 5 cycles of treatment.

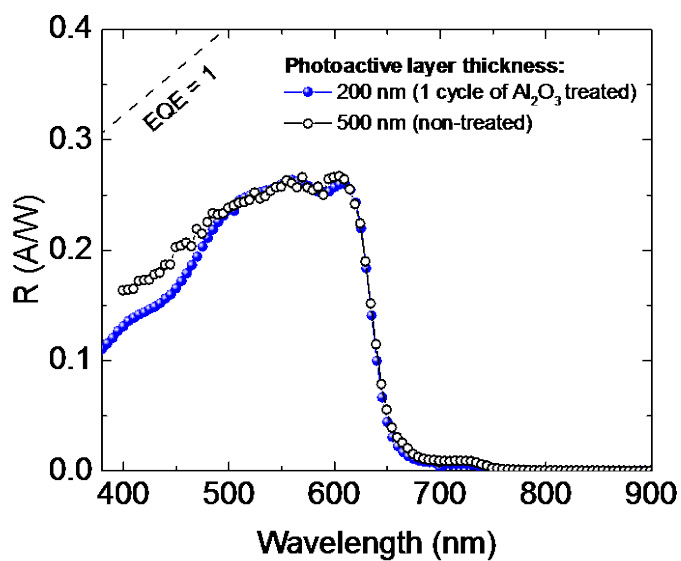


Figure 6.5 A comparison of spectral responsivity measurements in devices with a 200 nm- and 500 nm-thick photoactive layer.

6.4.2 Linear Dynamic Range

Next, we investigated the linear dynamic range (*LDR*) of the ALD-treated OPDs. *LDR* defines as the region where photocurrent density shows linearly dependent on irradiance, in a unit of dB, expressed by Equation (18). Figure 6.6, the ALD treated OPD shows high linearity over 6 orders of magnitude, showing a *LDR* value larger than 136 dB. When the OPDs are illuminated at 2 mW, the photocurrents still show high linearity, suggesting that the PMA-doped thin devices enable moderate series resistance and mitigate bimolecular recombination losses at high optical power (67). However, working as a low-light level sensing photodetector, we need to pay attention to the performance under low illumination. The photocurrents decay sublinearly when the optical power decreases to the sub-nW range, where responsivity values start to roll off.

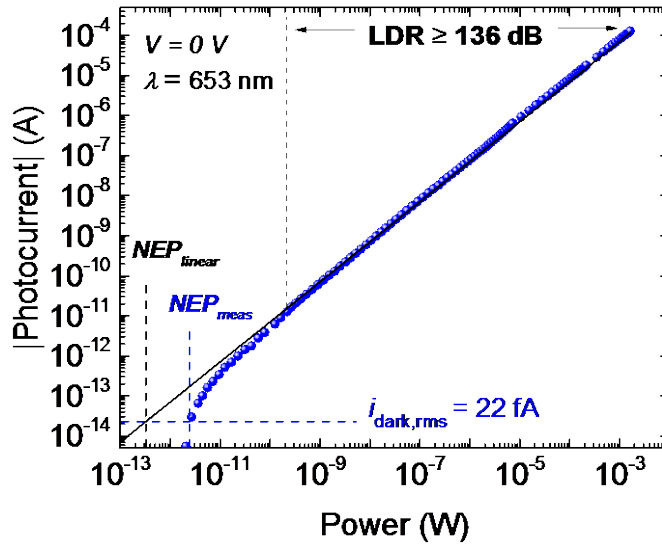


Figure 6.6 . Measurement of linear dynamic range at 653 nm showing larger than 136 dB and the measured noise current under dark equal to 22 fA.

6.4.3 Noise Equivalent Power and Specific Detectivity

Next, to further investigate the electronic noise in the OPDs, we captured the temporal dark currents using an electrometer with an internal bandwidth of 80 Hz and quantified the noise as the fluctuations around the steady-state average dark current, presented in a root-mean-squared (rms) value calculated over a set of discrete data points ($I_{dark,rms}$). As shown in Figure 6.7, the OPDs show an $I_{dark,rms}$ value of 22 fA resulting in an estimated noise equivalent power value of 0.3 pW at 653 nm, calculated by $NEP = \frac{I_{dark,rms}}{\Re}$. However, it is worth noting that, in most of the cases, photocurrents deviate from linearity at low optical power possibly caused from charge-trapping effects, leading to a discrepancy in responsivity value and an implausible NEP value. Therefore, here, we conducted a direct measurement of temporal photocurrent associated with a gradual increase in optical power from dark to 4.9 pW, shown in Figure 6.8 (a). Figure 6.8 (b) suggests that the minimum detectable optical power at 653 nm is ca. 2.8 pW, where the signal-to-noise ratio equals to one, representing the measured noise equivalent power (NEP_{meas}) of the OPDs.

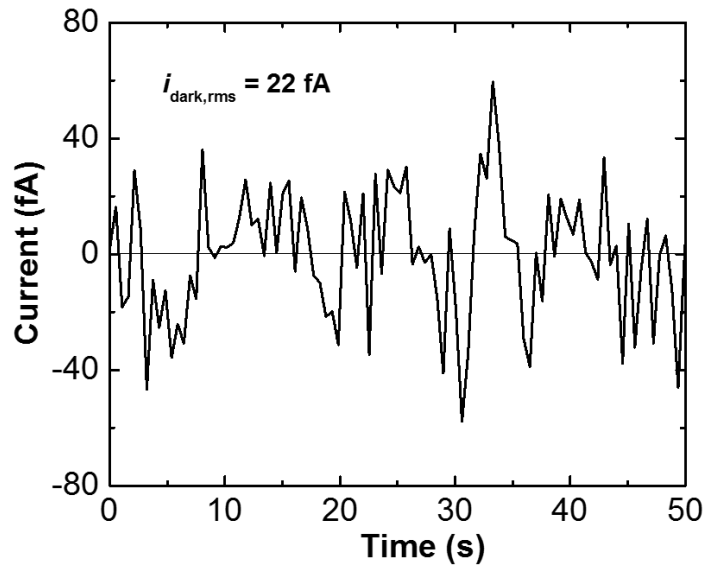


Figure 6.7 Current fluctuations measured under dark.

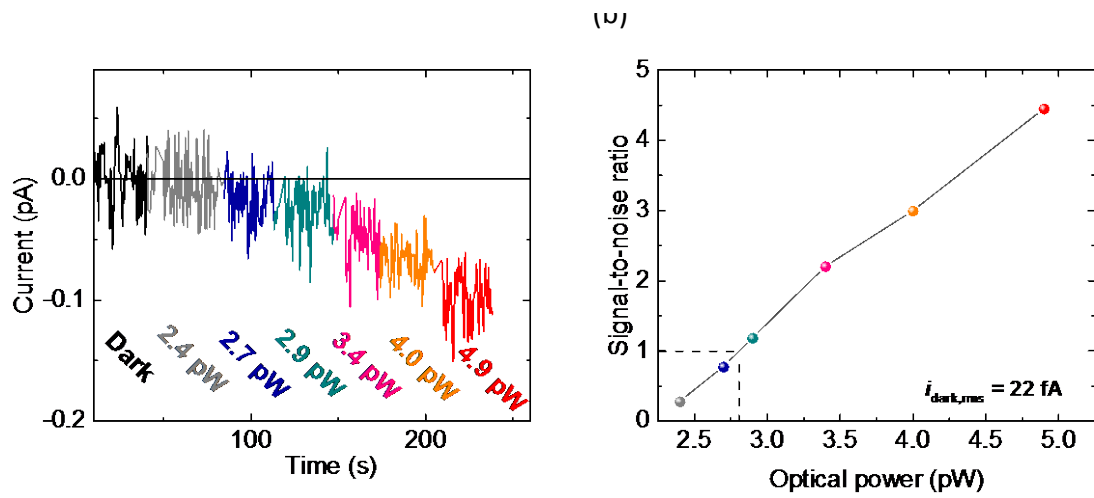


Figure 6.8 Direct measurement of *NEP*. (a) Temporal photocurrents corresponding to a gradual increase of optical power. (b) Minimum detectable optical power associated with the noise equivalent power at 653 nm derived from the signal-to-noise ratio equal to one.

Next, the measured specific detectivity (D_{meas}^*) value can be therefore obtained by $D^* = \frac{\sqrt{AB}}{NEP}$, where A is device area and B the measurement bandwidth. These results lead to a peak D_{meas}^* value of 7.5×10^{12} Jones at 555 nm. In fact, the NEP is wavelength dependent. If the devices illuminated at the wavelength where generates peak responsivity values, the R values most likely remain constant or even increases with a photoconductive gain at lower optical power illumination, leading to a lower NEP value and higher D^* value. In other words, a constant responsivity leads to a D_{linear}^* value higher than D_{meas}^* value. In addition, when a device is operating at a high frequency, white noise becomes the limiting factor. Therefore, we approached the white noise value by providing the simulating parameters from the equivalent circuit model (discussed in the previous section), equals to 1.3×10^{-15} A/Hz^{-1/2}, leading to an unprecedented peak value of 7.2×10^{13} Jones for thin device. In Figure 6.9, we showed the spectral detectivity values of D_{meas}^* and D_{linear}^* derived from NEP_{meas} and NEP_{linear} , respectively. The detectivity value limited by the white noise (D_{white}^*) is compared with D_{meas}^* and D_{linear}^* operating at 80 Hz.

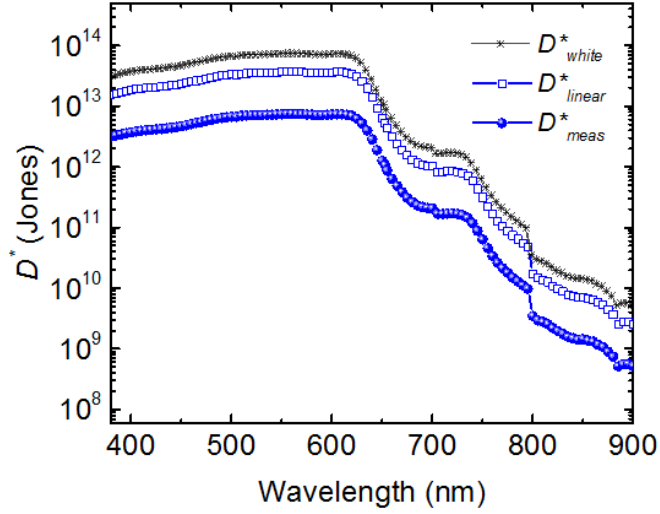


Figure 6.9 Specific detectivity values derived from measured *NEP* and linear *NEP* value operated at 80 Hz, and white noise limited specific detectivity values.

6.4.4 Response Time

Finally, we studied the response time of the ALD-treated OPDs. Response time of a photodetector is defined by the duration when the photocurrent arises from 10% to 90% or declines from 90% to 10%, referred to rise time and fall time, respectively. We monitored the voltage decay across a 100 Ω load resistance as a function of time, which reflects the transient photocurrent during the fall time. First, we studied the response time of OPDs operating at different external applied bias. In Figure 6.10(a), the ALD-treated OPDs (200 nm-thick) yield response time of 10.0 ± 0.1 μ s operating at 0 V and 10.9 ± 0.1 μ s operating at -3 V. The results show that the external apply bias only has minor impact on the response time of PMA-doped P3HT:ICBA devices. We believe that the response time of the OPDs is limited by the hopping transport mechanism of the photogenerated

carriers; the shorter travel distance for the carriers results in the faster response. To validate the measurement is not limited by the RC time constant, we increased the thickness (d) of the photoactive layer from 200 nm to 700 nm but kept the same device area (A), leading to an lower intrinsic capacitance ($C = \epsilon \frac{A}{d}$), and then demonstrated the same measurement. The 700 nm-thick device operating at 0 V, -1 V, and -2 V shows response time of $16.4 \pm 2.4 \mu\text{s}$, $17.4 \pm 2.5 \mu\text{s}$, and $17.8 \pm 2.4 \mu\text{s}$, respectively, independent of external bias too. Compared the response time of these two OPDs with different thickness, we demonstrated that the thin devices enable fast photoresponse. The results also can be found in other systems, such as the intrinsic P3HT:ICBA devices, shown in Figure 6.10(b).

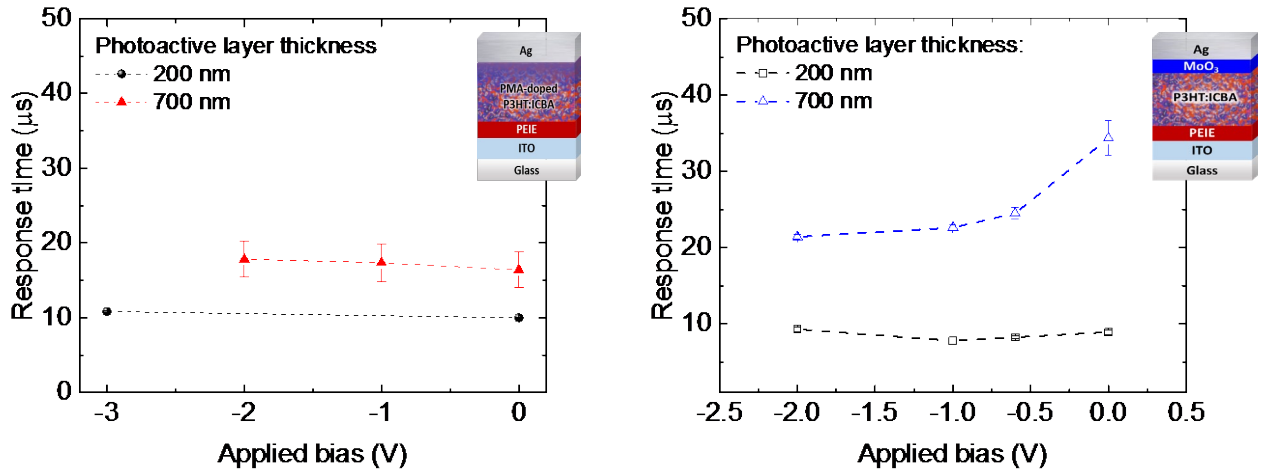


Figure 6.10 Response time of OPDs with different thickness. (a) PMA-doped P3HT:ICBA OPDs. (b) Intrinsic P3HT:ICBA OPDs.

Second, we investigated the irradiance-dependent response time by illuminating the OPDs under two different optical power, ca. 1.7 nW and 3.5 μW. Again, we monitored the

temporal voltage decay across the load resistance, which is linearly dependent on the photocurrent. A long tail in the decay profile was observed after a high optical power (in the range of μW) was applied, which delays the response of OPDs. To rationalize the dynamics of photocurrent, we proposed a two-exponential decay function to describe the profile of normalized photocurrent in the fall period, expressed by

$$V(t) = m_1 e^{-\frac{t}{\tau_1}} + (1 - m_1) e^{-\frac{t}{\tau_2}} \quad (27)$$

The photoresponse dynamics composes of two behaviors: the first term refers to the fast component associated with τ_1 while the second term refers to the slow component associated with τ_2 . In equation (27), t is the time and light source is off while $t \geq 0$; $V(t)$ is the normalized temporal voltage across the load resistance; m_1 and $(1 - m_1)$ is the weight of the fast response and slow response, respectively; τ_1 and τ_2 is the characteristic decay time constant for fast response and slow response, respectively. Figure 6.11, the OPDs show faster photoresponse under illumination of nW than μW in optical power. Two fits were generated by a mutual fitting process, enabling a shared τ_1 and τ_2 value in both of the illumination conditions. The results show a τ_1 value of $3.09 \pm 0.01 \mu\text{s}$ and a τ_2 value of $5.64 \pm 0.01 \mu\text{s}$. When the OPD was illuminated at ca. $3.5 \mu\text{W}$, the photoresponse contained a fast component (τ_1) with 41.7% and a slow component (τ_2) with 58.3%. When the optical power decreased to 1.7 nW , the long tail vanished, leading to a single-exponential decay in photoresponse with a single time constant $3.09 \pm 0.01 \mu\text{s}$. The inset in Figure 6.11 shows the fitting residual, and table 1 summarizes the fitting parameters.

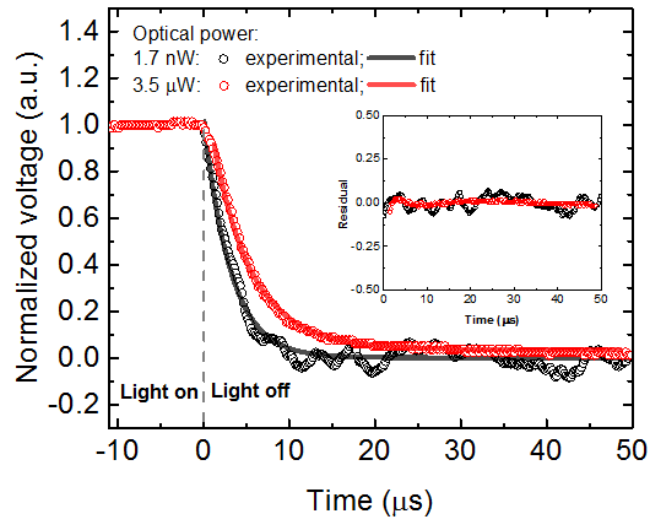


Figure 6.11 Photocurrent decay profile of ALD-treated OPDs illuminated with different optical power. The dynamics follows a single exponential decay with a time constant of $3.09\ \mu\text{s}$ illuminated at $1.7\ \text{nW}$.

Table 3 Fitting parameters of photocurrent decay generated with different optical power.

Estimated optical power	τ_1	τ_2	m_1
1.7 nW	$3.09 \pm 0.01\ \mu\text{s}$	$5.64 \pm 0.01\ \mu\text{s}$	1
3.5 μW			0.42

6.5 Application to Other Systems

To investigate the generality of the ALD treatment for reducing J_{dark} in different type of OPDs, we additionally fabricated and ITO/PEIE (10 nm)/P3HT:ICBA (200 nm)/MoO₃ (10 nm)/Ag devices and ITO/PEIE (10 nm)/PDPP3T:PC₇₁BM (80 nm) /MoO₃ (10 nm)/Ag devices treated them with Al₂O₃ with various cycle numbers. Figure S2 and S3 show the J_{dark} values in reverse bias can be lowered from 10⁻⁴ A/cm² to 10⁻⁶ A/cm². With the 10 cycles of Al₂O₃ treatment for PDPP3T:PC₇₁BM devices, the dark current density at 0 V decreased to 130 pA/cm² that can be differentiated from the photocurrents, showing a peak responsivity value to 0.12 A/W at 850 nm (Fig. S2b).

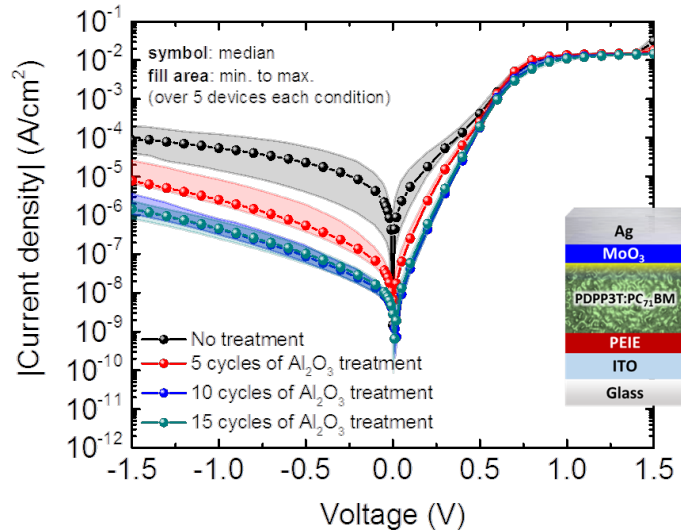


Figure 6.12 Stabilized dark J - V characteristics of ITO/PEIE (10 nm)/PDPP3T:PC₇₁BM (80 nm) /MoO₃ (10 nm)/Ag devices with 5, 10, and 15 cycles of Al₂O₃ treatment. Symbols refer to the mean value and filled areas refer to the range of minimum to maximum, calculated over five devices for each condition.

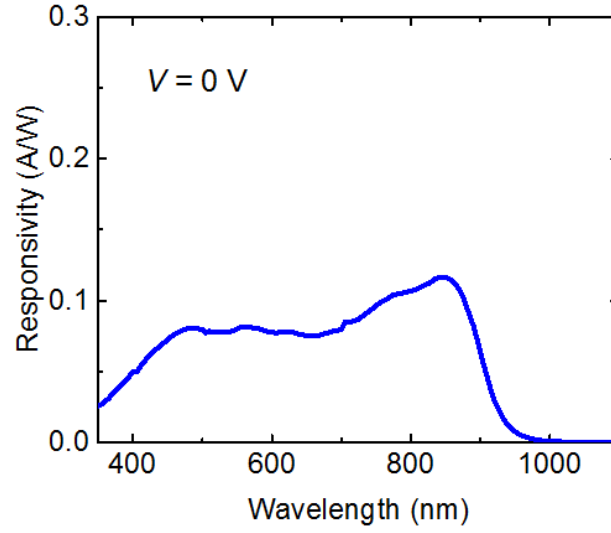


Figure 6.13 Spectral responsivity of the device with 10 cycles of Al_2O_3 treatment.

Moreover, reproducibility of the J_{dark} values in reverse bias is found to become higher with more cycle numbers of ALD treatment, illustrated in Figure 6.13(a) and Figure 6.14. In Figure 6.14, we show the error bars as the standard deviation value for each measurements and symbols refer to the mean value. The standard deviation show smaller when more cycle numbers are applied. Thus, this technique provides higher consistency between devices and is potentially useful for fabricating large-area OPDs. However, J_{dark} at 1.5 V become smaller with higher cycle numbers, indicating a sacrifice in R_s in the meanwhile. It is because that a thicker insulator layer introduces a higher barrier to collect carriers from electrodes. Therefore, there exists tradeoff between reproducibility and parasitic resistance in this method.

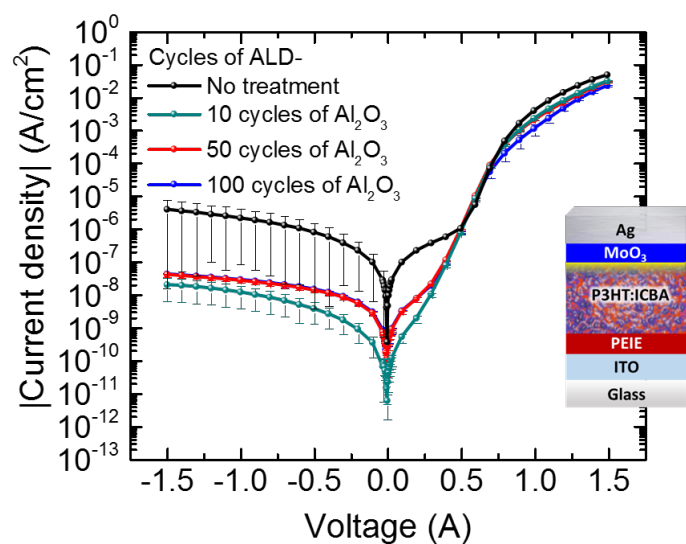


Figure 6.14 Stabilized dark J - V characteristics of ITO/PEIE (10 nm)/P3HT:ICBA (200 nm)/MoO₃ (10 nm)/Ag devices with 10, 50, and 100 cycles of Al₂O₃ treatment. Symbols refer to the mean value and error bars refer to the standard deviation, calculated over five devices for each condition.

6.6 Summary

In this work, we developed an approach to reducing the dark current values without significantly increasing the series resistance in OPDs by introducing superficial treatment on photoactive layers using the ALD technique. In addition, this method can be effectively used in various systems and enable a high shunt resistance in thin devices. In the past, we reported a solution-processed electrical p-doping technique by immersion photoactive layers into a PMA solution, showing increased electrical conductivity and improved photo-oxidation in air of the polymeric films(95, 96). Here, we leverage the PMA doping results combined with the ALD treatment technique, a 200 nm-thick P3HT:ICBA OPD shows a reduced dark current density value of 21.6 pA/cm² at 0 V, linear dynamic range (*LDR*) larger than 136 dB, and a white noise limited specific detectivity (D^*) value of 7.3×10^{13} Jones. In addition, by introducing PMA doping and decreasing the photoactive layer, the OPDs show response time of 3.0 μ s operating at 0 V. A faster photoresponse dominated with a single-exponential decay is observed under weaker optical power illumination, the behavior is different from the intrinsic P3HT:ICBA thick devices. Therefore, this technique potentially provides a solution for organic photodetectors to monitor short pulse light at weak optical power in the range of nW such as scintillators in radiation detection.

CHAPTER 7. CONCLUSIONS AND FUTURE WORK

7.1 Conclusions

In this work, first, we achieved high-performance organic photodiodes that enable unprecedented detectivity value of 8×10^{13} Jones that are comparable to those of low-noise inorganic counterparts but at a lower voltage and with room temperature operation. As discussed in chapter 4, we learned that the reverse saturation current density that stems from the thermal generation/recombination of carriers plays a crucial role in determining the J_{dark} and electronic noise in organic photodiodes. The physical insights allowed us to select a proper combination of materials with weak electronic interaction in bulk heterojunction. In particular, P3HT:ICBA OPDs produce J_{dark} near 0 V in the range of pA/cm², which is 2 orders of magnitude lower than that of state-of-the-art OPDs (60).

State-of-the-art crystalline inorganic photodiodes possess restrictions in manufacturing control of defects over large areas, which introduces to challenges to enable high detectivity values over increasingly large areas and simple design of applications at low cost (80). Based on the achievement discussed in chapter 4, we used the same method and developed flexible OPDs in 1.0 cm² with high detectivity approaching 10^{13} Jones, which rival those of flexible OPDs with small areas in ca. 0.1 cm² (52, 97). Next, these OPDs in a ring geometry collect PPG signal efficiently, and we found the power consumption is lower than using the conventional Si PDs. We believe that the achievement will open a route to develop reliable biometric applications for next generation.

Finally, we discovered a superficial treatment using ALD to reduce the electronic noise in OPDs with thin active layers. On the contrary to the state-of-the-art strategies (32, 74), this technique does not significantly decrease the responsivity in devices. By using this technique, we improved the response time and linear dynamic range in a 200 nm-thick OPDs. In addition, this technique enables a response time of 3.1 μ s in PMA thin devices, providing a solution to the problem of sensing a continuous pulse of light with weak optical power, such as scintillators used in radiation detection.

7.2 Future Work

The scope of the work presented in this thesis can be further developed and extended in a plenty of directions. The recommended future work includes investigation of device performance and exploration for sensing applications.

7.2.1 Device Stability

Assessing OPD device stability is a crucial aspect for the development of widespread photodetector technology. Some organic semiconductors are sensitive to moisture and oxygen, and the degradation might result in a significant impact on the performance of OPDs. In the past, we have shown that PMA-doping technique improves the photo-oxidative stability of polymer films. However, a systematic photo-oxidation stability measurement in a device level is worthy of being investigated.

7.2.2 Photoresponse Spectrum

Near-infrared (NIR) OPDs have drawn wide attention recently. However, small transport bandgap and amorphous phase in NIR materials remain challenges in the development of the high-performance NIR OPDs. In this work, we have shown that the ALD treatment enables electronic noise in OPDs and be applicable to various systems, including PDPP3T:PC₇₁BM devices. The preliminary results indicated that PDPP3T:PC₇₁BM OPDs yield responsivity of 0.1 A/W at 850 nm and higher reproducibility after ALD treatment. The treatment condition can be further optimized and, the photodetector performance can be investigated. In addition, the use of non-fullerene acceptors that enable photoresponse in the NIR region is promising to develop high-detectivity NIR OPDs with ALD treatment.

7.2.3 Stretchable Organic Photodiodes

Interest in developing flexible and stretchable optoelectronics is blooming. Stretchable OPVs applicable to non-planar solar roofing or robotic systems have been demonstrated recently (14, 41-47). To our best knowledge, few stretchable OPD has been reported in the literature. Stretchable devices provide a higher form factor and therefore outperform flexible devices in biomedical applications, such as electronic eyes or artificial skins.

7.2.4 *Self-Sustainable Sensors*

Ubiquitous intelligence and computing systems are driving innovations to enable the wide distribution of photodetectors, communications, and information. Power consumption becomes a crucial issue as integrating amounts of devices in a system. In this work, we developed high-performance OPDs operated at low power. We can further integrate OPDs into large-area arrays and realize an imaging sensing applications. Furthermore, integration of the sensing platform with a large-area OPVs as use of energy harvester can potentially achieve a self-sustainable sensing application.

REFERENCES

1. A. Pierre, A. Gaikwad, A. C. Arias, Charge-integrating organic heterojunction phototransistors for wide-dynamic-range image sensors. *Nature Photonics* **11**, 193 (2017).
2. Z. S. Ballard, A. Ozcan, in *Mobile Health: Sensors, Analytic Methods, and Applications*, J. M. Rehg, S. A. Murphy, S. Kumar, Eds. (Springer International Publishing, Cham, 2017), pp. 313-342.
3. X. Gan *et al.*, Chip-integrated ultrafast graphene photodetector with high responsivity. *Nature Photonics* **7**, 883 (2013).
4. D. Baierl *et al.*, A hybrid CMOS-imager with a solution-processable polymer as photoactive layer. *Nature Communications* **3**, 1175 (2012).
5. M. M. Research. <https://www.maximizemarketresearch.com/market-report/image-sensor-market/897/>
6. S. Ghanbarzadeh, S. Abbaszadeh, K. S. Karim, Low Dark Current Amorphous Silicon Metal-Semiconductor-Metal Photodetector for Digital Imaging Applications. *IEEE Electron Device Letters* **35**, 235-237 (2014).
7. C. Hoessbacher *et al.*, in *2016 Optical Fiber Communications Conference and Exhibition (OFC)*. (2016), pp. 1-3.
8. N. Youngblood, C. Chen, S. J. Koester, M. Li, Waveguide-integrated black phosphorus photodetector with high responsivity and low dark current. *Nature Photonics* **9**, 247 (2015).
9. Y. Lee *et al.*, High-Performance Perovskite–Graphene Hybrid Photodetector. *Advanced Materials* **27**, 41-46 (2015).
10. S. Wang *et al.*, Organic/inorganic hybrid sensors: A review. *Sensors and Actuators B: Chemical* **182**, 467-481 (2013).
11. T. Sekitani, U. Zschieschang, H. Klauk, T. Someya, Flexible organic transistors and circuits with extreme bending stability. *Nat Mater* **9**, 1015-1022 (2010).
12. T. Hassinen, K. Eiroma, T. Mäkelä, V. Ermolov, Printed pressure sensor matrix with organic field-effect transistors. *Sensors and Actuators A: Physical* **236**, 343-348 (2015).
13. H. Xu *et al.*, Flexible Organic/Inorganic Hybrid Near-Infrared Photoplethysmogram Sensor for Cardiovascular Monitoring. *Advanced Materials* **29**, 1700975-n/a (2017).

14. S. R. Forrest, The path to ubiquitous and low-cost organic electronic appliances on plastic. *Nature* **428**, 911-918 (2004).
15. C. J. Brabec, Organic photovoltaics: technology and market. *Solar Energy Materials and Solar Cells* **83**, 273-292 (2004).
16. K.-J. Baeg, M. Binda, D. Natali, M. Caironi, Y.-Y. Noh, Organic Light Detectors: Photodiodes and Phototransistors. *Advanced Materials* **25**, 4267-4295 (2013).
17. H. Xu *et al.*, A high-sensitivity near-infrared phototransistor based on an organic bulk heterojunction. *Nanoscale* **5**, 11850-11855 (2013).
18. F. Loffredo *et al.*, Photoresponse of pentacene-based transistors. *physica status solidi (a)* **211**, 460-466 (2014).
19. S. Singh, Y. N. Mohapatra, Persistent photocurrent (PPC) in solution-processed organic thin film transistors: Mechanisms of gate voltage control. *Journal of Applied Physics* **120**, 045501 (2016).
20. X. Liu, E. K. Lee, D. Y. Kim, H. Yu, J. H. Oh, Flexible Organic Phototransistor Array with Enhanced Responsivity via Metal-Ligand Charge Transfer. *ACS Applied Materials & Interfaces* **8**, 7291-7299 (2016).
21. H. J. Nam, J. Cha, S. H. Lee, W. J. Yoo, D.-Y. Jung, A new mussel-inspired polydopamine phototransistor with high photosensitivity: signal amplification and light-controlled switching properties. *Chemical Communications* **50**, 1458-1461 (2014).
22. M. Becquerel, Mémoire sur les effets électriques produits sous l'influence des rayons solaires. *Comptes rendus hebdomadaires des séances de l'Académie des sciences* **9**, 561-567 (1839).
23. D. M. Chapin, C. S. Fuller, G. L. Pearson, *A New Silicon p-n Junction Photocell for Converting Solar Radiation into Electrical Power*. (1954), vol. 25, pp. 676-677.
24. N. Sariciftci *et al.*, Semiconducting polymer-buckminsterfullerene heterojunctions: Diodes, photodiodes, and photovoltaic cells. *Applied physics letters* **62**, 585-587 (1993).
25. G. Yu, J. Gao, J. C. Hummelen, F. Wudl, A. J. Heeger, Polymer Photovoltaic Cells: Enhanced Efficiencies via a Network of Internal Donor-Acceptor Heterojunctions. *Science* **270**, 1789-1791 (1995).
26. Charge separation and photovoltaic conversion in polymer composites with internal donor/acceptor heterojunctions. *Journal of Applied Physics* **78**, 4510-4515 (1995).

27. Semiconducting polymer diodes: Large size, low cost photodetectors with excellent visible-ultraviolet sensitivity. *Applied Physics Letters* **64**, 3422-3424 (1994).
28. F. Guo, Z. Xiao, J. Huang, Fullerene Photodetectors with a Linear Dynamic Range of 90 dB Enabled by a Cross-Linkable Buffer Layer. *Advanced Optical Materials* **1**, 289-294 (2013).
29. P. Peumans, V. Bulovic, S. R. Forrest, Efficient, high-bandwidth organic multilayer photodetectors. *Applied Physics Letters* **76**, 3855-3857 (2000).
30. K. J. Baeg, M. Binda, D. Natali, M. Caironi, Y. Y. Noh, Organic light detectors: photodiodes and phototransistors. *Advanced materials* **25**, 4267-4295 (2013).
31. X. Gong *et al.*, High-Detectivity Polymer Photodetectors with Spectral Response from 300 nm to 1450 nm. *Science* **325**, 1665-1667 (2009).
32. A. Armin *et al.*, Thick junction broadband organic photodiodes. *Laser & Photonics Reviews* **8**, 924-932 (2014).
33. S. Xiong *et al.*, Universal Strategy To Reduce Noise Current for Sensitive Organic Photodetectors. *ACS Applied Materials & Interfaces* **9**, 9176-9183 (2017).
34. P. E. Keivanidis, P. K. H. Ho, R. H. Friend, N. C. Greenham, The Dependence of Device Dark Current on the Active-Layer Morphology of Solution-Processed Organic Photodetectors. *Advanced Functional Materials* **20**, 3895-3903 (2010).
35. Y. Mendelson, C. Pujary, in *Proceedings of the 25th Annual International Conference of the IEEE Engineering in Medicine and Biology Society (IEEE Cat. No.03CH37439)*. (2003), vol. 4, pp. 3016-3019 Vol.3014.
36. T. Guo, Z. Cao, Z. Zhang, D. Li, M. Yu, Reflective oxygen saturation monitoring at hypothenar and its validation by human hypoxia experiment. *BioMedical Engineering OnLine* **14**, 76 (2015).
37. L. Wang, B. P. Lo, G. Z. Yang, Multichannel Reflective PPG Earpiece Sensor With Passive Motion Cancellation. *IEEE Transactions on Biomedical Circuits and Systems* **1**, 235-241 (2007).
38. A. K. Bansal, S. Hou, O. Kulyk, E. M. Bowman, I. D. W. Samuel, Wearable Organic Optoelectronic Sensors for Medicine. *Advanced Materials* **27**, 7638-7644 (2015).
39. H. T. Yi, M. M. Payne, J. E. Anthony, V. Podzorov, Ultra-flexible solution-processed organic field-effect transistors. *Nature Communications* **3**, 1259 (2012).
40. T. Yokota *et al.*, Ultraflexible organic photonic skin. *Science Advances* **2**, (2016).

41. S. Bauer *et al.*, 25th Anniversary Article: A Soft Future: From Robots and Sensor Skin to Energy Harvesters. *Advanced Materials* **26**, 149-162 (2014).
42. T. Someya, Z. Bao, G. G. Malliaras, The rise of plastic bioelectronics. *Nature* **540**, 379 (2016).
43. E. O. Aminy, A. Ana Claudia, Flexible photovoltaic power systems: integration opportunities, challenges and advances. *Flexible and Printed Electronics* **2**, 013001 (2017).
44. Y. S. Rim, S. H. Bae, H. Chen, N. D. Marco, Y. Yang, Recent Progress in Materials and Devices toward Printable and Flexible Sensors. *Advanced Materials* **28**, 4415-4440 (2016).
45. A. E. Ostfeld, A. M. Gaikwad, Y. Khan, A. C. Arias, High-performance flexible energy storage and harvesting system for wearable electronics. *Scientific Reports* **6**, 26122 (2016).
46. Y. Khan, A. E. Ostfeld, C. M. Lochner, A. Pierre, A. C. Arias, Monitoring of Vital Signs with Flexible and Wearable Medical Devices. *Advanced Materials* **28**, 4373-4395 (2016).
47. Y. Qian *et al.*, Stretchable Organic Semiconductor Devices. *Advanced Materials* **28**, 9243-9265 (2016).
48. P. Adrien, A. Ana Claudia, Solution-processed image sensors on flexible substrates. *Flexible and Printed Electronics* **1**, 043001 (2016).
49. C. M. Lochner, Y. Khan, A. Pierre, A. C. Arias, All-organic optoelectronic sensor for pulse oximetry. *Nature Communications* **5**, 5745 (2014).
50. M. S. Arnold *et al.*, Broad Spectral Response Using Carbon Nanotube/Organic Semiconductor/C60 Photodetectors. *Nano Letters* **9**, 3354-3358 (2009).
51. Y. Xie *et al.*, Broad-Spectral-Response Nanocarbon Bulk-Heterojunction Excitonic Photodetectors. *Advanced Materials* **25**, 3433-3437 (2013).
52. A. Pierre, I. Deckman, P. B. Lechêne, A. C. Arias, High Detectivity All-Printed Organic Photodiodes. *Advanced Materials* **27**, 6411-6417 (2015).
53. G. Azzellino *et al.*, Fully Inkjet-Printed Organic Photodetectors with High Quantum Yield. *Advanced Materials* **25**, 6829-6833 (2013).
54. D.-S. Leem *et al.*, Low dark current small molecule organic photodetectors with selective response to green light. *Appl. Phys. Lett.* **103**, 043305 (2013).
55. E. Saracco *et al.*, Work Function Tuning for High-Performance Solution-Processed Organic Photodetectors with Inverted Structure. *Adv. Mater.* **25**, 6534-6538 (2013).

56. P. E. Keivanidis, P. K. Ho, R. H. Friend, N. C. Greenham, The Dependence of Device Dark Current on the Active-Layer Morphology of Solution-Processed Organic Photodetectors. *Adv. Funct. Mater.* **20**, 3895-3903 (2010).
57. I. K. Kim *et al.*, High-Performance, Solution-Processed Non-polymeric Organic Photodiodes. *Adv. Opt. Mat.* **3**, 50-56 (2015).
58. M. Kielar, O. Dhez, G. Pecastaings, A. Curutchet, L. Hirsch, Long-Term Stable Organic Photodetectors with Ultra Low Dark Currents for High Detectivity Applications. **6**, 39201 (2016).
59. A. Armin, R. D. Jansen-van Vuuren, N. Kopidakis, P. L. Burn, P. Meredith, Narrowband light detection via internal quantum efficiency manipulation of organic photodiodes. *Nat Commun* **6**, (2015).
60. M. Kielar, O. Dhez, G. Pecastaings, A. Curutchet, L. Hirsch, Long-Term Stable Organic Photodetectors with Ultra Low Dark Currents for High Detectivity Applications. *Scientific Reports* **6**, 39201 (2016).
61. R. D. Jansen-van Vuuren, A. Armin, A. K. Pandey, P. L. Burn, P. Meredith, Organic Photodiodes: The Future of Full Color Detection and Image Sensing. *Advanced Materials* **28**, 4766-4802 (2016).
62. Z. Shang *et al.*, Trade-Off between Trap Filling, Trap Creation, and Charge Recombination Results in Performance Increase at Ultralow Doping Levels in Bulk Heterojunction Solar Cells. *Advanced Energy Materials* **6**, 1601149 (2016).
63. X. Jia, C. Fuentes-Hernandez, C.-Y. Wang, Y. Park, B. Kippelen, Stable organic thin-film transistors. *Science Advances* **4**, eaao1705 (2018).
64. B. Kippelen, J.-L. Brédas, Organic photovoltaics. *Energy & Environmental Science* **2**, 251-261 (2009).
65. M. Knupfer, Exciton binding energies in organic semiconductors. *Applied Physics A* **77**, 623-626 (2003).
66. J.-L. Brédas, J. Cornil, A. J. Heeger, The exciton binding energy in luminescent conjugated polymers. *Advanced Materials* **8**, 447-452 (1996).
67. M. Stolterfoht *et al.*, Photocarrier drift distance in organic solar cells and photodetectors. *Sci. Rep.* **5**, 9949 (2015).
68. Y. Fang, A. Armin, P. Meredith, J. Huang, Accurate characterization of next-generation thin-film photodetectors. *Nature Photonics* **13**, 1-4 (2019).
69. A. van der Ziel, Noise in solid-state devices and lasers. *Proceedings of the IEEE* **58**, 1178-1206 (1970).

70. J. L. Wyatt, G. J. Coram, Thermodynamic validity of noise models for nonlinear resistive devices. *Proceedings of 1997 IEEE International Symposium on Circuits and Systems. Circuits and Systems in the Information Age ISCAS '97* **2**, 889-892 vol.882 (1997).
71. R. L. Stratonovich, *Nonlinear nonequilibrium thermodynamics I : linear and nonlinear fluctuation-dissipation theorems*. (Berlin New York : Springer-Verlag, 1992).
72. T. Martin, R. Landauer, Wave-packet approach to noise in multichannel mesoscopic systems. *Physical Review B* **45**, 1742-1755 (1992).
73. M. D. Groner, F. H. Fabreguette, J. W. Elam, S. M. George, Low-Temperature Al₂O₃ Atomic Layer Deposition. *Chemistry of Materials* **16**, 639-645 (2004).
74. Y. Zhou *et al.*, A Universal Method to Produce Low-Work Function Electrodes for Organic Electronics. *Science* **336**, 327-332 (2012).
75. Y. Zhou *et al.*, All-plastic solar cells with a high photovoltaic dynamic range. *Journal of Materials Chemistry A* **2**, 3492-3497 (2014).
76. M. B. Prince, Silicon Solar Energy Converters. *J. Appl. Phys.* **26**, 534-540 (1955).
77. W. J. Potscavage, S. Yoo, B. Kippelen, Origin of the open-circuit voltage in multilayer heterojunction organic solar cells. *Appl. Phys. Lett.* **93**, 3 (2008).
78. B. P. Rand, D. P. Burk, S. R. Forrest, Offset energies at organic semiconductor heterojunctions and their influence on the open-circuit voltage of thin-film solar cells. *Phys. Rev. B* **75**, 115327 (2007).
79. W. J. Potscavage Jr, S. Yoo, B. Kippelen, Origin of the open-circuit voltage in multilayer heterojunction organic solar cells. *Applied physics letters* **93**, 413 (2008).
80. G. Eppeldauer, J. E. Hardis, Fourteen-decade photocurrent measurements with large-area siliconphotodiodes at room temperature. *Applied Optics* **30**, 3091-3099 (1991).
81. A. G. *et al.*, Fully Inkjet-Printed Organic Photodetectors with High Quantum Yield. *Advanced Materials* **25**, 6829-6833 (2013).
82. G. H. Gelinck *et al.*, X-Ray Detector-on-Plastic With High Sensitivity Using Low Cost, Solution-Processed Organic Photodiodes. *IEEE Transactions on Electron Devices* **63**, 197-204 (2016).
83. A. Falco, L. Cinà, G. Scarpa, P. Lugli, A. Abdellah, Fully-Sprayed and Flexible Organic Photodiodes with Transparent Carbon Nanotube Electrodes. *ACS Applied Materials & Interfaces* **6**, 10593-10601 (2014).

84. H. Jin *et al.*, Efficient, Large Area ITO-and-PEDOT-free Organic Solar Cell Sub-modules. *Advanced Materials* **24**, 2572-2577 (2012).
85. M. Kröger *et al.*, Role of the deep-lying electronic states of MoO₃ in the enhancement of hole-injection in organic thin films. *Applied Physics Letters* **95**, 123301 (2009).
86. W.-F. Xu, C.-C. Chin, D.-W. Hung, P.-K. Wei, Transparent electrode for organic solar cells using multilayer structures with nanoporous silver film. *Solar Energy Materials and Solar Cells* **118**, 81-89 (2013).
87. Z. Wang *et al.*, Improvement of transparent silver thin film anodes for organic solar cells with a decreased percolation threshold of silver. *Solar Energy Materials and Solar Cells* **127**, 193-200 (2014).
88. W. Cao *et al.*, Flexible organic solar cells using an oxide/metal/oxide trilayer as transparent electrode. *Organic Electronics* **13**, 2221-2228 (2012).
89. L. Mao *et al.*, Flexible large-area organic tandem solar cells with high defect tolerance and device yield. *Journal of Materials Chemistry A* **5**, 3186-3192 (2017).
90. A. John, Photoplethysmography and its application in clinical physiological measurement. *Physiological Measurement* **28**, R1 (2007).
91. T. Tamura, Y. Maeda, M. Sekine, M. Yoshida, Wearable Photoplethysmographic Sensors—Past and Present. *Electronics* **3**, 282 (2014).
92. H. Xu *et al.*, Flexible Organic/Inorganic Hybrid Near-Infrared Photoplethysmogram Sensor for Cardiovascular Monitoring. *Advanced Materials* **29**, 1700975 (2017).
93. T.-H. Kim *et al.*, Fully Stretchable Optoelectronic Sensors Based on Colloidal Quantum Dots for Sensing Photoplethysmographic Signals. *ACS Nano* **11**, 5992-6003 (2017).
94. H. Zhang *et al.*, Transparent Organic Photodetector using a Near-Infrared Absorbing Cyanine Dye. *Scientific Reports* **5**, 9439 (2015).
95. V. A. Kolesov *et al.*, Solution-based electrical doping of semiconducting polymer films over a limited depth. *Nature Materials* **16**, 474 (2016).
96. F. A. Larrain *et al.*, Stable solvent for solution-based electrical doping of semiconducting polymer films and its application to organic solar cells. *Energy & Environmental Science* **11**, 2216-2224 (2018).